1-1-2012

Studying the glial cell response to biomaterials and surface topography for improving the neural electrode interface

Evon S. Ereifej
Wayne State University,

STUDYING THE GLIAL CELL RESPONSE TO BIOMATERIALS AND SURFACE TOPOGRAPHY FOR IMPROVING THE NEURAL ELECTRODE INTERFACE

by

EVON S. EREIFEJ

DISSERTATION

Submitted to the Graduate School

of Wayne State University,

Detroit, Michigan

in partial fulfillment of the requirements

for the degree of

DOCTOR OF PHILOSOPHY

2012

MAJOR: BIOMEDICAL ENGINEERING

Approved by:

Advisor	Date

DEDICATION

I dedicate my dissertation work to my parents, Sami and Suad Ereifej who have always encouraged me to work hard and reach my goals. They have dedicated their lives to give their children the privileges they did not have growing up. They taught us the importance of having an education. In the words of my father, "your book is your best friend...go read".

ACKNOWLEDGEMENTS

Above all I would like to thank my advisor, Dr. Pamela VandeVord for all of her support and guidance over the years. Without her I would not have had the opportunity to work on this research project. Dr. VandeVord has patiently mentored me and allowed me to discover everything I now know about research. She inspires me to follow my dreams and pursue all of my life's goals. A special thank you goes to my committee members, Dr. Howard Matthew, Dr. Golam Newaz, and Dr. Jinsheng Zhang. You have all given me much support, knowledge, time and advice along the way.

Furthermore, I would like to thank all the members of Dr. VanndeVord's lab group; you are all such a dynamic and kind group of people to work with. I'd like to recognize those lab members who were there from the beginning of this journey and taught me numerous lab skills, Roche deGuzman, Kristy Broadrick, Lai Yee Leung, Bin Wu and Li Mao, and those who joined later on and were there until the end, Rebecca Miller, Sujith Sajja, Therez Bu-Akal and Yanmei Yuan. A very special thank you to Alessandra del Cengio Leonardi and Nisrine Zakaria for all of the encouragement, wisdom and assistance you have given me over the years. I would also like to convey my sincere appreciation to Saida Khan, you are an exceptional mentor, you have taught me so much and thanks to the projects I worked on with you I have found my passion in research. My heartfelt gratitude goes to Dr. Timothy Hadden for his patience, kindness, and intelligence in helping me with my molecular experiments. Dr. Hadden, is a truly gifted professor, researcher and mentor who has guided me not only in the lab, but has taught me some lifelong lessons I will never forget.

I sincerely appreciate all the sources of funding that partially supported this research: Wayne State University President's Translational Enhancement Award and the Kales Scholarship for Biomedical Engineering students.

I am indebted to support I have received from numerous lab groups at Wayne State University. Many thanks to Dr. Auner and Dr. Cheng for assistance with material fabrication used in these studies. Much appreciation goes to Dr. Mao and her student Li Li for aid with AFM and contact angle measurements. Thank you to Dr. Ren for support in use of lab equipment. I would like to express my gratitude to Dr. Bulent Ozkan for this help, advice, and guidance on the statistical analysis of my data.

Last but not least, I am so thankful for all of the love and encouragement I have received from my family and friends over the years. The pride emanating from you all has motivated me to do my best and reach my greatest potential. I would like to express my deepest appreciation to my parents, Sami and Suad Ereifej, without whom this could not have been possible; you have been there for me from the beginning and carried me until the end. Thank you!

TABLE OF CONTENTS

LIST OF FIGURES

LIST OF TABLES

CHAPTER 1

1.1 Introduction to the Problem

The concept of having neural electrodes located within the brain to stimulate and record signals in order to treat neurological disorders is very exciting, however, to this day, the ability to design a stable, long-term device has failed (Polikov et al., 2006). For approximately three decades, researchers have been attempting to develop neuroprosthetic devices that can re-establish lost functions after nervous system injury (Szarowski et al., 2003). Two of the most successful neural advances made thus far are the deep brain stimulators used to treat neurodegenerating diseases such as Parkinson's disease and the use of cochlear implants to improve hearing in the deaf (Szarowski et al., 2003). It is the formation of electrical connections with neural dendrites and axons, that controls the functionality of a microelectrode neuroprosthetic device (Turner et al., 1999). At the minimum, there needs to be electrical connections to the surrounding tissue to record field and single-unit potentials (Turner et al., 1999).

The damage to the brain tissue caused by neural electrode insertion reduces the lifespan of the electrode (Frampton et al., 2010; Szarowski et al., 2003; Yuen et al., 1981). Implantation of such devices has been shown to lead to changes in gene expression, increased cell proliferation, compromised blood-brain barrier integrity, infiltration of circulating macrophages, intermittent ischemia, and generation of reactive oxygen species and inflammatory cytokines (Frampton et al., 2010; Griffith and Humphrey, 2006; McCreery and Agnew, 1983; Szarowski et al., 2003; Turner et al., 1999). Moreover, the sustained presence of the neural electrode results in increased glial cell volume and migration to and proliferation of activated glial cells at the

device-tissue interface (Frampton et al., 2010; Polikov et al., 2006; Szarowski et al., 2003; Turner et al., 1999). This response culminates in the formation of a fibrous and cellular sheath, covered by activated glial cells, encapsulating the neural electrode. Consequently preventing the recording and stimulation of neurons, which results in the inconsistent and unreliable device performance (Frampton et al., 2010; Polikov et al., 2005; Yuen et al., 1981) .

Some approaches towards reducing the tissue encapsulating sheath created by gliosis include targeting the problem at the site of insertion. It has been thought, that if the initial insertion tissue damage is minimized then the encapsulating sheath may accordingly be reduced (Szarowski et al., 2003; Yuen et al., 1981). It has been shown that device size and insertion speed play important roles in reducing the amount of insertion-related damage (Szarowski et al., 2003; Yuen et al., 1981). However, little is known on the role of other physical factors including device geometry and texture on reducing this tissue damage. Literature has shown that surface topography modifications can alter cell alignment, adhesion, proliferation, migration, and gene expression (Agnew et al., 1983; Cogan et al., 2005; Cogan et al., 2006; Merrill et al., 2005). Thus, the goal of this proposed work is to study surface topography effects on minimizing astrogliosis.

1.2 Hypothesis and Specific Aims

Neural electrodes show promise for the treatment of neurodegenerative disease, however, failure of the electrode has been inevitable following chronic implantation of the current devices. Glial scar formation around the electrode consequently forms a barrier preventing neuronal processes from reaching the electrode. Current research to alleviate the inflammatory and chronic immune response on electrodes focuses on altering the electrode size, materials, protein and drug coatings, and surface topographies. Research has shown that alterations in surface topography, such as nanopatterning, have significant effects to cellular and molecular behavior of cells. Nanopatterning has been reported to alter cellular adhesion, migration, proliferation, viability, morphology, alignment, differentiation, and gene expression. The majority of reports focus on neuronal response to materials, however, the glial response may likely predict this neuronal behavior. There is a gap in the knowledge base of how glial cells respond to nanopatterned surfaces. This information could lead to improved electrode designs which reduce the inflammatory effect and prevent glial scar formation.

Specific Aims:

1. Characterization of astrocyte reactivity and gene expression on biomaterials for neural electrode fabrication.

- Investigate the reactivity of C6 glioma cell line on four biomaterials used in neural electrode fabrication
- Materials to be tested include platinum, silicon, PMMA, and SU8. Polystyrene will serve as the control material.
- Astrocyte reactivity will be determined in terms of proliferation, gene expression of reactivity and proliferation factors, and cellular morphology.

- Identification of material to serve as the substrate to be nanopatterned (for aims 2-3).

Hypothesis: Each biomaterial will elicit a different response from the astrocytes. Astrocyte reactivity to these materials will vary according to proliferation, GFAP expression, viability and morphology. A compatible material will have cells with low levels of GFAP expression, steady proliferation rate, minimum 80% viability, and spread out cells with round nuclei.

2. Evaluation of protein and cellular response to nanopatterning.

- Determine if nanopatterning of a material will alter C6 astrocyte proliferation, viability, gene expression, morphology and alignment.
- Examine the effects nanopatterning has on ECM protein adhesive rate, quantity of adsorption, and alignment with the nanopattern.

Hypothesis: The nanopatterned surface will reduce the reactivity of the astrocytes as compared to the non-patterned surface. Moreover, the nanopattern surface will reduce the adsorption of the ECM proteins.

3. Comparative assessment of iridium oxide and platinum alloy wires using an *in vitro* glial scar assay

- Culture iridium oxide and platinum alloy wires with a mixed primary brain cells (consisting of astrocytes, microglia and neurons)
- Examine the glial scar thickness around the wires after seven days in vitro.
- Quantify through immunostaining the amount of cells around the wires.
- Determine the astrocyte reactivity through GFAP relative gene expression.

Hypothesis: The glial scar assay will be effective in assessing the biocompatibility of the materials. A glial scar will grow around both materials due to the foreign body inflammatory reaction.

4. Assessment of organotypic brain slice response on nanopatterned polydimethylsiloxane surface

- Culture organotypic brain slices with a nanopatterned and non-patterned substrate.
- Observe the gene expression of activity and cytokine factors.
- Determine through immunostaining and SEM the alignment of astrocytes on the nanopatterned surface.

Hypothesis: The nanopatterning will inhibit the inflammatory cascade and astrocytes will align along the nanopattern.

CHAPTER 2

2.1 Overview of the Central Nervous System Cells

The brain is a complex organ principally composed of neurons and glial cells. Astrocytes make up 30-65% of glial cells in the brain. Astrocytes are multifunctional cells whose roles range from homeostatic, information processing, and response to CNS injury (Buffo et al., 2010). Microglia compose 5-12% of total glial cells in the brain (Parekkadan et al., 2008). Microglia functions as the macrophage of the CNS, arriving first at the site of injury initiating the inflammatory cascade (Parekkadan et al., 2008). Neurons make up less than 25% of the cells in the brain; they are responsible for information processing and control of bodily functions (Polikov et al., 2005). These cells all work together to maintain a physiological homeostasis and functionality.

2.1.1 Astrocytes

Astrocytes cellular extensions give them a star-like appearance *in vitro* culture. Astrocyte functions include providing growth cues to neurons during Central Nervous System (CNS) development, mechanically support the mature neuronal circuits, buffer neurotransmitters and ions released during neuronal signaling, help control the chemical environment of the neurons, transfer of nutrients across the blood brain barrier, and modulate the firing activity of neurons (Fitch and Silver, 2008; Negi et al., 2010a; Polikov et al., 2005). Astrocytes are a major source of extracellular matrix proteins (ECM) and adhesion molecules such as laminin, fibronectin, cytotactin, J-1 family members janusin and tenascin, and nerve cell adhesion molecule (N-CAM) (2003; Miller and Peppas, 1985). They produce growth factors to regulate the morphology, proliferation, differentiation, and survival of neuronal subpopulations *in vivo*

and *in vitro*. Astrocytes contain ion channels for K^+, Na^+, Cl^-, HCO_3, and Ca^{2+} (2003; Dow and Wang, 1998; Nimmerjahn, 2009).

Astrocytes have processes that form a 15um thick barrier between the pia matter and the cerebral cortex neurons, called the glia limitans. This barrier separates and protects the CNS from non-CNS structures. Furthermore, astrocytes are responsible for blocking off damaged areas after injury from the healthy brain tissue (Fitch and Silver, 2008; Nimmerjahn, 2009). Astrocytes are characterized by their intermediate filaments made up of polymerized glial fibrillary acidic protein (GFAP). These filaments are 45-60 kDa, 8-10nm in diameter, many micrometers long, and are considered to be astrocyte specific cell markers (2003; Negi et al., 2010a; Polikov et al., 2005).

Astrocytes become activated in reaction to injury (Buffo et al., 2010). Activated astrocytes are hypertrophic, hyperplastic, have an upregulation of intermediate filaments GFAP and vimentin expression, and filament formation (Buffo et al., 2010; Gervasi et al., 2008). Studies have shown vimentin expression in mature reactive astrocytes, microglia and perivascular cells (Polikov et al., 2006; Szarowski et al., 2003). Activated astrocytes have a change in number and distribution of cellular organelles and glycogen deposits and an increase in matrix production and migration (Polikov et al., 2005; Seker et al., 2010). Reactive astrocytes are formed locally and spread to farther sites (2003; Seker et al., 2010; Turner et al., 1999). Studies have shown a variety of cytokines involved with either the initiation or modulation of reactive astrogliosis (Farina et al., 2007; John et al., 2003; Liberto et al., 2004; Rao et al., 2012). These cytokines include interleukin-1beta (IL-1β), tumor necrosis factor alpha (TNFα), and transforming growth factor beta 1 (TGFβ1), of which astrocytes express receptors and result in an astrocytic reactive response (Farina et al., 2007; John et al., 2003; Liberto et al., 2004; Rao et

al., 2012). Astrocyte-derived cytokines such as IL-1β and TNFα are considered to promote neurotoxicity whereas TGFβ1 acts as a neuroprotective (Farina et al., 2007; John et al., 2003; Liberto et al., 2004; Rao et al., 2012).

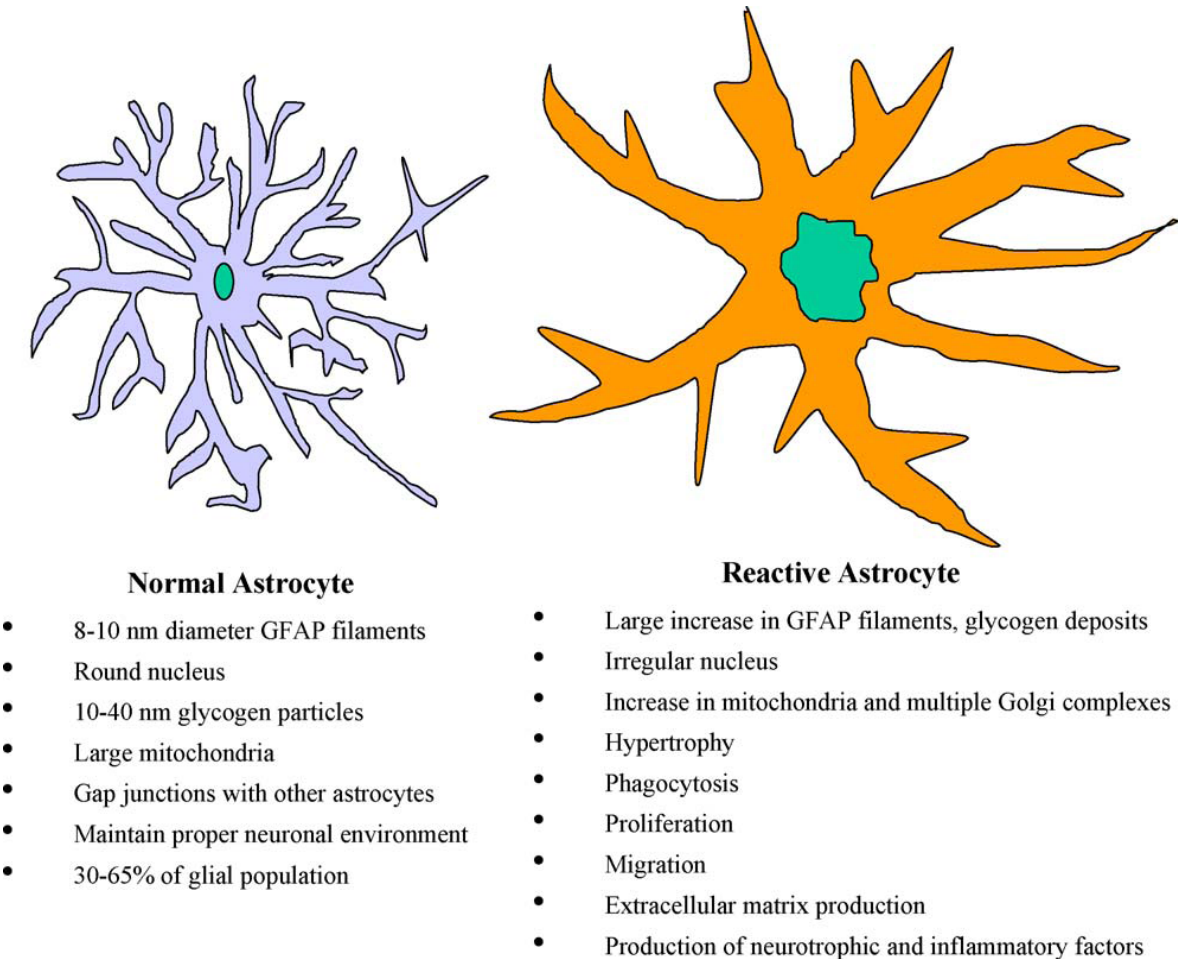

Figure 1. Schematic representation of a normal versus reactive astrocyte and their properties (Polikov et al., 2005).

2.1.2 Microglia

Microglia are termed the macrophages of the CNS and function as the "resident representatives of the immune system in the brain" (2003). Microglia enter the brain by blood-born hematopoetic cells through a prenatal infiltration. Microglia continuously migrate and

sample their local environment, unsurprisingly they are the first cell at the site of injury. They rapidly respond to protect neurons by releasing trophic and anti-inflammatory factors (Parekkadan et al., 2008). Microglia react to injury either by acting as phagoctyes or cytotoxic cells; they degrade extracellular matrix and cellular debris by secreting proteolytic enzymes and kill pathogenic organisms (Fitch and Silver, 2008; Polikov et al., 2005). Microglia are an immediate source for pro-inflammatory cytokines such as IL-1α, IL-1β, IL-6, and TNF-alpha, and the chemokine MCP-1 used in the recruitment of macrophages and microglia activation (Fujii et al., 2010; Parekkadan et al., 2008). They are known to release neurotrophic factors such as NGF, BDNF, and NT-3 which aid in neuronal growth and survival (Parekkadan et al., 2008). Microglia display an increased expression of leukocyte-associated molecules, such as CD68 and Mac-1/CD11b, recognized by the ED-1 and OX-42 antibody respectively (Polikov et al., 2005; Szarowski et al., 2003). Following injury, microglia are known to secrete various cytotoxic and neurotoxic factors that can lead to neuronal death. These include excitory amino acids, such as glutamate, reactive oxygen intermediates, such as hydrogen peroxide, and reactive nitrogen intermediates, such as nitric oxide. Studies have shown that the inability of a foreign body to be removed will result in the constant release of these neurotoxic factors (Polikov et al., 2005).

Activated microglia have an increased proliferation, more compact “amoeboid” morphology, phagocytose foreign material, and upregulate lytic enzyme production for foreign body degradation (Figure 2) (Polikov et al., 2005). Microglia play a dominant role in the acute inflammatory response to a foreign body (Fujii et al., 2010; Parekkadan et al., 2008; Polikov et al., 2005). Microglia cluster around the foreign body within the reactive glial scar until the implanted device is removed (Polikov et al., 2006).

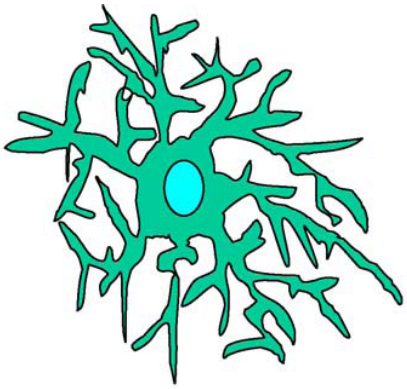

Resting or Ramified Microglia

- No Fc receptors, no macrophage specific receptors
- Large, dense chromatin masses in small flattened nucleus
- 5-10% of glial population
- Many long, thin processes

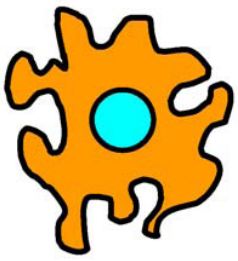

Activated or Amoeboid Microglia

- Upregulation of lytic enzymes
- Retraction of cytoplasmic processes to stouter, thicker pseudopodia
- Accumulation of phagocytosed material and lipid droplets
- Ameboid and motile abilities
- Release of inflammatory factors MHC I, II expression
- Active Proliferation

Figure 2. Schematic representation of a normal versus activated microglia and their properties (Polikov et al., 2005).

2.1.3 Neuron

Neurons they are responsible for information processing and control of bodily functions (Polikov et al., 2005). Neurons have three major regions: the cell body (perikaryon) containing the nucleus and major organelles, numerous dendrites and a single axon (Figure 3). Dendrites originate from the cell body, differ in shape and size and branch into the grey matter while axons can extend much further form the cell body and make up the white matter (2003).

Some axons are covered in an insulating myelin sheath which facilitates rapid impulse conduction which originates at the axon hillock as an action potential (2003). The CNS is made up of different types of neurons, including excitatory pyramidal neurons found in the cerebral

cortex and interneurons (2003). Pyramidal neurons are highly polarized, with a triangular shaped body, numerous dendrites that can spread over several millimeters and an axon that spans from the base of the cell body towards the subcortical white matter (2003). Neurotransmitters in pyramidal neurons are glutamate and aspartate. Interneurons can be excitatory or inhibitory. Spiny stellate cells are excitatory interneurons, they resemble pyramidal neurons in that they have large numbers of dendritic spines and use either glutamate or aspartate as their neurotransmitter (2003). There are a large variety of inhibitory interneurons found in the cerebral cortex, varying in size and shape, although they all use γ-aminobutyric acid (GABA) as their neurotransmitter (2003). Interneurons are found in the gray matter of the cerebral cortex, for their dendrites and axons do not spread very far (2003).

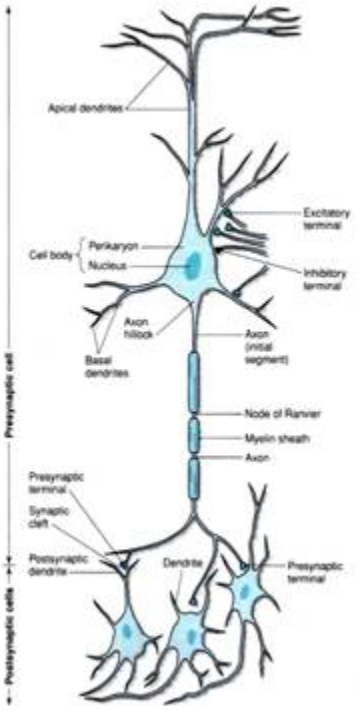

Figure 3. Illustration of a neuron (Cogan et al., 2010).

2.2 Injury/Glial Scar

The insertion of a micro-electrode device through cortical tissue severs capillaries, ECM, glial and neuronal cell processes. As the electrode is inserted deeper into the tissue, the damage to the ECM produces a high-pressure region surrounding the electrode (Polikov et al., 2005). The disruption of blood vessels initiates the release of erythrocytes, activates platelets, clotting factors, and the complement cascade for the recruitment of macrophages and initiates tissue rebuilding (Polikov et al., 2005). The inflammatory response within the brain tissue is characterized by the presence of reactive astrocytes and microglia. As early as one day post injury, activated microglia surround the implant (Kidambi et al., 2010; Szarowski et al., 2003). Studies have shown microglia and astrocytes remain at the surface of implanted biomaterials for up to nine months after implantation (Griffith and Humphrey, 2006; Morin et al., 2006; Morin et al., 2005; Morino et al., 2010; Polikov et al., 2005; Szarowski et al., 2003; Turner et al., 1999). Therefore, it is thought that these cells remain at the surface as long as the material remains in contact with brain tissue (Polikov et al., 2005). Moreover, it has been shown that cells forming the glial sheath appear to have migrated from nearby tissue (Turner et al., 1999).

The long-term effect of chronically implanted electrodes is the formation of a glial scar made up of reactive astrocytes and the matrix proteins they generate (Polikov et al., 2005; Rose et al., 1985). Astrocytes are reported to become activated from as far as 500 μm away from an electrode insertion site (Polikov et al., 2006; Polikov et al., 2005). Over time, the glial scar decreases in thickness, becoming denser and more organized (Polikov et al., 2006; Szarowski et al., 2003). Studies have shown glial scars from retrieved devices two weeks post implantation were 500-600 μm thick (Polikov et al., 2006; Szarowski et al., 2003; Turner et al., 1999). Several reasons have been hypothesized for glial scar formation such asunresolved acute

inflammation, toxicity of the device material, chronic movement between the device and brain tissue (Polikov et al., 2006; Szarowski et al., 2003; Turner et al., 1999). The glial scar functions to encapsulate the electrode, separating the damaged brain tissue and the foreign device from the undamaged, healthy tissue (Polikov et al., 2005). This encapsulation leads to an increasing distance between the electrode and its target neurite processes. Thus, increasing the impedance of the electrode and decreasing signal strength (Polikov et al., 2005). The strength and quality of the recorded electrical signal is determined by the location of the neuron in relation to the electrode recording sites. In order to maintain a recording and accurately observe action potentials, the maximum distance between neuron and electrode, commonly referred to as the "kill zone", can only be between 50-100 μm (McCreery and Agnew, 1983; Polikov et al., 2005; Turner et al., 1999; Wang et al., 2011). Studies have shown that the molecular composition of the glial scar and the production of inhibitory molecules by reactive astrocytes impair axon regeneration (2003; Rose et al., 1985). The astrocytes in the glial scar upregulate inhibitory molecules, such as, chondroitin sulfate proteoglycans (CSPGs), tenascin, Semaphorin 3, ephrin-B2, and slit proteins which play a role in the CNS axons inability to regenerate (Fitch and Silver, 2008). It has been shown that reactive astrocytes secrete proteoglycans that inhibit the growth of neuritis in injured spinal cord and brain models (Griffith and Humphrey, 2006).

2.2.1 Time Course of Glial Scar in vivo

Turner et al quantitatively studied astrocyte activation, morphology, and distribution changes to silicone probes *in vivo* (Polikov et al., 2005; Turner et al., 1999). They determined the time course for glial scar formation through the use of Confocal and scanning electron microscopy. Two weeks after a silicon electrode was implanted into a rat cerebral cortex, reactive astrocytes surrounded the implant site as far as 500-600um away. By four weeks, the

reactive astrocytes adjacent to the implant became denser and spread their processes around the insertion site. The web of astrocytes was observed to become denser by the six and 12 week time intervals (Polikov et al., 2005; Turner et al., 1999). Observations revealed a collapse of the insertion sites when the probe was removed after two and four weeks, but remained intact when the probe was removed at weeks six and 12 (Figure 4). (Turner et al., 1999). Furthermore, the formation of the glial scar was found to be much faster than the regrowth of neuronal axons, resulting in a high resistance barrier preventing the axons from extending. They concluded that studies earlier than two weeks are required to fully understand the formation of the glial scar.

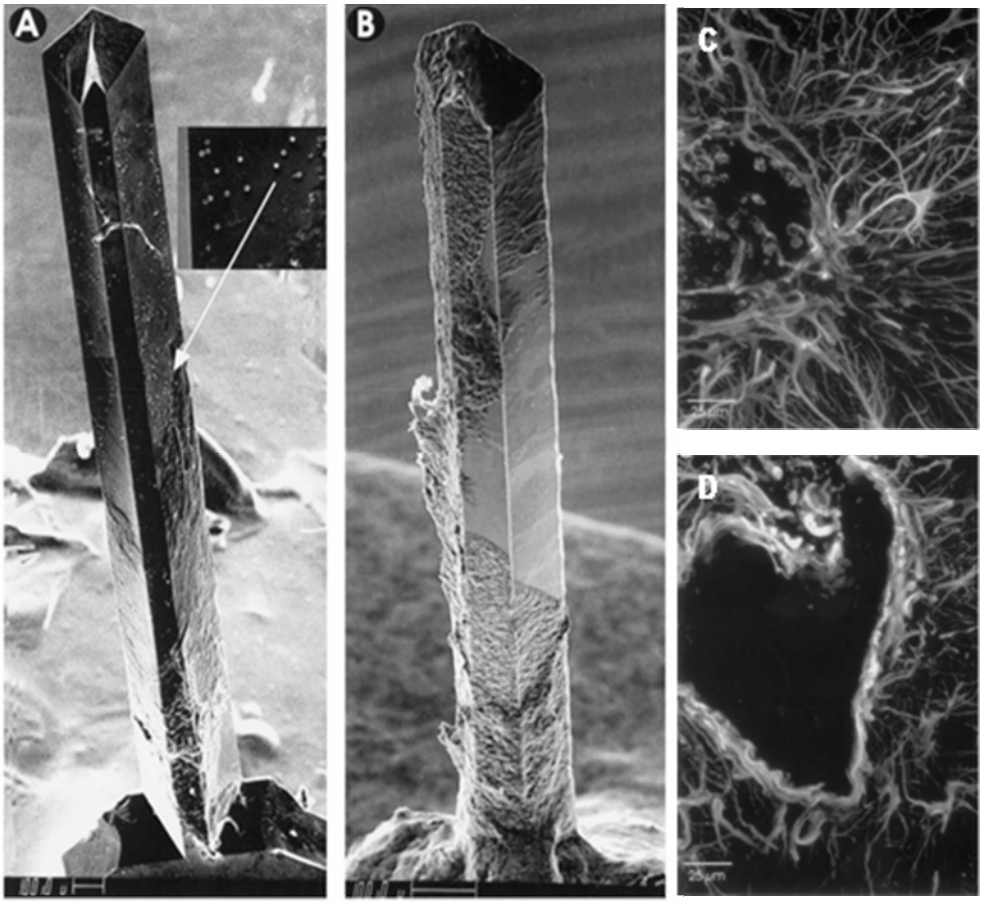

Figure 4. SEM images of (A) a 2 week probe and (B) a 6 week probe covered in layers of cells. The insert in (A) are magnified view of red blood cells attached to the probe. Confocal microscopy images of GFAP stained insertion sites at (C) 2 weeks and (D) 6 weeks (Turner et al., 1999).

Several years later, the same group studied time effects when varying the geometries of the probes and observing the tissue response starting at one day post implantation (Szarowski et al., 2003). GFAP staining revealed astrocytes were activated 100-200 μm away from the implant site one day post implantation. By the second week, GFAP-positive cells aligned around the device site. At week four, the encapsulation was 50-100 μm thick (Szarowski et al., 2003). Similarly to their previous study, astrocyte activation continued to spread up to 500 μm away from the implant site by the fourth week (Polikov et al., 2005; Szarowski et al., 2003; Turner et al., 1999). At six weeks the sheath thinned down to a compact 25-50 μm thick layer around the insertion site and remained constant up to week 12 (Szarowski et al., 2003). Szarowski et al also stained for vimentin expression. They found similar results to GFAP staining, however with much fewer cells making a 25-50 μm sheath thickness completed by week four. ED1 was utilized to stain for reactive microglia. Observations showed ED1-positive cells after one day around the insertion sites. By one week, the ED1-positive microglia covered an area three to four times as large as the initial insertion site. The microglia closest to the insertion site had short, thick processes, while the ones further away were elongated. By two weeks, the lumen of the site was filled with stained materials. The ED-1-positive microglia formed a 100-200um thick layer by the fourth week. Similar to the GFAP and vimentin positive staining, the sheath was more compact by the sixth week, which continued to thin out by week 12.

Szarowski et al demonstrated that the reactive cellular response, although expected during the first two weeks, are still found up to 12 weeks after device insertion (Figure 5). This suggests that the astrocytes and microglia are continuously being activated (Szarowski et al., 2003). It is believed that the cascade of events, beginning with the rupture of vessels when the

device is inserted, is related to the long term activation of the astrocytes and microglia (Szarowski et al., 2003). Furthermore, they concluded that the device size plays an important role in reducing the amount of insertion-related damage (Polikov et al., 2005; Szarowski et al., 2003).

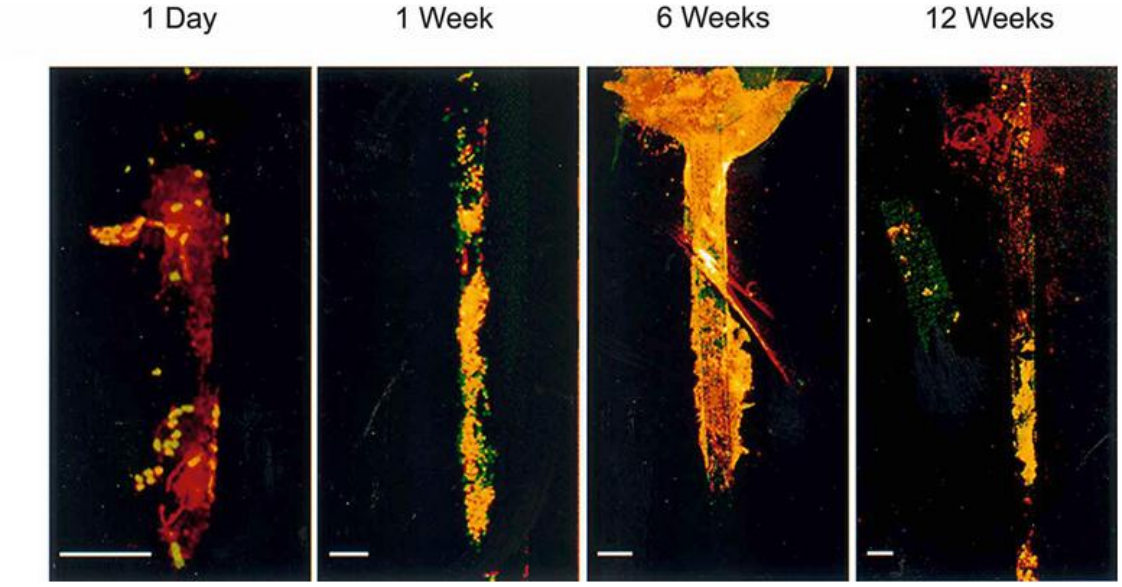

Figure 5. Devices removed from brains at 1 day and 1, 6, 12 weeks post insertion. GFAP (red) and nuclear stain (green), nuclei associated with GFAP-positive cells (yellow) (Szarowski et al., 2003).

2.2.2 In vitro glial scar models

After two decades of *in vivo* testing, the mechanism depicting the failure of chronic neural electrodes is still unclear. *In vitro* studies allow for the control at a molecular level in which the mechanisms of failure can be understood. However, there have been a limited number of studies creating an *in vitro* glial scar environment. Polikov et al proposed an *in vitro* model of glial scarring by culturing primary mixed brain cells, made up of neurons, astrocytes, and microglia. They injured the cell monolayer through a mechanical scrape followed by placement of a stainless steel wire near the scrape (Polikov et al., 2006). They found that astrocytes began

to extend their processes six hours post scrape injury and completely covered the site by day seven. Astrocytes around the scrape had fewer and thicker processes. Microglia entered the wound site one hour post scrape injury and were spread out over the entire wound area by six hours. Microglia covered the foreign body, in this case a stainless steel microwire, six hours after placement and remained there up to 14 days. Astrocytes began to form a glial scar over the microglial covered wire seven to ten days after placement (Figure 6) (Polikov et al., 2006). Polikov's results did not correlate with literature from *in vivo* studies. Neurons, *in vivo,* become depleted around the recording electrode, leading to a degradation of signal strength and failure of the implant. They concluded ten days in culture was not long enough to witness results typically found four to six weeks *in vivo* (Polikov et al., 2006).

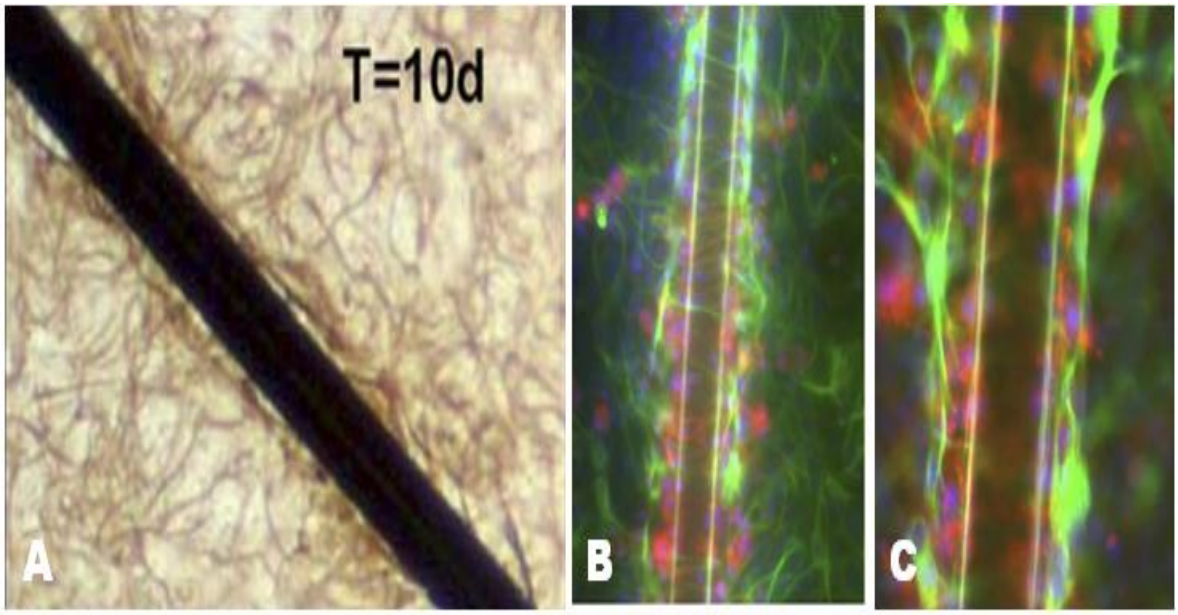

Figure 6. (A-C) Glial scarring on microwire after ten days in culture. (B-C) Fluorescent labeling of nuclei with DAPI (blue), astrocytes with GFAP (green), and microglia with OX-42 (red). (C) Higher magnification of image (B) (Polikov et al., 2006).

2.3 The Extracellular Matrix of the Central Nervous System

In 1971, the CNS ECM was first described by Tani and Ametani (Zimmermann and Dours-Zimmermann, 2008). They found that the CNS ECM is composed of numerous proteins and polysaccharides secreted from local cells and organized closely into a meshwork (Bruce Alberts, 2008). A specialized sheet-like ECM, known as the basement membrane, is primarily composed of collagen type IV, laminin, heparin sulfate proteogylcan and other glycoproteins (Yonezawa et al., 2010). The basement membrane provides mechanical support, separates tissues into different compartments, influences cells phenotypes, and acts as a selective molecular sieve (Yonezawa et al., 2010). The basement membrane in the CNS surrounds blood vessels and is beneath the pia mater and choroid plexus (Yonezawa et al., 2010).

The extracellular space in the mature CNS is condensed to 20% of the total volume (Rauch, 2007). Studies have shown that in a healthy adult brain, commonly found ECM proteins, such as fibronectin and collagen are scarce beneath the blood brain barrier and choroid plexus (Tate et al., 2007; Zimmermann and Dours-Zimmermann, 2008). In the healthy adult brain, fibronectin is limited to the meninges, choroids plexus and vascular basement membrane (Tate et al., 2007). However, fibronectin does play a crucial role in neural development; it promotes cell survival, migration, neurite outgrowth and synapse formation (Tate et al., 2007; Tate et al., 2009). Furthermore, when brain tissue damage occurs, fibronectin is found to be increased, most likely entering through the injured blood brain barrier (Tate et al., 2007). It has been shown that fibronectin has a reparative role, similar to that found in wound healing. It has been reported that the protein triggers anti-apoptotic cascades in neurons and is beneficial after brain ischemia (Tate et al., 2007; Tate et al., 2009). Tate et al showed that fibronectin in the injured brain serves to protect against cell death which correlates with neurological function

(Tate et al., 2007). The binding of fibronectin to microglial cells has been shown to elevate their adhesion, migration and proliferation (Mayeed et al., 2009; Tate et al., 2007; Thanawala et al., 2007). It has been shown that the secretion of fibronectin from microglia mediates the adhesion of microglia to synthetic materials used in neural electrode design (Mayeed et al., 2009; Thanawala et al., 2007). Moreover, activated microglia have an increased expression of $\alpha_4\beta_1$, $\alpha_5\beta_1$, and Mac-1 integrins that bind to fibronectin, which may promote the recruitment of microglia to the injury site (Mian et al., 2007; Tate et al., 2007). The binding of microglia to fibronectin will result in the increased production of anti-inflammatory cytokine transforming growth factor β (TGF-β) and nerve growth factor, which coherently will increase the production of neuroprotective and neurotrophic molecules (Hermanns et al., 2006). TGF-β is a primary regulatory factor in connective tissue and wound healing process; TGF-β1 is immediately released after injury, controlling the inflammatory and neuronal response, while TGF-β2 is expressed from astrocytes, endothelial cells, and macrophages more slowly, regulating the glial/collagenous scarring (Berdichevsky et al., 2010; Hermanns et al., 2006; Klapka and Muller, 2006). When TGF-β is released, there will be an increase in fibroblast proliferation, increased ECM production, and decreased ECM degradation (Berdichevsky et al., 2010; Hermanns et al., 2006). Furthermore, the release of TGF-β results in the transcription of connective tissue growth factor (CTGF) gene, which is a mitogen and chemoattractant stimulating collagen and fibronectin synthesis in fibroblasts (Figure 7) (Hermanns et al., 2006). Studies have revealed that following injuries to the CNS, a wound healing scar mainly composed of collagen type IV and fibronectin is formed in the lesion core surrounded by a glial scar around the parenchyma (Figure 8) (Hermanns et al., 2006; Klapka and Muller, 2006). It is thought that the rupture of the

dura allows for the entrance of non-neural meningeal and inflammatory cells to invade the CNS lesions (Klapka and Muller, 2006). Endothelial cells and astrocytes have been shown to express collagen type IV after injury (Hermanns et al., 2006).

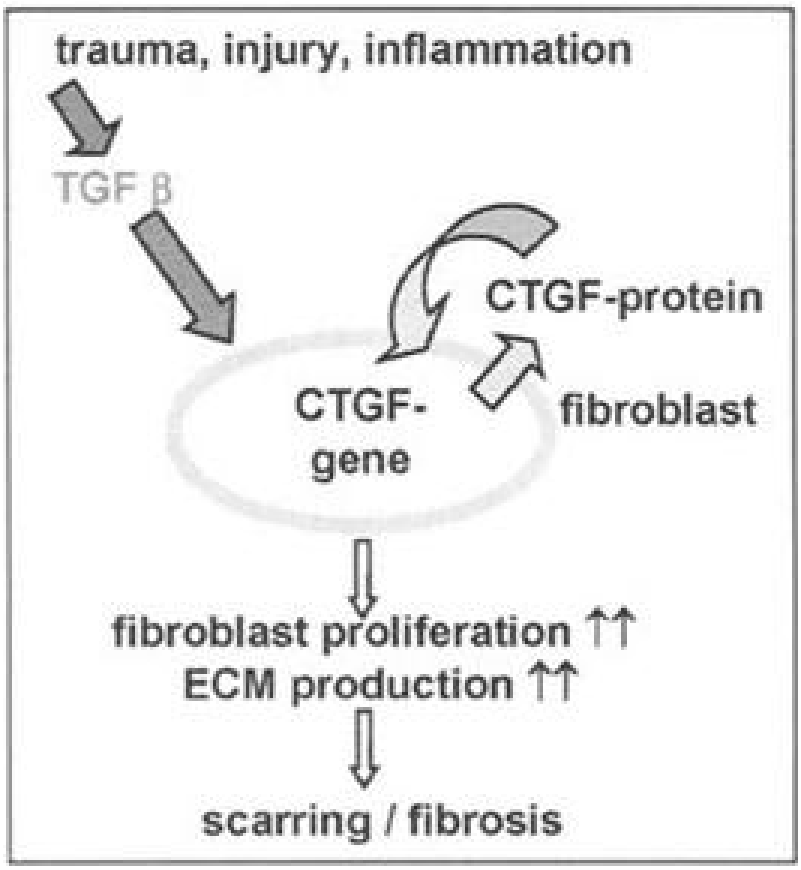

Figure 7. Schematic of TGFb release resulting in a scar tissue composed of ECM proteins (Hermanns et al., 2006).

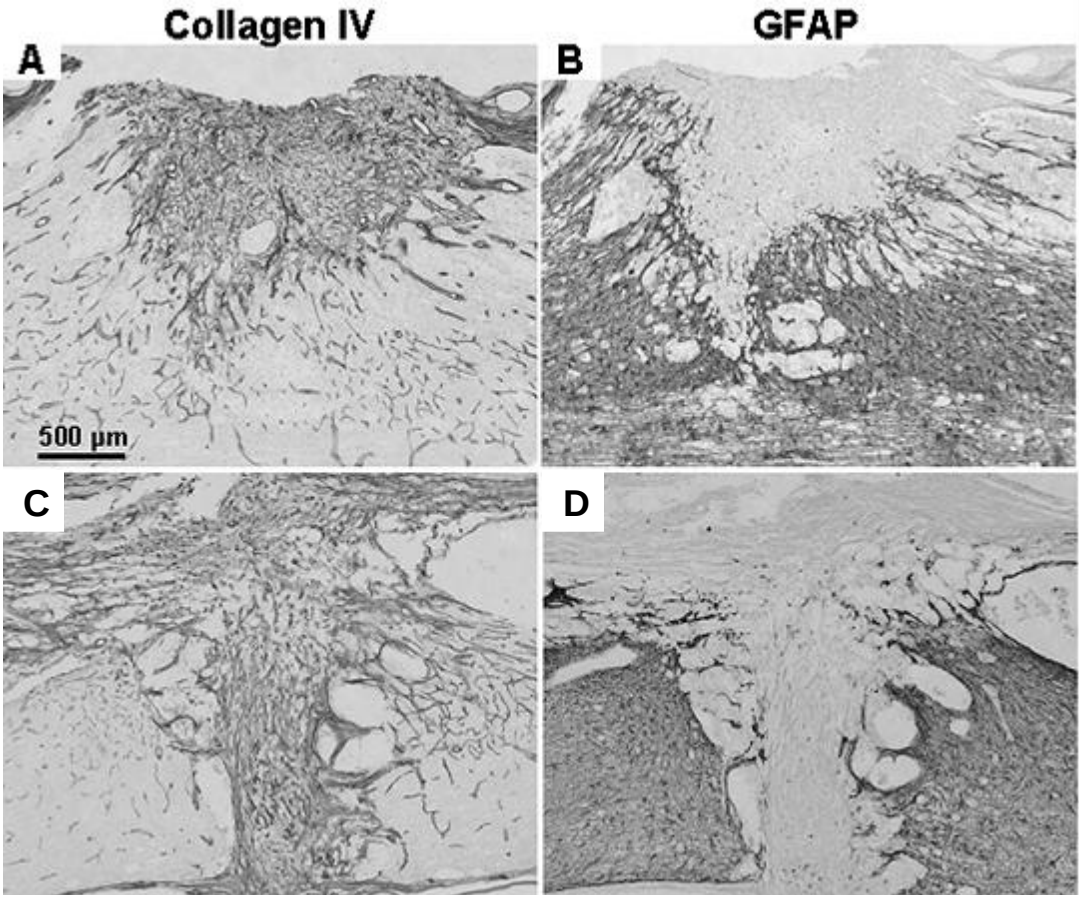

Figure 8. Immunostaining at seven day post injury in adult rat spinal cord of (A) and (C) collagen type IV stain and (B) and (D) GFAP (Klapka and Muller, 2006).

2.3.1Fibronectin

Fibronectin is a glycoprotein that is made up of two similar disulfide-linked subunits, each with a molecular mass of 250-280 kD and covalently linked by disulfide bonds near their C-termini (Humphries et al., 1989; Pankov and Yamada, 2002). There are three repeating subunits that make up each monomer; 12 type I repeats, 2 type II repeats, and 15-17 type III repeats (Pankov and Yamada, 2002). Type I repeats contain 40 amino-acids and 2 disulfide bonds, type II have 60 amino-acids and two intrachain disulfide bonds, and type III are 90 amino-acids long without any disulfide bonds (Figure 9) (Pankov and Yamada, 2002). Although there is only one fibronectin gene, it has evolved from numerous exon splicing, resulting in over 20 known variants of human fibronectin (Bruce Alberts, 2008; Pankov and Yamada, 2002). There are two types of fibronectin, depending on its solubility; plasma fibronectin, which is synthesized in the liver and found in the plasma and other soluble parts of the body, and insoluble cellular fibronectin, produced by numerous cell types and found in the extracellular matrix (Pankov and Yamada, 2002). Plasma fibronectin remains in a closed, nonactive form circulating in the blood, while fibronectin on the cell surface, can polymerize and form large disulfide-linked complexes (Humphries et al., 1989; Pankov and Yamada, 2002). Fibronectin has many binding domains, it serves as a ligand for many integrins, linking the ECM to intracellular cytoskeletons and contributes to organizing the ECM (Bruce Alberts, 2008; Pankov and Yamada, 2002). The best known integrin-recognition sequence is the Arginine-Glycine-Aspartic acid (RGD) sequence, located in the type III_{10} repeat which binds to the $\alpha_5\beta_1$ integrin (Bruce Alberts, 2008; Hocking et al., 1996; Pankov and Yamada, 2002). Fibronectin fibrillogenesis, or fibronectin matrix assembly, is tightly regulated process of creating and depositing fibronectin fibrils into the ECM. A critical step during the process of fibrillogenesis is the crosslinking of fibronectin dimers to

one another at the disulfide bonds; this process forms the fibrils and aggregates that are deposited in the ECM (Bruce Alberts, 2008; Pankov and Yamada, 2002). Some of these self -binding sites are exposed, while others are cryptic and are only accessible after conformational changes initiated by cell-driven mechanical stretching (Bruce Alberts, 2008; Pankov and Yamada, 2002).

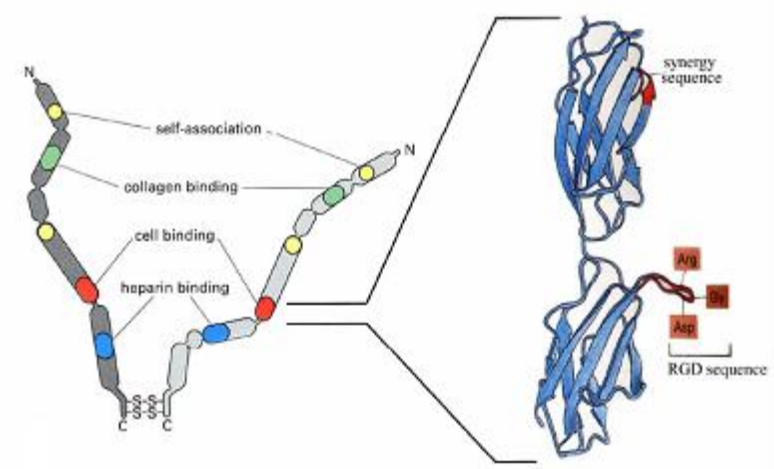

Figure 9. Structure of fibronectin dimer (left) two of the type III repeats with the RGD sequence (right) (Kane et al., 2011).

2.3.2 Collagen

Collagen, a fibrous protein secreted abundantly in connective tissue cells, is the most abundant protein in mammals, making up 25% of the total protein mass (Bruce Alberts, 2008). Collagen is made up of three α chains, each one 1000 amino acids long, that are wound together into a ropelike, stiff strand. Collagen is rich in proline and glycine; proline stabilize the helical conformation in each α chain while glycine is spaced at every third amino acid residue throughout the middle of the α chain (Figure 10) (Bruce Alberts, 2008). Collagen is arranged as a left-handed helix with three amino acids at every turn and glycine every third amino acid; triple-helices contain many triplet G-X-Y sequences, with X and Y being any amino acid, but usually X is proline and Y is hydroxyproline (Bruce Alberts, 2008). There are 42 different

human genes that code for collagen α chains, making 40 known types of collagen molecules; examples include type I collagen which is prominent in skin and bone and type IV collagen a major part of the basal lamina (Bruce Alberts, 2008). Collagen has a unique characteristic known as self assembly. Once collagen triple-stranded helical rod is secreted into the extracellular space, the collagen molecules self assemble into higher order polymers called fibrils (10-300 nm in diameter and hundreds of micrometers long) (Bruce Alberts, 2008). Collagen fibrils aggregate into large, cable-like bundles called collagen fibers, which are several micrometers in diameter. Collagen type IV triple helices are about 400 nm in length and self assemble to form the backbone of the basement membrane (Klapka and Muller, 2006). Collagen type IV is highly insoluble due to its disulfide and/or lysine aldehyde-derived cross-links (Klapka and Muller, 2006).

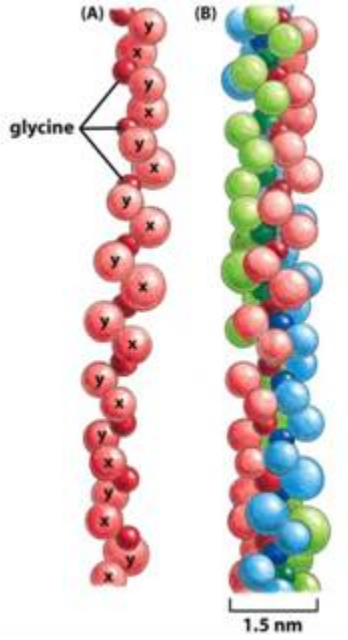

Figure 10. Structure of collagen (a) one α chain (b) collagen triple-stranded helix (Kane et al., 2011).

CHAPTER 3

3.1 Neural Electrodes

The use of electrosimulation of neural tissues goes back to 2500BC when Ancient Egyptians used the electrical shock from electrical catfish as a method of pain relief (Kotov et al., 2009). Since then, researchers have been developing neuroprosthetic devices that use microelectrode arrays to stimulate nerve cells. Current devices are based on electrical field-effect stimulation of functional neural elements to treat different diseases or disorders. These devices may provide a viable treatment for degenerative diseases of the CNS and spinal cord injury. The Food and Drug Administration approved the use of neural electrodes in adults in 1985; as of 2005, there were over 150,000 people with a cochlear implant (Kotov et al., 2009). Some of the other successful advancements made are the brain stimulations used to treat Parkinson's disease (Szarowski et al., 2003), epilepsy, tinnitus and retinal vision prosthesis (Cogan, 2008; Elfar et al., 2009; MA Howard, December 16, 1997). The use of microfabrication technology has helped fabricate devices ranging from 10 to 100s of micrometers, therefore allowing the target of precise regions in the brain (Szarowski et al., 2003).

There are two main subcategories of cortical neural prosthetics, stimulating and recording. Stimulating neural electrodes are used for Parkinson's disease treatment and restoring hearing (Zhong and Bellamkonda, 2008). Recording devices are also known as brain-computer interfaces and are used to help paraplegics control a wheelchair or prosthetic limb through thought by reading signals from an array of neurons and translating them into action (Zhong and Bellamkonda, 2008). Recent developments in microelectrode arrays include microwires, silicon micromachined microprobes (SMM) and polymer substrate probes; most commonly used are microwires and SMMs for their ease of process and fabrication (Zhong and Bellamkonda, 2008).

3.1.1 Microwires

Microwires were the first used chronic recording electrodes. They are fine wires with 25-50 μm diameter and 8 mm in length (Polikov et al., 2005). They are made from conducting metals, such as platinum, gold, tungsten, iridium, stainless steel and are insulated with non-cytotoxic Teflon or polyamide (Figure 11) (Zhong and Bellamkonda, 2008). The tip of the wire is not coated with an insulator therefore able to receive electronic signals from neurons (Polikov et al., 2005). These wires are soldered to a small connector in an array and glued to the skull to allow for greater prosthetic control (Zhong and Bellamkonda, 2008). Microwires are easier to fabricate, can enter deeper into the brain tissue and have a higher quality of recordings with lower impedance compared to silicon based electrodes (Polikov et al., 2005). However, they have been typically found to begin to lose signal within 5 weeks after implantation (Williams et al., 1999; Zhong and Bellamkonda, 2008). If the cortical surface moves after surgery, the electrode tips may either move to another cortical layer or move deep into the white matter, therefore failing to record from the desired neurons (Zhong and Bellamkonda, 2008).

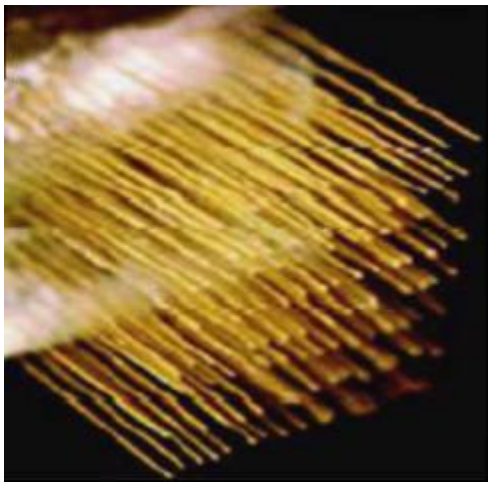

Figure 11. Microwires made of Teflon coated stainless steel (Khan et al., 2005; Polikov et al., 2005).

3.1.2 Silicon Micromachined Microprobes

Silicon micromachined microprobes (SMM) offer many advantages to microwire electrodes. The silicon photolithography process allows for smaller and higher electrode count arrays. This allows for more control over size, shape, texture, and spacing of the electrode, and for the ability to have multiple recording sites in a single electrode shank (Polikov et al., 2005; Zhong and Bellamkonda, 2008). There are two widely used SMMs, the Michigan probe and the Utah Electrode Array (UEA) (Figure 12). The Michigan Probe was developed at the University of Michigan Center for Neural Communication Technology. Michigan probes are composed of planar arrays of electrode shanks. These shanks are prepared from a single, thin, sheet of silicon. Shanks are typically, 15 μm thick, 100-500 μm wide, and range in length from 2 mm to 1 cm. Multiple recording sites are placed all along the top and bottom of the probe at user defined locations, rendering them to have better access to neurons (Polikov et al., 2005). Moreover, the electrodes will be able to be placed at multiple cortical depths for complete control of recording locations and depths, ideal for extracellular recordings (Zhong and Bellamkonda, 2008). Compared to the microwire electrodes, advantages of the Michigan probes include ability to fabricate batches at a time, reproducibility of size, shape and relative electrode locations, composition of high-density recording sites, and ability to incorporate circuits directly onto the probe (Zhong and Bellamkonda, 2008). Disadvantages include high electrode impedance, fragility due to planar design, therefore making them difficult to handle, post-process and further modify (Zhong and Bellamkonda, 2008). Currently, Michigan probes are being used in diagnostic and therapeutic neurological applications (Mian et al., 2005).

The UEA was developed at the University of Utah Center for Neural Interfaces and has been in use for over 20 years, but clinically only since 2004 (Mian et al., 2005). A single block of silicon is etched, doped, and heat treated to form the 3D array of needle-like electrodes with recording tips. The UEA can have either 25 or 100 shanks and varies in shape. Each shank is 1.5mm in length and ranges from 100 μm at its base to less than 1 μm at the tip (Polikov et al., 2005). Both systems require an insulating layer to protect the electrode from unwanted electrical signals. Teflon or S-isonel coatings have been successfully used with microwire electrodes. Epoxylite resins and plasma-deposited diamond-like carbon (DLC) have also had success. Polyamide is most commonly used to coat silicon based devices.

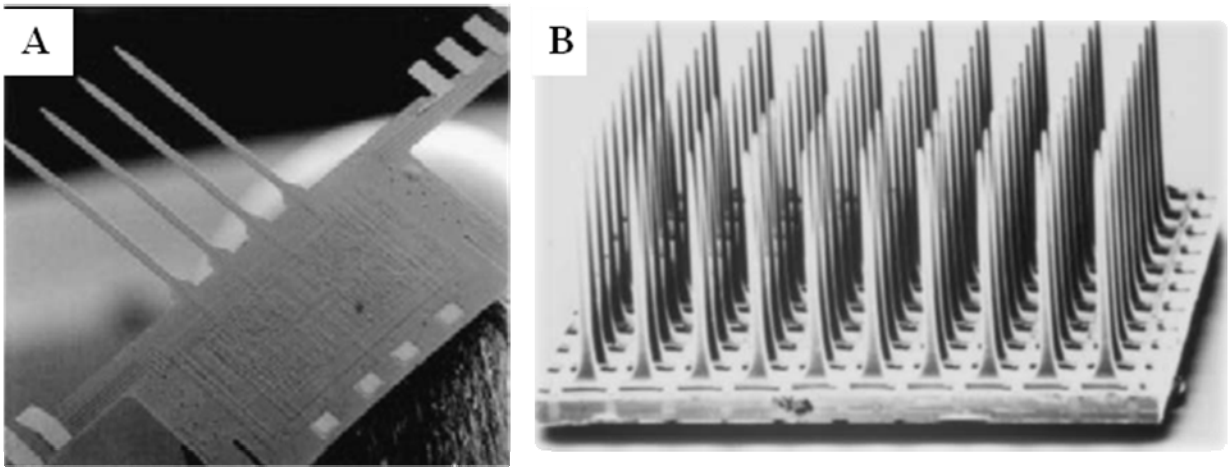

Figure 12. (A) Michigan electrode (B) Utah electrode (Harris et al., 1997; Kam et al., 2002; Polikov et al., 2005).

3.1.3 Clinical Use of Neural Prostheses

There has been a great deal of success in neural prostheses research over the last 35 year (Mian et al., 2005). Currently, over 200,000 devices are implanted into patients (Table 1) (Gobbels et al., 2010; Mian et al., 2005). The majority of these devices are either implanted into the spinal cord or a peripheral nerve. To date, there are limited microelectrodes that are used to

penetrate through the human cortex, otherwise known as, "brain-computer-interfaces" (BCI) (Mian et al., 2005). In fact, the first clinical use of the UEA was in 2004. At this point it has been commercialized to Cyberkinietics, Inc. (Foxborough, NJ, USA). This electrode was implanted in human subjects suffering from high spinal cord lesion (C3). These patients can now communicate through these neural prosthetic interfaces, at 20 letters per minute (Mian et al., 2005). In recent years, there have been a growing number of clinical trials using BCI to circumvent motor deficits (Grundke-Iqbal et al., 1981; H. Makamba, 2003; Samuel K. Sia, 2003; T. C. Merkel, 2000). However, their widespread clinical implantation is currently impeded by the difficulties in maintaining stable long-term recordings (Grundke-Iqbal et al., 1981).

Table 1. Summary of fully implanted neural prostheses with more than 1,000 implanted systems (Gobbels et al., 2010; Mian et al., 2005).

Application	Number of Implants	Manufacturers
Spinal cord stimulator to treat intractable pain and motor disorders	>130,000	Advanced Neuromodulation Systems, USA; Medtronic, USA
Auditory nerve stimulator to restore hearing (cochlear implant)	>55,000	Advanced Bionics, USA; AllHear, USA; Cochlear, Australia; MED-EL, Austria; MXM lab, France
Deep brain stimulator for tremor, Parkinson's disease and pain	>20,000	Medtronic, USA
Vagal nerve stimulator to treat intractable epilepsy	>17,000	Cyberonics, USA
Sacral nerve stimulator for urinary urge incontinence, urinary retention, pelvic pain and faecal incontinence	>10,000	Medtronic, USA
Sacral nerve stimulator for bladder emptying	>2500	Finetech Medical, UK
Phrenic Nerve stimulator for respiration	>1600	Avery Laboratories, USA; Atrotech, Finland; MedImplant, Austria

3.2 Neural Electrode Biomaterials

Neural electrodes are expected to function for the lifetime of the patient (Zhong and Bellamkonda, 2008). Customary biocompatible, corrosion-resistive materials are used for electrodes, including platinum, silicon and conducting polymers (Kotov et al., 2009). Platinum is one of the most commonly used materials in medical practice (Kotov et al., 2009). Platinum is used as stimulating/recording electrodes for it excellent conductivity (Polikov et al., 2005). Moreover, it is resistant to corrosion and has charge storage capacities in the range of 300-350mC cm^{-2}. However, there have been several studies that have found cytotoxic effects from SU-8 (De Boeck et al., 2003; Vernekar et al., 2009), silicon (Kotzar et al., 2002; Szarowski et al., 2003) and platinum (Griffith and Humphrey, 2006) cultured with neuronal cells or implanted *in vivo*. In a study done by Griffith et al with *Rhesus macaque*, glial scarring was found around platinum wires implanted into the motor cortex for periods up three years (Griffith and Humphrey, 2006).

SU-8 is a highly cross-linked, negative, near-ultraviolet (UV; 350-400nm) epoxy based photoresist that allows manufacturers to make high-aspect ratio thick microelectromechanical systems (MEMS) structures (Hopcroft et al., 2005; Vernekar et al., 2009). SU-8 is a commonly used material for bioMEMS and lab-on-a-chip devices. Advantageous of SU8 include its has dielectric properties, transparency to visible light, low Young's modulus (below ~5 Gpa), and low cost, (Hopcroft et al., 2005; Voskerician et al., 2003). Moreover, it is used because of its mechanical strength, chemical resistance, and simplicity in fabrication of a high aspect ratio structure. These properties suggest that SU-8 will have strong electrical and optical recording, which make it a compatible neuron-based device (Wu et al., 2006).

Conflicting data has been reported on the biocompatibility of SU-8. Kotzar et al investigated the biocompatibility of numerous bioMEMS materials, including silicon and SU-8. They found that these materials were not cytotoxic to mouse fibroblasts *in vitro*. Subsequently, they performed a study using rabbit muscle implantations which lead them to classify these materials as non-irritants. Furthermore, studies performed by Kisaalita's et al concluded that SU-8 microstructures are viable platforms for cell culturing systems for cell-based biosensing against drugs and promoting human neuroblastoma cells' resting membrane potential (Wang et al., 2009; Wu et al., 2006).

There have been several studies revealing contrary results with respect to the cytotoxicity with SU-8, thus rendering it a controversial material for biomedical purposes (Vernekar et al., 2009; Wu et al., 2006). It appears that the specific formula of SU-8 utilized in these experiments differ and may be the reason for the varying cell responses. When conducting aqueous physiochemical tests, Kotzar et al found that Si_3N_4 and SU-8 leached detectable nonvolatile residues (Kotzar et al., 2002; Ni et al., 2009). Vernekar et al examined primary neuronsfrom rats on various surface treatments of SU-8 for 21 days *in vitro* (Vernekar et al., 2009). Neurons had poor adhesion to the SU-8 surfaces and less than 10% of neurons survived when cultured adjacent to or on the SU-8 substrates (Vernekar et al., 2009). Moreover, they found toxins such as fluorine and antimony leaching from the SU-8 2000. SU8 2015 contains a faster drying, more polar solvent, cyclopentenone, compared to the original formula (SU-8-2000) which used butyrolactone (Vernekar et al., 2009). It was concluded that the current formulas of SU-8/SU-8 2000 are cytotoxic to primary neurons, thus rendering them incompatible (Vernekar et al., 2009).

Methods such as heat treatment, isopropanol sonication, parylene coating and oxygen plasma treatment all improved the cytocompatibility of SU-8. It was found that reusing the SU-8 2000 samples removed some of these toxic agents through passive diffusion. Therefore, indicating a possibility of detoxifying the SU-8 2000 through diffusion techniques.

Poly methyl methacrylate, (PMMA) and polysytrene are both considered biocompatible materials commonly used as substrates for mammalian cell culture (Ni et al., 2009). PMMA has been used for medical applications for a number of years for its excellent tissue compatibility(Frazer et al., 2005). PMMA is a polymer that has been often used in numerous medical devices and more recently been employed for the production of MEMS for medical applications (bioMEMS/bioNEMS) (Bhushan, 2008; Frazer et al., 2005; Kotzar et al., 2002). Characteristics of PMMA include its excellent tissue compatibility, ease of polymer manipulation, strength, availability, inexpensiveness, radiolucency, low thermal and electrical conductance and weight. Negative features of PMMA include its relative low surface energy and tremendous release of heat during polymerization, which may cause protein denaturation and tissue damage (Frazer et al., 2005). Several groups have shown good growth rates for dorsal root ganglion neurons cultured on PMMA (Cogan et al., 2006; Song and Uhrich, 2007). Moreover, these groups stated they used PMMA as their substrate because of its isotropic properties, the fact that it is a well-characterized polymer for Nano-Imprint Lithography (NIL) in their laboratory.

CHAPTER 4

4.1Nanopatterning

Current approaches towards inhibiting the initiation of glial scarring range from altering the geometry, roughness, size, shape and materials of the device (Grill et al., 2009; Kotov et al., 2009; Kotzar et al., 2002; Szarowski et al., 2003). An array of design strategies have been targeted toward minimizing failure of implanted microelectrodes by minimizing the chronic glial scar around the microelectrode under chronic conditions. These approaches have included developing novel implant materials, shape, size, and rigidity. The speed of implantation, use of bioactive coatings, and repositioning of the device post implantation have also been studied to improve biocompatibility (Stice and Muthuswamy, 2009). In order to properly design a successful neural electrode, the understanding of the cellular environment is mandatory.

In vivo conditions comprise of cells living in the ECM meshwork with a three-dimensional and high aspect ratio topographical textures (Millet et al., 2010; Wu et al., 2006). The 3D environment allows cells to have topographical cues which will allow them to differentiate and perform their specific functions. Moreover, the first interaction that a protein has with the biomaterial is what influences the cellular response. Properties such as the chemistry, surface charge, and topography of a material are major factors in protein adsorption, of which consequently effect the cell reaction as well (Kriparamanan et al., 2006). The objective of altering the surface of material by adding a nanoscale surface roughness lies in the understanding that the *in vivo* environment is not smooth. Atomic force microscopy (AFM) has been used to measure the topographic structure of numerous basement membranes (Kriparamanan et al., 2006). These studies have shown that a material that can mimic the nanotopography of the natural environment *in vivo* will consequently result in an improved

biocompatible response (Curtis et al., 2004; Ding et al., 2010; Kotov et al., 2009; Millet et al., 2010; Zervantonakis et al., 2011). Nanotopography has been shown to affect the cells' morphology, alignment, adhesion, proliferation, gene expression profiles and even prevent biofouling and contamination on the material's surface(Kriparamanan et al., 2006). Topography affects gene expression and protein production, such as cytokines, growth factors, signaling molecules, and cytoskeleton linked molecules (Kriparamanan et al., 2006). Therefore, just as the chemical composition of a material alters the cellular response, as does the size of the nanostructure on the substrate. Researchers in Scotland have done extensive work in surface topography and fibroblasts. They have found that fibroblasts will adhere to surfaces with a height range of 20-70nm, but will not attach well to larger or smaller surfaces of the same material (Curtis, 2005; Curtis et al., 2004; Das et al., 2008; Fok-Seang et al., 1998). In another study they found that fibroblast adhesion is enhanced at cliff edge features, but diminished at pits and pillars (Fok-Seang et al., 1998). They concluded that cellular adhesion is affected by surface features (Fok-Seang et al., 1998). This group also studied the cytoskeleton of fibroblasts on microgrooved surfaces and confirmed an earlier theory that, "cells react to topography primarily at lines of discontinuity in the substratum by actin nucleation" (Muir et al., 1998). They concluded that the aggregation of actin along groove/ridge boundaries is a primary driving event in determining fibroblast orientation on microgrooved substrata (Muir et al., 1998). Effects of microgrooves on fibroblast gene expression were observed in a later study (O'Keefe et al., 2001). The results showed many initial gene changes and also down-regulation of gene response with time (O'Keefe et al., 2001). This was thought to happen due to the deformation in the cell and nucleus morphology (O'Keefe et al., 2001).

Cell type also appears to play a role in reaction to the material topography (Kriparamanan et al., 2006). This cell-specific response can be used when customizing novel topography for specific devices. For example, it may be important for one cell type to adhere and spread on a surface while not for another cell type (Kriparamanan et al., 2006). It has been shown that fibroblasts show a decrease in cell adhesion on 50-100nm sized etching, whereas endothelial cells adhere and proliferate on 50-500nm sized etched nanostructures (Chung et al., 2010; Chung et al., 2009; Sudo et al., 2009). Dalby et al studied the effects of polymer demixed island topography with a 95-nm Z axis on endothelial and fibroblast cells (Bruder et al., 2007). They found that endothelial cells exposed to the topography had more of a curved morphology, similar to the vascular endothelium found *in vivo* (Bruder et al., 2007). Meanwhile, fibroblasts exposed to these same islands had more of a rounded morphology and poorly shaped cytoskeleton (Bruder et al., 2007). These results suggested that the cells had more of a phenotypically correct morphology when exposed to the nanoscale features (Bruder et al., 2007; Dalby et al., 2004; Das et al., 2008; Kriparamanan et al., 2006).

The mechanism involved with the cellular response to a nanopatterned surface is not well understood. It is thought that the effects of the surface topography directly influence the cell response, or indirectly effect the cell responses through the affects they have on the adsorption of proteins (Kriparamanan et al., 2006). Nanotopography has been shown to alter protein adsorption, as it has been shown that different proteins respond differently to the nanopatterned surfaces (Kriparamanan et al., 2006). The range for optimal protein adsorption on a nanopatterned surface is found to be very narrow (Kriparamanan et al., 2006). Studies have shown low randomly oriented protein adsorption on a 4 nm height, but high adsorption of defined orientation proteins on 1-2 nm high nanostructures (Kriparamanan et al., 2006). Cell

alignment onto the surface begins soon after the cells adhere to the surface and it is very dependent on the cell type. The substrate topography affects the alignment of the actin filaments and the focal adhesion structures, therefore altering the cell morphology, adhesion, and function (Kriparamanan et al., 2006). Cell alignment generally means the polarization and elongation of the cells in the direction of the nanogrooves. For example, when fibroblasts are seeded onto a nanostructured surface, the first event that takes place is the cytoskeleton arrangement (Curtis, 2005; Curtis et al., 2004; Das et al., 2008; Fok-Seang et al., 1998). Within the first five minutes post seeding, the actin aggregation occurred then within 20 minutes there microtubules align (Curtis, 2005; Curtis et al., 2004; Das et al., 2008; Fok-Seang et al., 1998). Another study showed that human corneal epithelieal cells align in the direction of 70nm wide grooves and ridges; however, when seeded onto a flat surface, they did not have a specific orientation (Teixeira et al., 2003).

Topographic effects have been investigated extensively for silicon and titanium and to a lesser extent PMMA (Kotov et al., 2009). Photolithography is the traditional method for modifying the surface topography of substrates, however, this technique is limited by the diffraction limit of light and therefore cannot produce structures on a nano-sized level (Blattler et al., 2006). Over the years, new techniques have been developed to create reproducible, high quality patterns at a low cost. These techniques include, extreme ultraviolent interference lithography, soft-lithographic techniques (i.e. replica molding and microcontact printing, nanoimprint lithography (NIL), nanosphere lithography (colloid lithography or colloidal block-copolymer micelle lithography), and nanostencil technique (Blattler et al., 2006; Das et al., 2008; Ding et al., 2010; Kriparamanan et al., 2006). Most of these techniques require a mask or master that contains the pattern to be printed; this mask may be reused many times. Optical

nanolithography is the most widely used and best established lithography technique available (Blattler et al., 2006). This technique uses ultraviolet (UV) light to create micropatterns thru an etching or lift-off process. In order to create patterns on a nanoscale level, the extreme ultraviolet interference lithography (EUV-IL) technique is used(Blattler et al., 2006). This method generates patterns with high fidelity, which are highly reproducible and can cover an area as large as $3x3mm^2$. Microcontact printing uses a stamp made out of a soft, flexible polymer, therefore allowing application to a rough or curved substrate (Blattler et al., 2006). NIL is cheap and fast, so it can produce many test surfaces quickly (Cogan et al., 2006). It is easy to produce patterns smaller than 10nm because, the resolutions of NIL samples are not dependent on diffraction or scattering.

4.2 Nanopatterning Effect on Brain Cells

As stated earlier, the proximity of the neuron to the electrode determines the strength of the signal captured, therefore it is imperative to find methods to attract, adhere, and preserve neurons near recording sites. There are numerous methods for enhancing neuronal attachment, including the coating of cell adhesion proteins, such as collagen and fibronectin, or even polypeptides such as RGD. Ignatius et al found that coating cover slips with poly-d-lysine and laminin, neurons attached, spread and grew much better compared to uncoated surfaces (John et al., 2001; Polikov et al., 2005). Furthermore, it has been found that regardless of the surface underneath; neurons will grow on top of astrocyte monolayers in culture (Liberto et al., 2004; Polikov et al., 2005; Theil et al., 2005). Neuronal processes have been found to extend along the tracks provided by the astrocytes. Therefore, in order to potentially block the negative components found in the glial cell response, astrocytes would need to be attracted and adhered onto the electrode surface (Duffy et al., 2000; Polikov et al., 2005). Hence, the goal of neural

electrode fabrication is to find a material surface that will maintain neurons proximity to the recording surface, minimize astrogliosis, and eliminate chronic microglial activation (Polikov et al., 2005).

Nanofabrication of nanoelectrode arrays is being pursued in the field of neuronal electrophysiology in order to increase sampling capabilities (Blattler et al., 2006). By having a larger electrode surface area, through micro/nano-patterning, the electrode will be more accessible to ions, therefore, greatly increasing the capacitative component (Kotov et al., 2009). Neural cell function, such as neurite alignment, has been shown to be affected by the topography of materials. Table 2 summarizes selected literature studying the effect surface topography has on neural cells. Micropattterning has been shown to guide neuronal cell growth in neuronal implants and *in vitro* neural networks for tissue engineering applications (Blattler et al., 2006). Nanofabrication has promise to better understand cell behavior by mimicking the nano-world around the cell created by the nanotopographies of the ECM and the nanochemistry that composes the cell membrane (Blattler et al., 2006). It is the ability of a nanomaterial to mimic the roughness of natural tissue that is so interesting when designing optimal implants for the central nervous tissue. In fact, studies have shown that select proteins (i.e. fibronectin and vitronectin) adsorb more on nanomaterials compared to smooth materials of the same chemistry. This protein adsorption is the initiator of better cell adhesion, alignment, and outgrowth of neurites (Rose et al., 1985). It has been proposed that the uncontrolled, non-specific interactions between biological molecules and an implant are the cause for device failure. The rejection of an implant due to immune reactions, the short circulation time of drug-delivery particles, and the false response of biosensors are often caused by the non-specific adsorption of proteins (Blattler et al., 2006). Moreover, it has been shown that the proteins adsorbed to nanomaterial surfaces

may expose more amino acid binding sequences than proteins adsorbed to conventional materials, consequently allowing for greater cell adhesion. (John et al., 1999; Rose et al., 1985).

Webster et al found that when vitronectin is adsorbed onto nanophase alumina, there was protein unfolding, therefore exposing adhesion binding sites, such as the Arginine-Glycine-Aspartic Acid-Serine (RGDS) sequence (John et al., 1999; Rose et al., 1985) . In another study, they showed that there was less adhesion and proliferation of astrocytes and fibroblasts on carbon nanofibers compared to carbon fibers with diameters not in the nanoscale (Petrossians et al., 2011; Rose et al., 1985). Studies done by Shain et al found that astrocytes prefer to grow and adhere onto patterned surfaces of varying dimensions over smooth silicon surfaces *in vitro* (Kriparamanan et al., 2006; Szarowski et al., 2003). They used photolithography and microcontact printing to deposit hydrophobic and hydrophilic self assembling monolayers of organosilanes. Seil et al studied the astrocyte adhesion and proliferation on zinc oxide nanoparticle polyurethane composites. They found that there was a significant decrease in astrocyte adhesion and proliferation when there were more zinc oxide nanoparticles on the surface (Rose et al., 1985). This is believed to occur for several reasons. First, the nanoscale surface features better imitate the nanoscale protein rich environment of the ECM found *in vivo*. Second, the surface area of the nanoscale roughness samples is much larger, therefore allowing for more interaction between the cells and proteins on the surface. Third, nanomaterials have more of a surface energy than flat surface due to their increase in grain boundaries. This increase of surface energy is thought to not only increase the amount of protein adsorption, but the conformation of the proteins adsorbed as well (Rose et al., 1985).

Johansson et al found that axons can be guided by imprinted nanosized patterns, down to 100nm and that axons grew on top of the ridges rather than inside of the grooves of the pattern

(Cogan et al., 2006). They correlated this with previous studies that showed cells like to grow uphill, negative curvature, over downhill, positive curvature (Cogan et al., 2006). In the study performed by Wu et al, they used 3-D structures made from SU-8 with depths of 100um or aspect ratios greater than one. They found that they could promote SH-SY5Y human neuroblastoma cells to maintain a resting membrane potential on a 3-D microwell network meshwork compared to flat SU-8 substrates. Their findings suggest that cellular function may be controlled through topography engineering (Wu et al., 2006). They used the following dimensions: 50-um wells (diameter) with center-to-center spacing of 55-um, 100-um wells with a center-to-center spacing of 110-um, 100-um wells with center-to-center spacing of 190-um connected by a 10-um wide microchannels all having 100-um depths. These dimensions were used because even the smallest diameter was large enough to have the cells easily fit during plating. They found that compared to flat surfaces, cells on the patterned SU8 exhibited a cell resting membrane potential.

Table 2. Neuronal Cells on Patterned Surfaces

Material	Fabrication Technique	Feature Type	Width/ diameter	Depth/ height	Other Size	Cell Type	Effects
polystyrene	Nd:YAG polarized laser radiation at 266nm	ridge/ groove		30-40nm	210nm (period)	C6 glioma	Ordered and continous nanostructures can pattern cells, guide cell alignment, and orient growth along definite directions (Zhu, Zhang et al. 2004).
polystyrene	photolithography and solvent casting	ridge/ groove	10um	3um	20um (pitch)	rat Type-1 astrocytes (primary)	85% of astroglial alignment in the direction of the grooves (Recknor, Recknor et al. 2004).
PMMA	nanoimprint lithography	grooves	100-400nm	300nm	100-1600nm (spacing)	adult mouse sympathetic and sensory ganglia	Axons displayed contact guidance on all patterns. Nerve cell processes preferred to grow on ridge edges and elevations in the patterns rather than in grooves (Johansson, Carlberg et al. 2006).
silicon	photolithography	pillars	0.5-2.0um (d)	1.0um	1.0-5.0um (gaps)	LRM55 astroglial cells	70% of cells preferred pillars over smooth silicon. Cells made contact with the tops of the pillars and did not reach the down into the spaces between the pillars (Turner, Dowell et al. 2000).
zinc oxide (ZnO) nanoparticles on polyurethane (PU)	Mixing PU and ZnO nanoparticles	nanoparticles	~60nm (d)			CRL-2005 rat astroctes	Astrocyte adhesion was reduced on ZnO nanoparticles/PU compsites compared to pure PU (Seil and Webster 2008).

Material	Fabrication Technique	Feature Type	Width/ diameter	Depth/ height	Other Size	Cell Type	Effects
Carbon nanofibers	catalytic and chemical vapor deposition	fibers	60-200nm (d)			CRL-2005 rat astroctes	Decrease in astrocyte adhesion and cunction, which may lead to a decrease in glial scar tissue formation (McKenzie, Waid et al. 2004).
silicon substrates with DETA and OTS organosilanes	microcontact printing	arrays of hexagonal features	5-50um			LRM55 astroglial cells	As feature size increased, cell adhesion increased (Kam, Shain et al. 1999).
silicon	chemical (HF) etching	surface roughness	2-810nm (Ra)			rat Nigral cells	Cells survuved for over 5 days with normal morphology and expressed neuronal TH when grown on surfaces with average roughness (Ra) from 20-50nm. Cell adherence was adversely affected at Ra less than 10nm and greater than 70nm (Fan, Cui et al. 2002).
silicon	chemical etching	surface roughness	10-250nm			primary cortical neurons	Optimum surface roughness range of 20-100nm that promotes cell adhesion and longevity (Khan, Auner et al. 2005).

Material	Fabrication Technique	Feature Type	Width/ diameter	Depth/ height	Other Size	Cell Type	Effects
gold and porous anodic alumina (PAA)	electrodeposition	nanopores and nanopillars	nanopillar: 200nm (d); nanopore: 200nm	nanopillar: 2um	nanopillar: 70nm (spacing)	PC12	Cells were spatially aware of nanoscale structures and responded differently to nanopores and nanopillars. Cells on nanopores and nanopillars had fewer and shorter neurites compared to those on smooth surfaces. Cells on nanopores developed more and longer neurites than those on nanopillars (Haq, Anandan et al. 2007).
silicon	photolithography	pillars	0.5-2.0um	1um	0.5-5.0um (gaps)	neurons from hippocampi rat embryos	Neuron growth on pillare surfaces exhibited alignment to pilar geometries with the smallest gap sizes. Neurite lengths were significantly longer on pillars with the smallest gaps and 2um pillar widths (Dowell-Mesfin, Abdul-Karim et al. 2004).
PDMS	soft lithography	gratings	350nm-10um	350nm	700nm-20um (pitch)	human mesenchymal stem cells	Nanotopography showed a stronger effect in enhancing upregulation of neuronal marker expression, compared to biochemical cues and unpatterned surfaces. Showed significance in nanotopography in directing differentiation of adult stem cells (Yim, Pang et al. 2007).

CHAPTER 5

5.1 Characterization of Astrocyte Reactivity and Gene Expression on Biomaterials for Neural Electrodes

It is crucial that materials used for neural electrode devices, intended for long-term *in vivo* purposes, to go through meticulous investigation of biocompatibility requirements. There is a lack of research studying astrocyte reactivity *in vitro* on multiple materials used for neural electrodes. The current study was designed to investigate the astrocyte proliferation, viability, morphology, and gene expression in order to assess the reactive state of the cells on different material surfaces. Although platinum and silicon have been extensively characterized both *in vivo* and *in vitro* for their biocompatibility with neuronal cells, this study utilized the novel usage of PMMA and SU8 in neural electrodes by comparative analysis of materials' biocompatibility.

5.2 Methodology

5.2.1 Material Fabrication

SU-8 samples were fabricated by spincoating SU-8 photoresist (2025). SU-8 was coated using the suggested parameters in Microchem website for 1 um thickness, onto silicon wafers. Thin film of platinum was deposited on silicon substrate using electron beam evaporation (Electron Beam Evaporator-BJD 1800), with titanium as an adhesion promoter and subsequent deposition of platinum onto the substrate. Evaporation was performed at a pressure of 1.0 _ 10-7 Torr, and a rate of 0.5 Å/sec for platinum and 1 Å/sec for titanium. The thickness of the film was 100nm and 10 nm for platinum and titanium respectively. The wafers were then cut into 1 cm^2pieces. PMMA sheets were cut into 1 cm^2 pieces. Polystyrene cover slips were employed as a control surface. Materials were washed with a Ultraomet 2003 Sonic Cleaner (Buehler, Bluff, IL) in ethanol, followed by distilled water for 15 minutes in each solvent. Platinum, silicon and

SU-8 samples were autoclaved for 30 minutes at 121^{o}C, before cell seeding all of the samples were sterilized under UV light.

5.2.2 Surface Chemistry Characterization

Energy-dispersive X-ray spectroscopy (EDX) was used to characterize the elements found in SU8. This technique was used to observe if antimony (Sb), a toxic salt used as a photo acid generator in the fabrication process, was present. To quantify the amount of antimony present in SU8, the surface composition of the deposited films was analyzed by X-ray photoelectron spectroscopy (XPS) using monochromatic AlKa radiation in a Perkin Elmer model S500 XPS Spectrometer.

5.2.3 Cell Cultures

This study utilized C6 rat astrocytoma cell line (ATCC, Manassas, VA). The cells were maintained in a F-12K medium supplemented with 10% horse serum, 2.5% fetal bovine serum (FBS), and 1% antibiotics-antimycotic. The cells were kept in a humidified incubator with the following setting conditions: 90% humidity, 5% CO_2 and 37.8^{o}C. The media was changed twice a week. Cells were detached using trypsin and then centrifuged at 1000rpm. Following which, the cells were resuspended in culture media, stained with Trypan blue and counted using a hemocytometer. There were 5000 cells in 100µl droplet of culture media loaded onto each sample in a 24 well plate. Following three hours of incubation at 37^{o}C, 500µl of culture media was added to each well. The culture media was changed twice a week during the study.

5.2.4 Proliferation Assay

The methylthiazolyldiphenyl tetrazolium bromide (MTT) colorimetric assay was employed to determine the number of cells and the rate at which they proliferated at days 1, 3,

and 7 post seeding. At each time point, 0.5 mg/mL MTT reagent was added to the culture medium and reincubated for 5 hours in the dark at 37^{o}C until the yellow MTT was reduced to purple formazan crystals. The culture media was removed carefully, so as to not disturb the formazan crystals, and replaced by dimethyl sulfoxide (DMSO), which solubilized the formazan crystals and cells. Absorbances were read at 570nm and 650 nm in a microtiter plate reader. The optical densities were calculated by subtracting the 650nm reference wavelength from the 570nm absorbance reading. To measure the approximate number of cells on the given test days, a growth curve for C6 cells was also generated by performing a MTT assay on a graded series (range from 2,000 to 1,500,000 cells) of cells plated on polystyrene culture dishes.

5.2.5 Real Time PCR

Real time PCR was used to measure gene expression from the different samples relative to the control surface (polystyrene samples). The total RNA from the samples was extracted on days 3 and 7 post seeding with Trizol (Invitrogen, Carlsbad, CA) following the manufacturer's protocol. The RNA concentration and purity was determined using a spectrophotometer through UV absorbance at 260nm and 280nm. Reverse transcriptase using the oligo$(dT)_{20}$ primer converted the mRNA to a cDNA template using a thermal cycler (Mastercycler Gradient, Eppendorf, Hauppauge, NY). For PCR analysis, we used cDNA equivalent to 50ng of total RNA. Specific primer pairs (Table 3) for proliferation, mitogen-activated protein kinase kinase 1 (MAP2K1) and astrocyte activation, glial fibrillary acidic protein (GFAP) were employed in the study. As an internal control, we used the house-keeping gene glyceraldehyde-3-phosphate dehydrogenase (GAPDH). The PCR master mix included 1 x SYBR® Green (Applied Biosystems, Foster City, CA), and forward and reverse primers (0.4μM each). A 96-well optical plate was used to put the master mix and cDNA templates into it. The plate was capped and

spun in order to settle all of the contents. The 7500 Fast Real-Time PCR System (Applied Biosystems, Foster City, CA) was used to read the plate. The following profile was used: 50°C for 2 min, 95°C for 10 min, and 40 cycles of 95°C for 15s and 60°C for 1 minute. Threshold cycle (Ct) values for each sample and primer pair were obtained and analyzed with the delta-delta (△△) Ct method(Livak and Schmittgen, 2001; Schmittgen and Livak, 2008) in order to calculate the fold change (R) in each target gene. The following equations were used:

$$\triangle Ct = Ct_{sample} - Ct_{GAPDH}$$

$$\triangle\triangle Ct = \triangle Ct_{test\ surface} - \triangle Ct_{control\ surface}$$

$$R = 2^{-\triangle\triangle Ct}$$

Table 3. Primer sequences for real-time PCR used in biomaterials study.

Cells	Category	Gene	Primer Sequence
C6 rat astrocytoma cells	Housekeeping gene	GAPDH	5'-TGGCCTTCCGTGTTCCTACC-3' (F)
			5'-AGCCCAGGATGCCCTTTAGTG-3' (R)
	Proliferation gene	MAP2K1	5'-TTCAAGGTCTCCCACAAGCCATCT-3' (F)
			5'-TTGATCCAAGGACCCACCATCCAT-3' (R)
	Activation gene	GFAP	5'-GTTGTGTTCAAGCAGCCTGG-3' (F)
			5'-CCAGTGAGTAAAGGTGACAG-3' (R)

5.2.6 Viability Test

In order visually observe the morphology and viability of the cells on the different surfaces; we used the Live/Dead® viability/cytotoxicity assay (Invitrogen, Carlsbad, CA). Calcein AM (2μm in phenol red free DMEM) was used to stain the live cells a green fluorescent color that can be seen using an emission filter (FITC) of ~488. Ethidium homodimer (EthD-1) (4μm in phenol red free DMEM) was used to stain the dead cells a red fluorescence, which can be seen using an emission filter at ~528. The samples were incubated in the Live/Dead stain for 20-30 minutes inside the incubator (37°C). Thereafter, the samples were mounted onto slides

using Prolong Gold antifade mounting gel (Invitrogen, Carlsbad, CA) and viewed under a Zeiss Axio Observer Inverted Microscope (Carl Zeiss Inc). Images for each sample were taken in the same location with both the red and green filters.

5.2.7 Cell Morphology Analysis

Fluorescence staining was utilized to image the cells' cytoskeleton along with the nucleus. The cells were washed in phosphate buffered saline (1X PBS) and fixed in 4% paraformaldehyde for 20 minutes. The cells were washed in PBS, and then permeablized by incubation for 25 minutes in 1X PBS containing 0.25% Triton X-100. The cells washed, blocked with 1% fetal bovine serum (FBS) for 25 minutes and washed again with 1X PBS. Cells were stained with Rhodamine Phalloidin in 1X PBS (Invitrogen, Carlsbad, CA) for 20 minutes at room temperature in the dark. Double staining of the nucleus was done with 2μg/mL of 4',6-diamidino-2-phenylindole (DAPI; Sigma-Aldrich, St. Louis, MO) for 20 minutes at room temperature in the dark. Thereafter, the samples were mounted onto slides using Prolong Gold antifade mounting gel (Invitrogen, Carlsbad, CA) and viewed under a Zeiss Axio Observer Inverted Microscope (Carl Zeiss Inc). Images for each sample were taken in the same location with both the red and DAPI filters.

5.2.8 Image Analysis

Image J software was used to quantify the number of live cells versus the dead cells, calculate the aspect ratio and the projected area of the cells. Each image was first converted to an 8-bit grayscale, following which a threshold binary image was created. An average area of stained live and dead cells was measured and used to set a global scale of a particle size (average area of stained dead cell 50μm^2 and stained live cell 80μm^2). Thereafter, the cells were counted

using the analyze particles function. The following formula was used to calculate the percentage of live and dead cells:

$$\% \text{ of live cells} = \frac{\#\text{ of live (or dead) cells}}{\text{sum of total cells (live + dead)}} * 100$$

The aspect ratio of the nucleus was used to measure the spreading of cells. It is calculated by taking the ratio of the major axis to the minor axis of each cell. A perfect circle has an aspect ratio of 1 and a line has an aspect ratio of infinity. The projected area of the cell's nucleus was measured by taking the total area of the nucleus. The circularity of the nucleus was measured by taking the ratio of the area of the nucleus over the area of a circle. A perfect circle will have a circulatory of 100%.

5.2.9 Statistical Analysis

All of the data are presented as a mean ± standard error of the mean. Experiments were performed in triplicates and repeated four independent times. There were minimally 15 samples analyzed per group. PASW software (version 18.0) was utilized for statistical analysis. In order to evaluate statistical significance between the materials groups over time with the MTT assay, aspect ratio, projected area and circularity a one way analysis of variance (ANOVA) was utilized. A nonparametric statistical analysis was used to test for statistically significant differences between the different material groups over time for the RTPCR studies and the Live/Dead analysis, because parametric statistical methods could not be completed due to insufficient power from a small sample size, the exact tests, which were designed for small, sparse, heavily tied, or unbalanced data and the validity of the corresponding large sample theory

is in doubt, were conducted in order to be able to make reliable inferences by computing exact p values for a very wide class of hypothesis tests, including one-, two-, and K sample tests, tests for unordered and ordered categorical data, and tests for measures of association.

5.3 Results

5.3.1 Surface Chemistry Characterization

Energy-dispersive X-ray spectroscopy (EDX) found that there was some antimony on the surface of the SU-8 substrate (Figure 13). However, X-ray photoelectron spectroscopy (XPS) was not able to detect antimony during both compositional survey scans at a pass energy of 100 eV and high-resolution detailed scan at a pass energy of 25 eV. This indicated that the presence of antimony was bellow the detection limit which is less than 1% of the total chemical composition of SU-8.

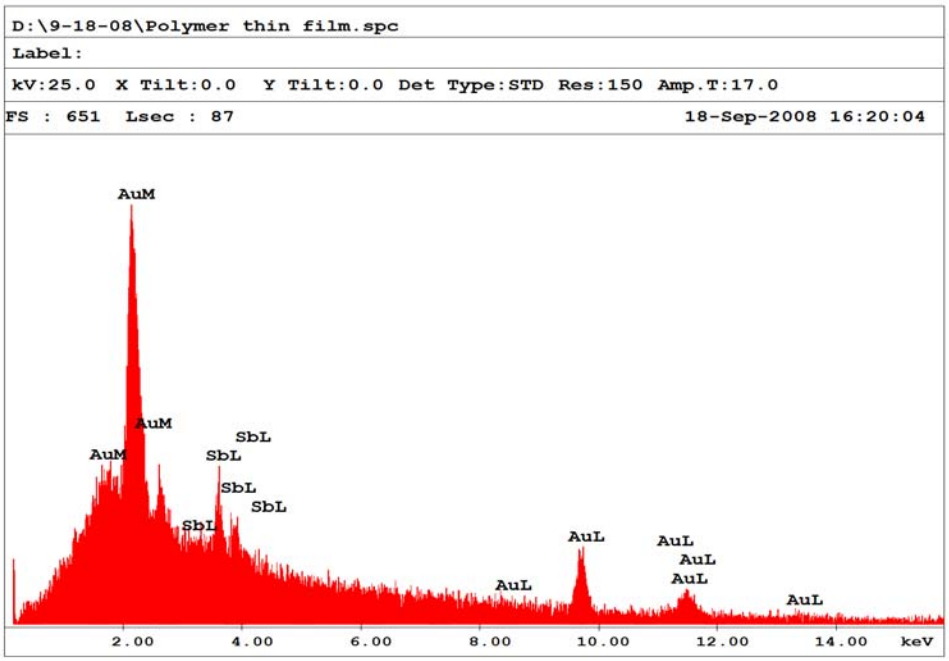

A

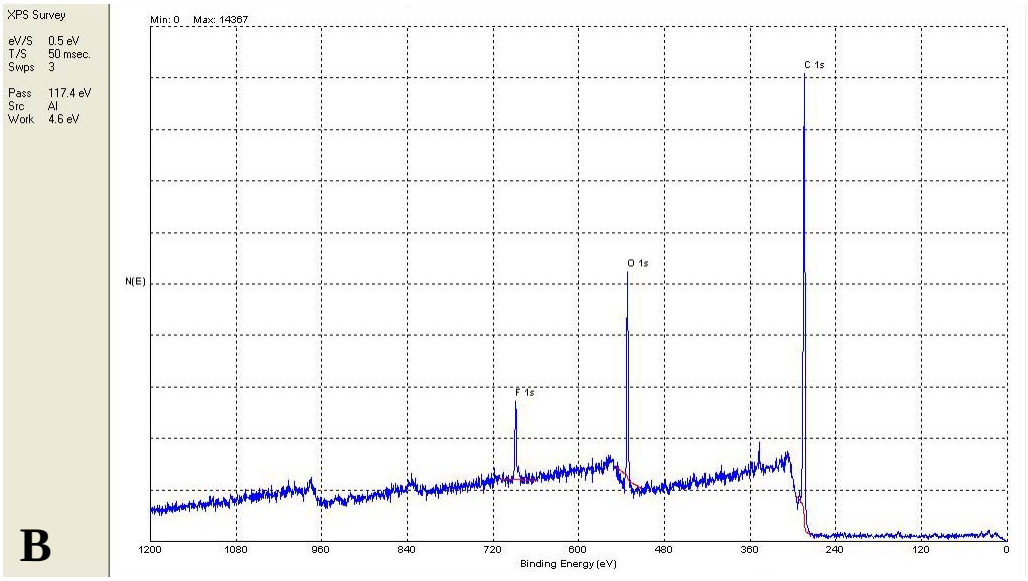

Figure 13. A) EDX of SU-8 shows low levels of antimony on the surface of the substrate. B) XPS survey scan at pass energy of 100eV was not able to detect any antimony.

5.3.2 MTT Proliferation Assay

The proliferation assay results revealed significance between the number of cells on the different material surfaces at three days (Figure 14). PMMA had significantly ($p<0.005$) less cells on its surface compared to SU-8, silicon and platinum surfaces on day one. Moreover, it was found that SU-8 had a significantly ($p<0.005$) higher volume of initial cell attachment in comparison to silicon, platinum and PMMA on day one. In fact, there were twice as many cells adhering onto SU-8 compared to the other materials. There were significantly less ($p<0.005$) cells on PMMA compared to the control on day three. Additionally, there were significantly less ($p<0.005$) cells on silicon compared to the other three material surfaces. Day seven revealed significantly fewer ($p<0.005$) cells on PMMA compared to platinum. Moreover, results showed the cells proliferated at significantly different rates on the different materials (Figure 15). The growth rates of the astrocytes on SU-8, silicon and platinum were found to be significant between all measured intervals ($p<0.05$ on SU-8 between day one and day three and $p<0.005$ for

all other time intervals). Cells seeded on PMMA were found to have a steady growth rate, similar to the control.

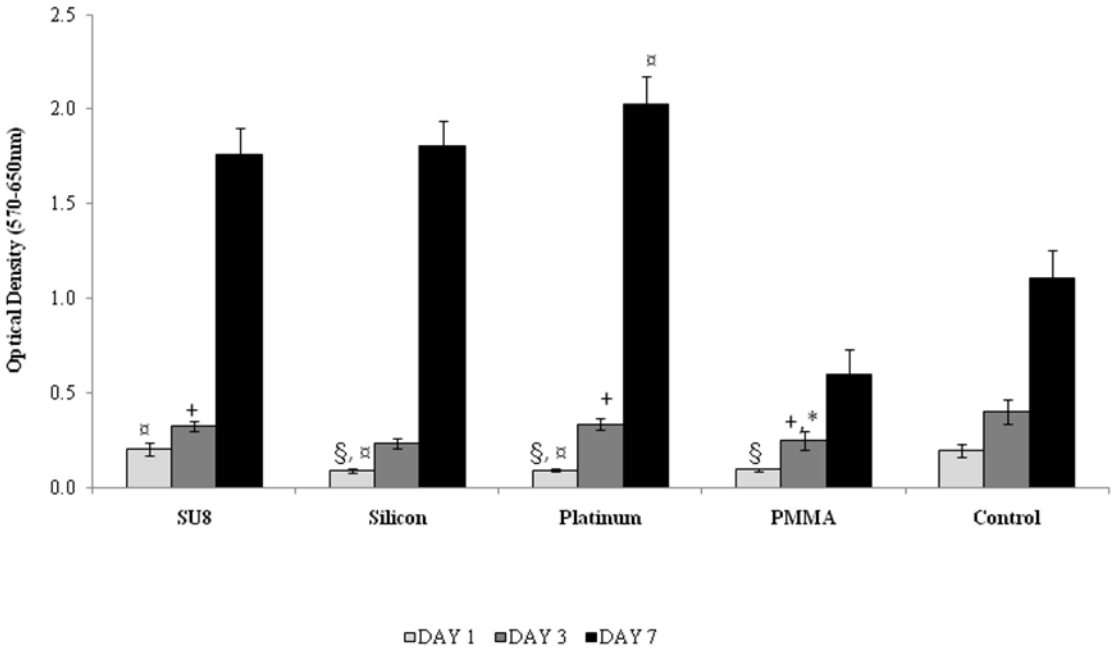

Figure 14. MTT Proliferation assay. PMMA had significantly fewer cells attach by day one compared to the other test materials (SU8, silicon, and platinum) surfaces, while SU8 had significantly highest amount of cells attach by day one. *p <0.05 compared to control, ¤p <0.05 compared to PMMA, §p <0.05 compared to SU8, +p <0.05 compared to silicon.

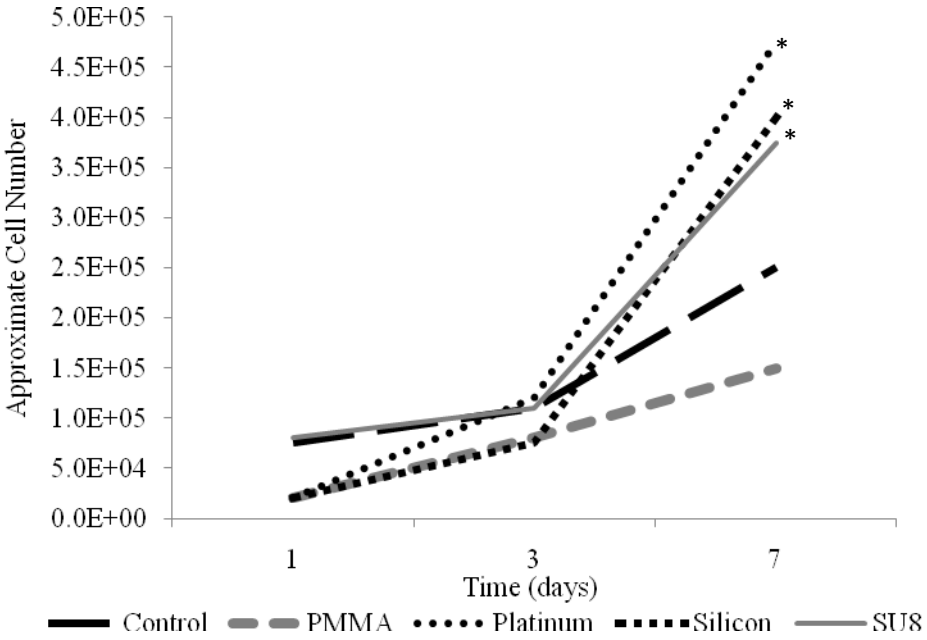

Figure 15. Growth rates of astrocytes on biomaterials. The growth rates of astrocytes on SU8, silicon and platinum were found to be significant between all measured time intervals *p <0.05.

5.3.3 Relative Gene Expression

Astrocyte MAP2k1 relative gene expression was significantly lower ($p<0.05$) on all surfaces compared to the control surface at both days three and seven (Figure 16). Moreover, compared to the other test surfaces, cells on SU-8 had significantly ($p <0.05$) less MAP2k1 gene expression on day three. Similarly, there was a significantly lower amount of MAP2k1 gene expression from cells on PMMA compared to those on platinum and silicon on day three. MAP2k1 gene expression from cells on silicon on day seven were significantly less ($p <0.05$) compared to the control, platinum and PMMA.

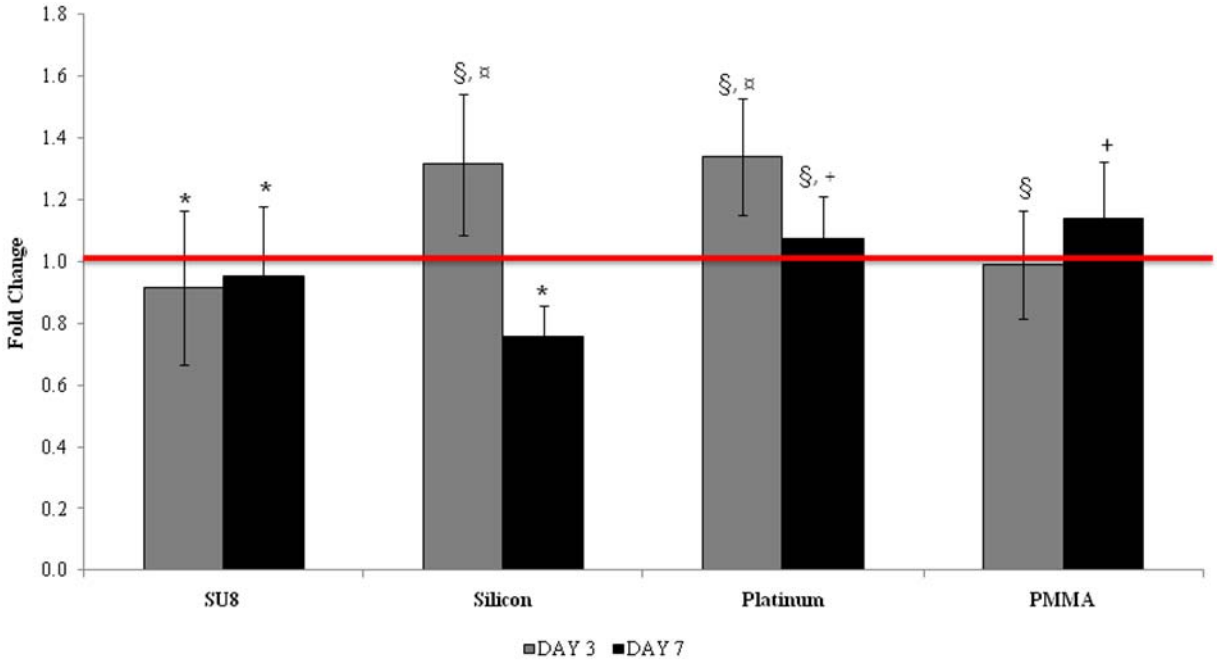

Figure 16. RTPCR MAP2k1 relative gene expression. The control is represented as the red line *p <0.05 compared to control, ¤p <0.05 compared to PMMA, §p <0.05 compared to SU8, +p <0.05 compared to silicon.

On day three, there was significantly less (p <0.05) GFAP relative gene expression found by cells growing on PMMA compared to those growing on the SU-8 and silicon surfaces (Figure 17). By day seven, there was significantly less (p <0.05) GFAP relative gene expression from PMMA compared to silicon and platinum surfaces. Furthermore, on day seven, there was significantly less (p <0.005) GFAP relative gene expression found by cells growing on SU-8 compared to those growing on the control, silicon and platinum surfaces.

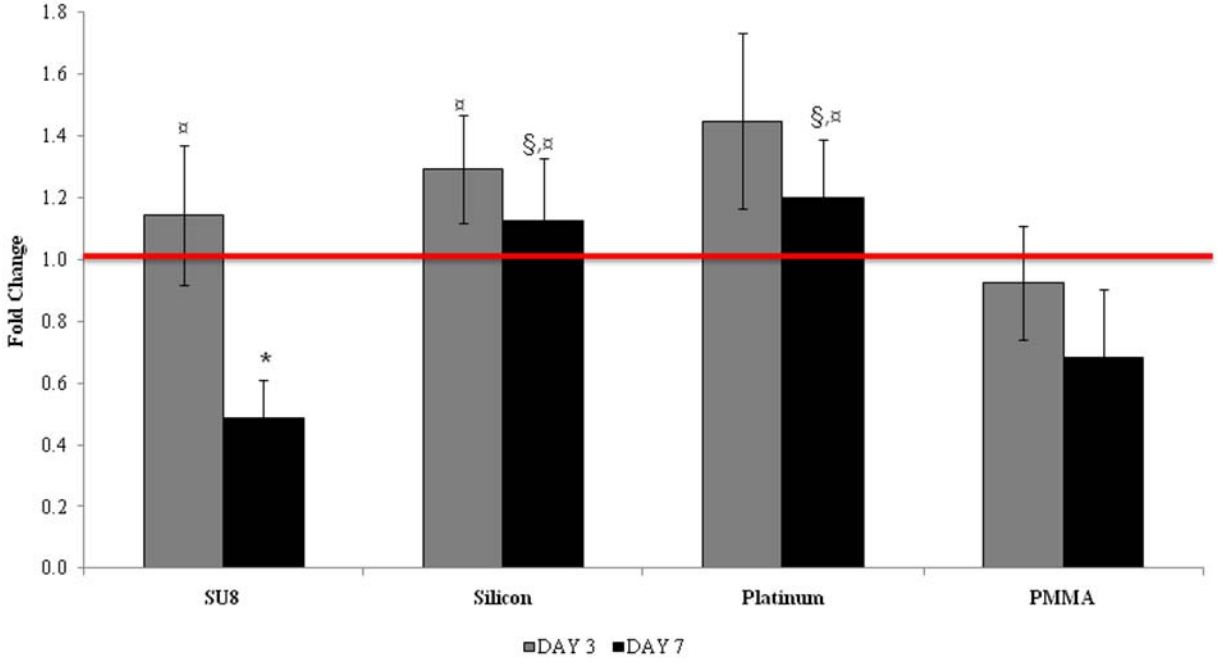

Figure 17. RTPCR GFAP relative gene expression. The control is represented as the red line. *p <0.05 compared to control, ¤p <0.05 compared to PMMA, §p <0.05 compared to SU8.

5.3.4 Cell Morphology

In order to assess the morphology of the cells quantitatively, the aspect ratio, projected area and the circularity of the cells' nucleus were calculated (Figure 18). Compared to the control, all of the test materials showed a significant difference (p <0.005) of the cells' nucleus aspect ratio and projected area on all three time points. The nucleus of cells on platinum had the largest projected area on day three compared to the other materials. Moreover, the projected area of the nucleus on PMMA resembled most to that of cells on the control surface. It was also found that the cells' nucleus aspect ratio on PMMA and SU-8 were similar to that of cells on the control surface on all three time points measured. The aspect ratio of the cells' nucleus on platinum was the highest on day one. In addition, silicon showed the highest cell nucleus aspect ratio on day three. There was not any statistical significance found when comparing the

circularity of the astrocytes' nucleus on the different materials. Cells on platinum had the lowest circularity of their nucleus on days one and seven, whereas cells on PMMA had the highest circularity on days one and three.

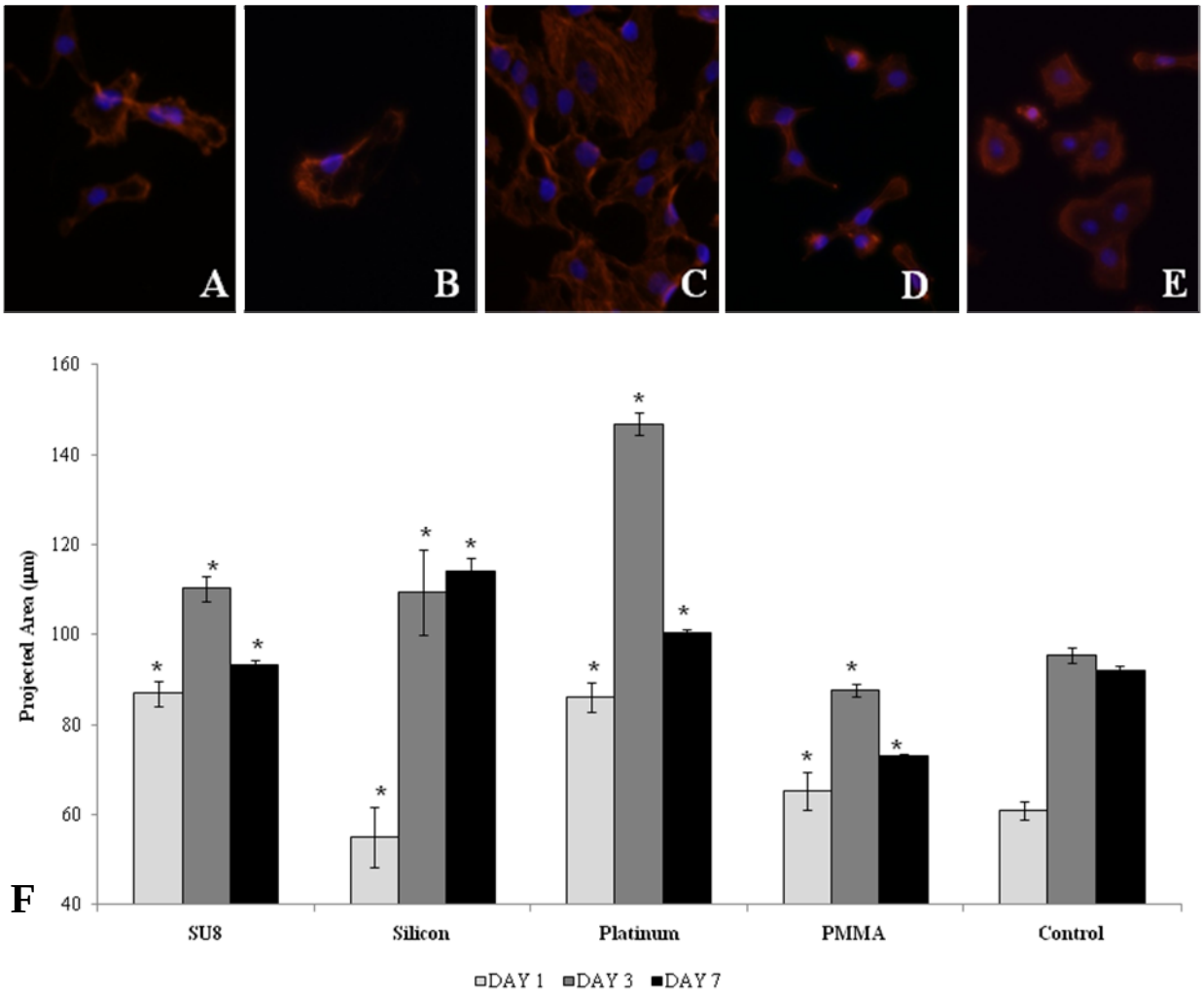

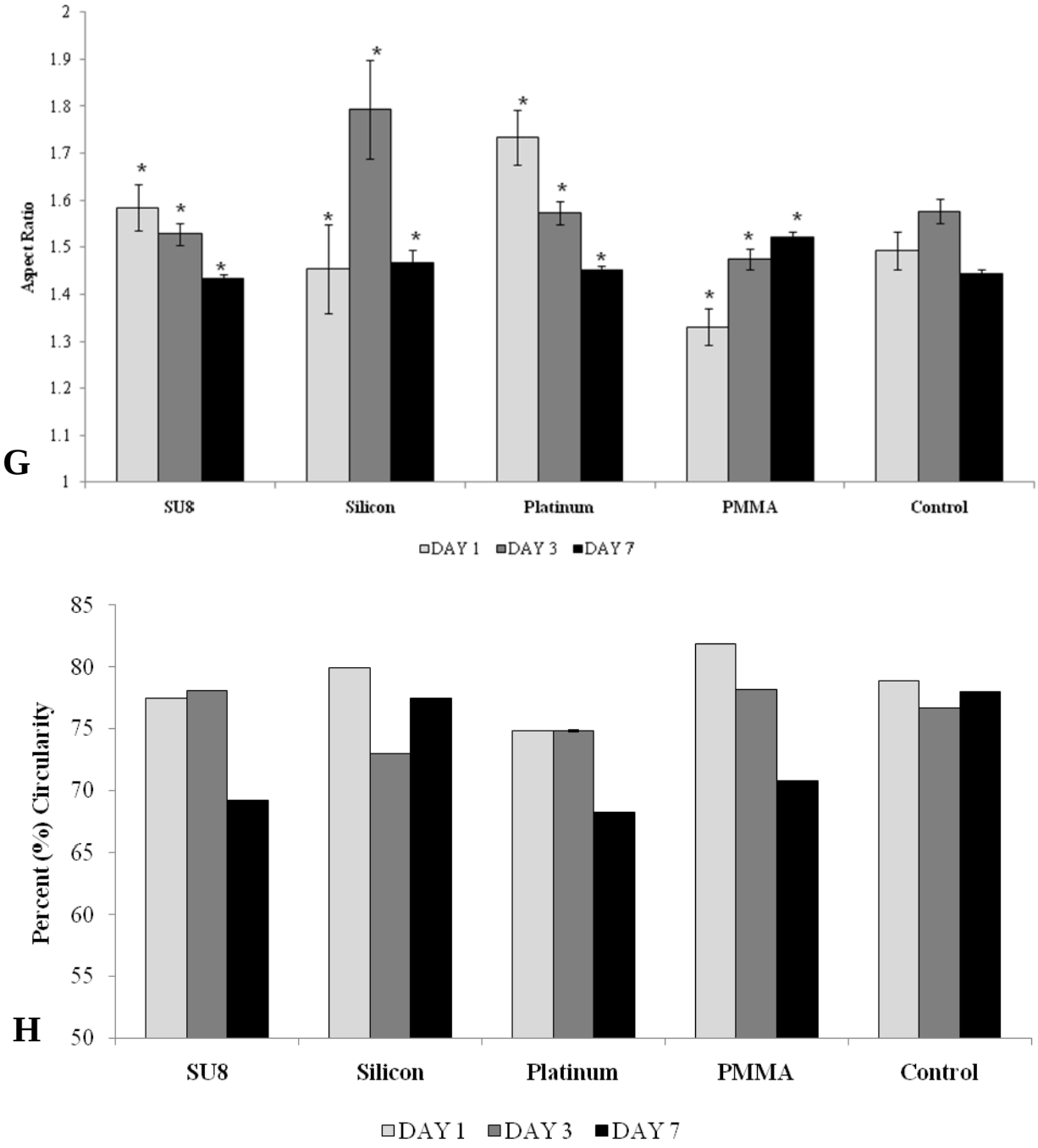

Figure 18. A-E) Rhodamine phlalloidin cytoskeleton stain double stained with DAPI for cell nucleus on day 3 (40X) of cells on SU-8, silicon, platinum, PMMA and control surfaces respectively. F) projected area of cells' nucleus G) aspect ratio of cells' nucleus H) circularity of the cells' nucleus *p <0.005 compared to the control.

5.3.5 Viability Assay

Astrocytes on platinum had significantly higher ($p < 0.05$) viability on platinum surface compared to the control, PMMA and silicon on day three post incubation (Figure 19). Moreover, cells growing on PMMA had significantly less ($p < 0.05$) viability compared to those on SU8 on day three. However, by day seven, astrocytes on PMMA were significantly ($p < 0.05$) more viable than on silicon. Overall, there were fewer than 10% dead cells on any material surface by seven days.

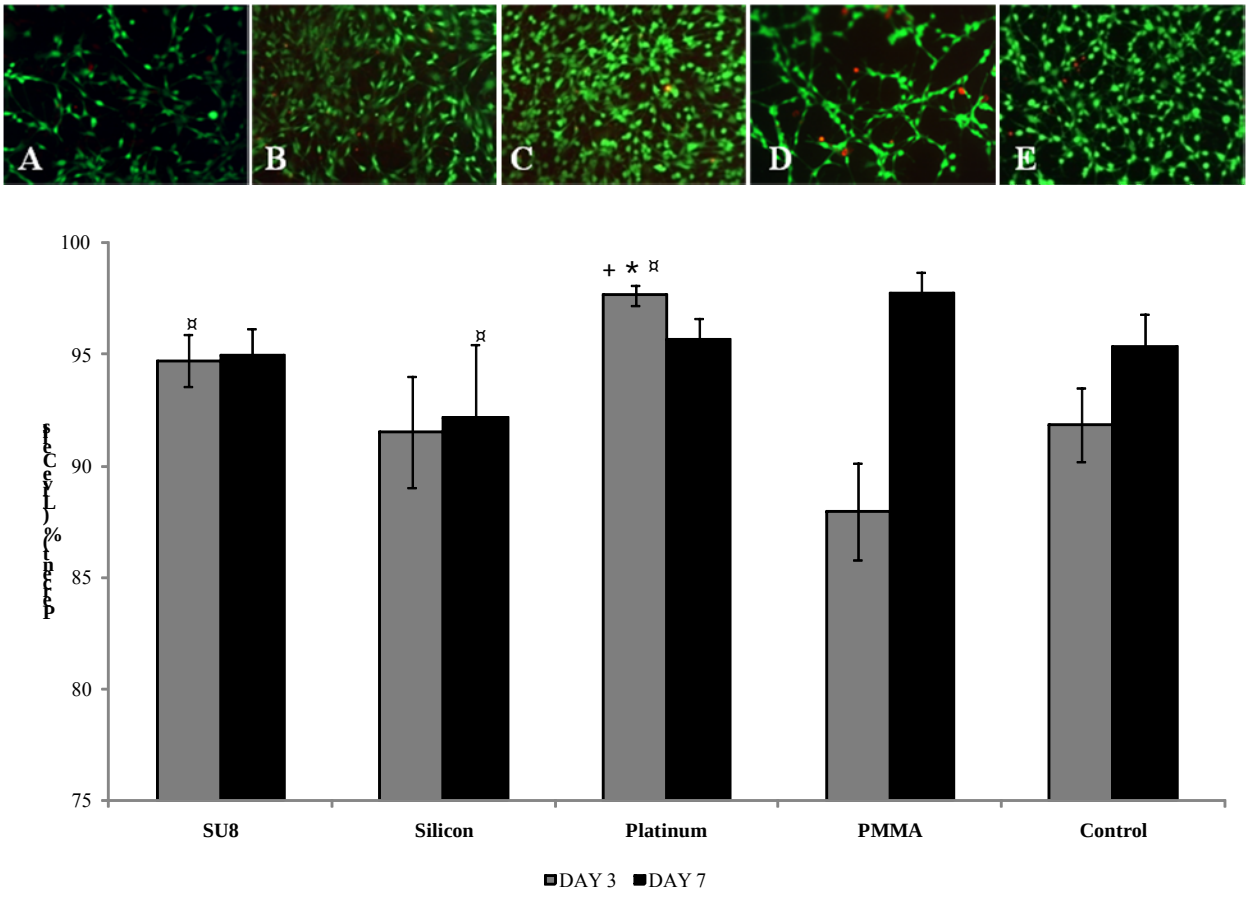

Figure 19. Live/Dead images taken on day 3 (20X) a) SU-8 b) silicon c) platinum d) PMMA e) control polystyrene f) viability results of cells on materials surface on days 3 and 7 days *in vitro*. *p <0.05 compared to control, ¤p <0.05 ompared to PMMA, +p <0.05 compared to silicon.

5.4 Discussion

In summary, this study showed astrocyte behavior on PMMA to be very similar to that on the control surface. Cells growing on platinum and silicon were the most reactive compared to other surfaces. Moreover, SU-8 did not show any evidence of cytotoxicity. As previously mentioned, some of the characteristics of reactive astrocytes include, hypertrophy, hyperplasia, upregulation of GFAP, and irregularly shaped nuclei. This study utilized these predefined characteristics of a reactive astrocyte through a combination of techniques. As a result of this study, we have classified guidelines to create a biocompatible neural electrode. Cytotoxicity testing is a good preliminary step in evaluating the biocompatibility of a medical device (Kotzar et al., 2002). Therefore, an increase in cell death on a biomaterial characterizes that biomaterial as incompatible. Since hyperplasia indicates astrocyte reactivity, a linear proliferation rate identifies unreactive astrocytes(Polikov et al., 2006; Polikov et al., 2005; Turner et al., 1999). It has been well established that an increase in GFAP expression is a result of an activated astrocyte (Bhandari et al., 2010; Negi et al., 2010a; Polikov et al., 2005). The cells' nuclei have to maintain a round shape with an area no more than 100 μm^2. Normal, inactivated astrocytes have round cell bodies with a diameter of 10-20μm, therefore large, irregularly shaped nuclei indicate an activated astrocyte (Bruce Alberts, 2008; Eric J. Nestler, 2001; Kühnel, 2003). Defiance of any of these guidelines may indicate an inflammatory response which results in classifying a biomaterial as incompatible.

Previous studies have found cytotoxic effects from SU-8(De Boeck et al., 2003; Vernekar et al., 2009), silicon(Kotzar et al., 2002; Szarowski et al., 2003) and platinum(Griffith and Humphrey, 2006) cultured with neuronal cells or implanted *in vivo*. In a study done by Griffith et al with *Rhesus macaque*, glial scarring was found around platinum wires implanted into the

motor cortex for periods up to three months and three years(Griffith and Humphrey, 2006). Results of our current study are evident of the astrocyte reactivity to platinum on an *in vitro* level. Astrocytes cultured on platinum had the highest levels of GFAP gene expression and the largest nuclei projected area on day three. Furthermore, the astrocyte's nuclei on platinum had the lowest circularity at all time points. The combination of these findings implies astrocyte reactivity on platinum (Bhandari et al., 2010; Polikov et al., 2005). Although silicon is commonly used in neural electrodes, our results indicate astrocyte reactivity to silicon, possibly explaining the limitations of current electrode design (Kotov et al., 2009; Zhong and Bellamkonda, 2008). Results of astrocytes on silicon are similar to those on platinum. Silicon had the second highest number of cells by day seven and second highest rate of proliferation, with platinum being the highest. Astrocytes on silicon had the lowest MAP2k1 expression by day seven, indication that the hyperplasia caused confluency on the surface. The lower cell viability on the silicon surface, compared to the other materials on day seven, is another indication of the cells reaching confluency in the silicon surface by say seven. Cells on silicon had the second highest GFAP expression, again with platinum being the highest on both days. It was interesting to note that the astrocytes on silicon had the smallest projected area on day one. This may indicate a lack of initial cell spreading on the materials. Moreover, the astrocytes' projected area and aspect ratio increased significantly from day one to day three, indication of hypertrophy, a sign of reactive astrocytes. PMMA and polysytrene are both considered biocompatible materials commonly used as substrates for mammalian cell culture (Ni et al., 2009). PMMA has been used for medical applications for a number of years due to its excellent tissue compatibility(Frazer et al., 2005). Our results found the cellular characteristics, reactions and growth rates of astrocytes grown on PMMA resembled closely to that of cells grown on the

control surface. Additionally, the astrocyte GFAP gene expressions of cells grown on PMMA were lower than the control, signifying a lack of astrocyte reactivity.

Material properties of SU-8 suggest that it could be used for a compatible neuron-based device(Wu et al., 2006). However, there have been several studies revealing cytotoxicity with SU-8, thus rendering it a controversial material for biomedical purposes (Vernekar et al., 2009; Wu et al., 2006). Kotzar et al performed an investigative study evaluating the biocompatibility of numerous bioMEMS materials, including silicon and SU-8. They found that these materials were not cytotoxic with mouse fibroblasts *in vitro*. Furthermore, another study they performed using rabbit muscle implantation lead them to classify these materials as non-irritants. However, when conducting aqueous physiochemical tests, they found that SU-8 leached detectable nonvolatile residues(Kotzar et al., 2002; Ni et al., 2009). Vernekar et al examined primary neuronal cell cultures from rats on various surface treatments of SU-8 for 21 days *in vitro*. They concluded that the current formulas of SU-8/SU-8 2000 are cytotoxic to primary neurons, thus rendering them incompatible. Vernekar found that he neurons had poor adhesion to the SU-8 surfaces and less that 10% of neurons survived when cultured adjacent to or on the SU-8 substrates. Moreover, they found toxins such as fluorine and antimony leaching from the SU-8 2000. These chemicals are typically found in the photo acid generator in the SU-8 2000 formula. It was noted that the neurons adjacent to the samples were dead(Vernekar et al., 2009). On the other hand, studies performed by Kisaalita's group concluded that SU-8 mictrostructures are viable platforms for cell culturing systems for cell-based biosensing against drugs and promoting human neuroblastoma cells' resting membrane potential(Wang et al., 2009; Wu et al., 2006).

Although studies have found cytotoxic elements in SU-8, our study shows otherwise. The XPS and EDX results indicate little to no cytotoxic chemical, antimony, in our SU-8

formula. There are few studies that raised concern about antimony leaching as possible cause of cytotoxicity (Cogan et al., 2009; Vernekar et al., 2009). However, the minimum acceptable amount of antimony for biomedical application of SU8 has not yet been determined. We found there was at least 93% viability of cells on SU-8 for up to one week *in vitro*, the initial adhesion of cells was strongest on SU-8, the proliferation rates were steady and consistent with the control, the morphology of the nucleus was consistent with the control, and GFAP was lowest on SU-8 day seven. The MTT assay revealed that the initial attachment of astrocytes to SU-8 was the highest. We found twice as many cells on SU-8 compared to the other material surfaces. Our observations suggest SU-8 to be biocompatible.

Studies have shown that PMMA reduces the adsorption of proteins by five to ten fold compared to polystyrene (Alaerts et al., 2001; Cogan et al., 2006). By using a polymer that minimizes the adsorption of proteins, they found that the chemical influence of the polymer on the cells was reduced(Alaerts et al., 2001). Proteins adsorb immediately after an implanted material comes into contact with physiological solutions. This protein adsorption facilitates the cellular interaction with the substrate surface. The number and strength of cells adhered to a substrate is inherently affected by the level of protein adsorption (Dupont-Gillain et al., 2004; Ni et al., 2009; Salakhutdinov et al., 2008). Our results found the fewest number of astrocytes on PMMA compared to any other surface, which could be explained by a low amount of protein adsorption on PMMA. Furthermore, there was 13% cell death on day three on PMMA surface most likely due to poor adhesion of cells on PMMA. It can be hypothesized that cells died on PMMA due to lack of adherence.

Surface hydrophobicity does have an effect on protein conformation, thus possibly making the protein's cell binding domain unavailable for cells to attach(Ni et al., 2009). SU-8

and PMMA are both hydrophobic materials, while silicon and platinum are hydrophilic(Burton and Bhushan, 2005; Shirtcliffe et al., 2004; Zisman, 1965; Zorba et al., 2006). Burton et al found that hydrophobicity is inversely correlated to adhesive strength; an increase in hydrophobic characteristics therefore reduces adhesive force(Burton and Bhushan, 2005). It is hypothesized that the cellular adhesive force on the SU-8 and PMMA was not strong. This is verified by the lack of cell spreading, indicated by the lowest aspect ratio and projected area from these two materials compared to silicon and platinum. Moreover, the results from the RTPCR MAP2k1 gene expression imply that the astrocytes on the SU-8 and PMMA substrates have room to continue proliferation after day seven, most likely due to the initial low adhesive force of the cells on these surfaces, thereby having cell detachment and emptying space for future cell growth and spreading. On day seven, cells on the PMMA and SU-8 surfaces showed an increase in MAP2k1 gene expression. Similarly, in a pilot study we conducted (data not shown), these two surfaces showed the highest increase in cell proliferation at day ten. These results indicate that cells grown on SU-8 and PMMA surfaces proliferate at a slower rate than cells growing on silicon and platinum. Cells grown on silicon and platinum substrates had a decreased MAP2k1 gene expression which further verifies full confluency by day seven *in vitro*.

A major hypothesis in current research implies that reactive astrocyte formation of the astroglial scar results in the chronic impediment of the electrodes and neurodegeneration(Frampton et al., 2010; McConnell et al., 2009). In order for this hypothesis to be validated, astrocytes need to increase reactivity with time, or at the very least maintain the same level of reactivity over the course of time. The results of this study found that the expression of GFAP decreased in astrocytes growing on all of the different material surfaces over time. In addition, the projected area of the cells' nuclei had decreased over time,

demonstrating that the area of the nucleus is directly proportional to the state of reactivity of the astrocyte. These results indicate that the astrocyte reaction to the materials was not a chronic, but rather an acute response.

5.5 Conclusions

The current study utilized a combination of techniques for characterizing the biocompatibility of cells *in vitro* on neural electrode materials. This information should be helpful in establishing sound guidelines of which neural implant materials should meet in order to be depicted biocompatible. This study has shown evidence of non-cytotoxicity of SU-8. We have confirmed the biocompatibility of PMMA with astrocytes. This data suggests the need of future investigations of both materials under *in vivo* conditions. We have shown astrocytes depict reactive characteristics when grown on platinum and silicon surfaces, thus rendering the need to find more biocompatible, conducting materials for neural electrode fabrication.

CHAPTER 6

6.1 Evaluation of Protein and Cellular Response to Nanopatterning

Numerous scientific techniques have been used for improving the cellular response to implanted neural electrodes. Studies have been performed on alterations in the device size, shape, material choice, and surface topography. Moreover, literature has shown (see Chapter 4 for more details) the effects surface topography modifications has on cellular behavior, more importantly, the effects nano-sized alterations have on protein adherence and cellular behavior. Depending on pattern size, proteins have been shown to adsorb at different rates, quantities, and even change their conformation due to the pattern. Studies have revealed cells alter their morphology, adhesion, migration, alignment, gene expression, and viability depending on the surface topography. This evidence lends support for our proposed work which examines the effect specific nanopatterning features will have on protein adsorption and astrocyte response. Preliminary data collected in this lab was utilized in determining the material and nanopattern feature dimensions used in this study (Ereifej et al., 2011; Salakhutdinov et al., 2008). Nanopatterned surfaces were fabricated with nano-imprint lithography on PMMA surfaces. The rate of protein adsorption, quantity of protein adsorption, cell alignment, morphology, adhesion, proliferation, viability and gene expression were compared between nanopatterned surfaces of different dimensions.

6.2 Methodology

6.2.1 Nanopattern Fabrication

Nanoimprint lithography (NIL), otherwise known as hot embossing, was utilized to create various nanopatterned surface. Specifically, the JenOptik HEX03 hot embossing system (Figure 20) (SSIM laboratory at Wayne State University) was used. Goodfellow UV-grade poly(methyl methacrylate) (PMMA) was the substrate. The processing temperature was 105-195°C and the applied controllable force is 300N – 3kN (Figure 21). Reflective holographic grated molds were purchased from Edmund Optics (Barrington, NJ) and used to make the patterned substrate with a period of 3600 grooves/mm, 1800 grooves/mm. A flat mirror mold was used for a controlled non-patterned surface. The embossed substrates were cut into 1cm^2 wafers. As a standard surface, we used polystyrene cover slips. All samples were cleaned with isopropanol, followed by 1×PBS and distilled water washes, and then sterilized under UV light for two hours.

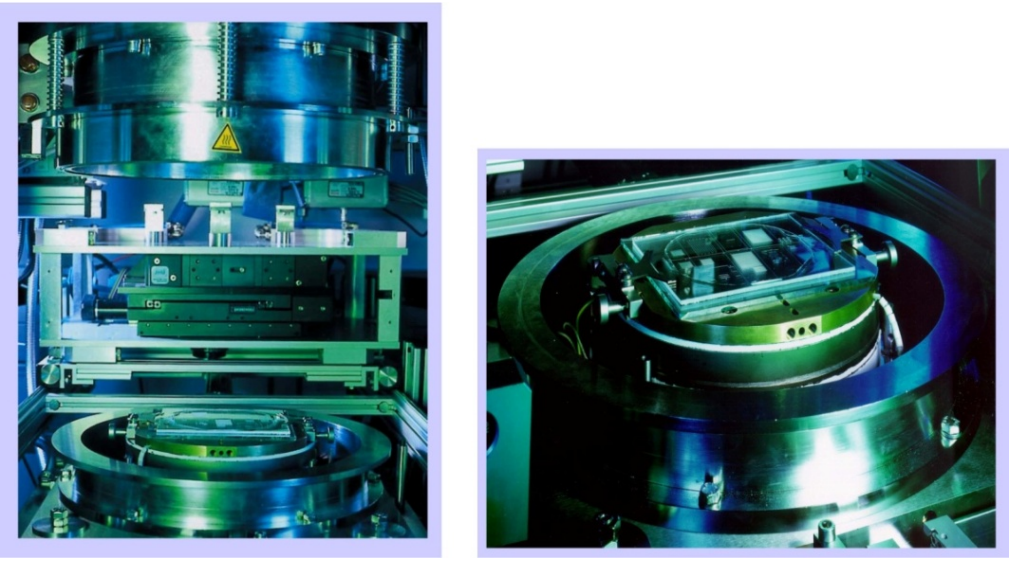

Figure 20. A) Nanoimprint lithography machine. B) Area in NIL machine in which the mask is placed.

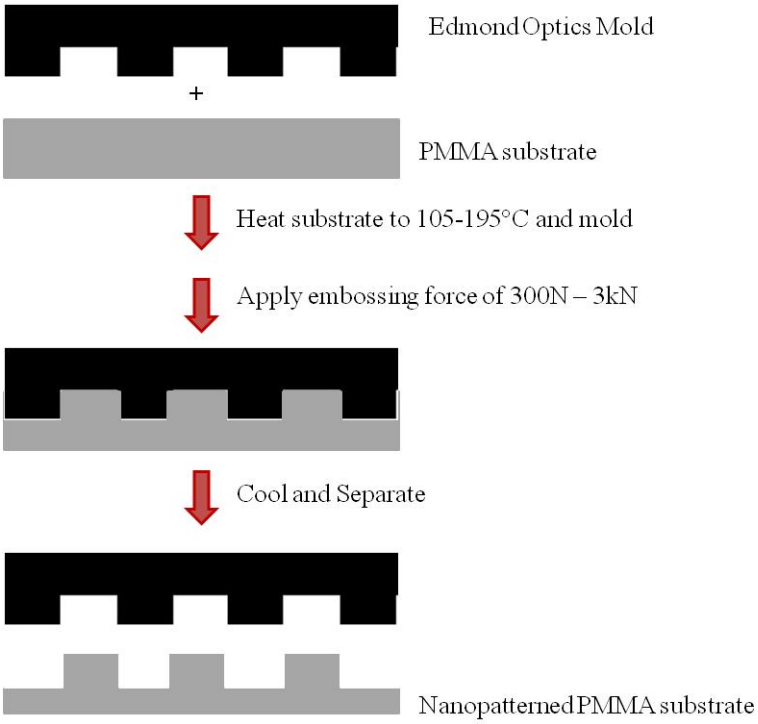

Figure 21. Schematic representation of material fabrication. Shown here is an example using the nanopatterned substrate; the same steps were used to make the non-patterned samples.

6.2.2 Atomic Force Microscopy

The dimensions of the nanopatterned PMMA substrates were characterized by Dimension 3100 AFM (VEECO) in the tapping mode in ambient air. The height, amplitude, and phase images were obtained using silicon tapping tips (nanoScience Instruments, VistruaProbes T300) with resonance frequency of 300 kHz and tip radius less than 10 nm. The scan rate was 1–3 Hz. Height images are plane-fit in the fast scan direction with no additional filtering operation. The dimensions of the nanopattern structure were determined using the sectional height analysis command (Nanoscope 5.30r3sr3) by manually measuring the lateral diameters and vertical heights of 3 - 5 different spots on each sample**.**

6.2.3 Scanning Electron Microscopy

Scanning electron microscopy (SEM) was utilized to image cells and brain tissue on the substrate surface. In particular, the Environmental SEM Quanta FEG 450 (FEI Company, Hillsboro, OR) was used at an operating high voltage of 10kV and pressure of 5.5 Torr. On day seven, samples were fixed in a 4% paraformaldehyde solution for 30 minutes at room temperature (RT). Following three rinses in 1×PBS, the samples were then washed in distilled water in order to remove salt crystals from the PBS.

6.2.4 Ellipsometry

In order to measure the rate of protein adsorption, the Beaglehole intruments NZ - Picometer Ellipsometer was used. This is a phase modulated ellipsometer that uses a HeNe laser at 633nm wavelength. The brewester's angle for PMMA was set at 56^{o}. After which, the samples were placed into a quartz cuvette and 1µg/ml of protein (fibronectin or collagen) was pipetted into the cuvette. The machine was set to run for three hours and collected data every ten seconds. The refractive index of the protein is required to measure thickness; however, thickness

was not measured in this study. Ellipticity depends on the refractive index of the ambiance of substrate, which in our case is the protein; it is proportional to thickness. Same ellipticity may correspond to different thickness depending on the ambiance of the substrate. This study conveyed the change along the y-axis over time in order to determine the arbitrary rate of protein adsorption on the nanopatterned and non-patterned substrates.

6.2.5 Protein Assay

The amount of protein adsorption was measured through the Micro BCA Protein Assay (Thermo Scientific, Waltham, MA). Wafers were incubated for two hours at room temperature with a 200µl droplet of either 10µg/ml of fibronectin or collagen. Thereafter, 150µl of the protein was collected and pipetted into a 96-well plate. As per manufacturer's protocol, 150µl of the working reaction was mixed with the protein in the 96-well plate on a shaker for 30 seconds. The standard curve was used to determine the protein concentrations. The standard curve was created by using serial dilutions of bovine serum albumin (BSA). The plate was covered and incubated at 37^{o}C for two hours, cooled to room temperature and then read at 562 nm on a microtiter plate reader**.**

6.2.6 Contact Angle Measurement

The water contact angle was determined from the shape of axisymmetric menisci of 5µl distilled water drops using a goniometer.

6.2.7 Cell Cultures

This study utilized C6 rat astrocytoma cell line (ATCC, Manassas, VA). The cells were maintained in a F-12K medium supplemented with 10% horse serum, 2.5% fetal bovine serum (FBS), and 1% antibiotics-antimycotic. The cells were kept in a humidified incubator with the following setting conditions: 90% humidity, 5% CO_2 and 37.8^{o}C. The media was changed twice

a week. Cells were detached using trypsin and then centrifuged at 1000rpm. The cells were then resuspended in culture media, stained with Trypan blue and counted using a hemocytometer. There were 5000 cells in 100µl droplet of culture media loaded onto each sample in a 24 well plate. Following three hours of incubation at 37^{o}C, 500µl of culture media was added to each well.

6.2.8 Proliferation Assay

The methylthiazolyldiphenyl tetrazolium bromide (MTT) colorimetric assay was employed to determine the number of cells and the rate at which they proliferated at days 1, 3, and 7 post seeding. At each time point, 0.5 mg/mL MTT reagent was added to the culture medium and reincubated for 5 hours in the dark at 37^{o}C until the yellow MTT was reduced to purple formazan crystals. The culture media was removed carefully, so as to not disturb the formazan crystals, and replaced by dimethyl sulfoxide (DMSO), which solubilized the formazan crystals and cells. Absorbances were read at 570nm and 650 nm in a microtiter plate reader. The optical densities were calculated by subtracting the 650nm reference wavelength from the 570nm absorbance reading. To measure the approximate number of cells on the given test days, a growth curve for C6 cells was also generated by performing a MTT assay on a graded series (range from 2,000 to 1,500,000 cells) of cells plated on polystyrene culture dishes.

6.2.9 Real Time PCR

Real time PCR was used to measure gene expression from the different samples relative to the control surface (polystyrene samples). The total RNA from the samples was extracted on days 3 and 7 post seeding with Trizol (Invitrogen, Carlsbad, CA) following the manufacturer's protocol. The RNA concentration and purity was determined using a spectrophotometer through UV absorbance at 260nm and 280nm. Reverse transcriptase using the oligo$(dT)_{20}$ primer

converted the mRNA to a cDNA template using a thermal cycler (Mastercycler Gradient, Eppendorf, Hauppauge, NY). For PCR analysis, we used cDNA equivalent to 40ng of total RNA. Specific primer pairs (Table 4) for proliferation, mitogen-activated protein kinase kinase 1 (MAP2K1), and astrocyte activation, glial fibrillary acidic protein (GFAP) were employed. As an internal control, we used the house-keeping gene glyceraldehyde-3-phosphate dehydrogenase (GAPDH). The PCR master mix included 1 x SYBR® Green (Applied Biosystems, Foster City, CA), and forward and reverse primers (0.4μM each). cDNA templates and master mix were read in a 96-well optical plate using a 7500 Fast Real-Time PCR System (Applied Biosystems, Foster City, CA). The following profile was used: 50°C for 2 min, 95°C for 10 min, and 40 cycles of 95°C for 15s and 60°C for 1 minute. Threshold cycle (Ct) values for each sample and primer pair were obtained and analyzed with the delta-delta (ΔΔ) Ct method(Livak and Schmittgen, 2001; Schmittgen and Livak, 2008) in order to calculate the fold change (R) in each target gene. The following equations were used:

$\Delta Ct = Ct_{sample} - Ct_{GAPDH}$

$\Delta\Delta Ct = \triangle Ct_{test\ surface} - \Delta Ct_{control\ surface}$

$R = 2^{-\Delta\Delta Ct}$

Table 4. Primer sequences for real-time PCR used in nanopatterned PMMA studies.

Cells	Category	Gene	Primer Sequence
C6 rat astrocytoma cells	Housekeeping gene	GAPDH	5'-TGGCCTTCCGTGTTCCTACC-3' (F)
			5'-AGCCCAGGATGCCCTTTAGTG-3' (R)
	Proliferation gene	MAP2K1	5'-TTCAAGGTCTCCCACAAGCCATCT-3' (F)
			5'-TTGATCCAAGGACCCACCATCCAT-3' (R)
	Activation gene	GFAP	5'-GTTGTGTTCAAGCAGCCTGG-3' (F)
			5'-CCAGTGAGTAAAGGTGACAG-3' (R)

6.2.10 Viability Test

In order visually observe the morphology and viability of the cells on the different surfaces; the Live/Dead® viability/cytotoxicity assay (Invitrogen, Carlsbad, CA) were used. Calcein AM (2µm in phenol red free DMEM) was used to stain the live cells a green fluorescent color that can be seen using an emission filter (FITC) of ~488. Ethidium homodimer (EthD-1) (4µm in phenol red free DMEM) was used to stain the dead cells a red fluorescence, which can be seen using an emission filter at ~528. The samples were incubated in the Live/Dead stain for 20-30 minutes inside the incubator (37^{o}C). Thereafter, the samples were mounted onto slides using Prolong Gold antifade mounting gel (Invitrogen, Carlsbad, CA) and viewed under a Zeiss Axio Observer Inverted Microscope (Carl Zeiss Inc). Images for each sample were taken in the same location with both the red and green filters.

6.2.11 Cell Nuclei and Cytoskeleton Staining/ Cell Adhesion

Fluorescence staining was utilized to image the cells' cytoskeleton along with the nucleus. The cells were washed in phosphate buffered saline (1×PBS) and fixed in 4% paraformaldehyde for 20 minutes. The cells were washed in PBS, and then permeablized by incubation for 25 minutes in 1X PBS containing 0.25% Triton X-100. The cells washed, blocked with 1% fetal bovine serum (FBS) for 25 minutes and washed again with 1X PBS. Cells were stained with Rhodamine Phalloidin in 1×PBS (Invitrogen, Carlsbad, CA) for 20 minutes at room temperature in the dark. Double staining of the nucleus was done with 2µg/mL of 4',6-diamidino-2-phenylindole (DAPI; Sigma-Aldrich, St. Louis, MO) for 20 minutes at room temperature in the dark. Thereafter, the samples were mounted onto slides using Prolong Gold antifade mounting gel (Invitrogen, Carlsbad, CA) and viewed under a Zeiss Axio Observer

Inverted Microscope (Carl Zeiss Inc). Images for each sample were taken in the same location with both the red and DAPI filters.

6.2.12 Image Analysis

Image J software was used to quantify the number of live cells versus the dead cells, and calculate the number of adhered cells. Each image was first converted to an 8-bit grayscale from which a threshold binary image was created. An average area of stained live and dead cells was measured and used to set a global scale of a particle size. The average area of stained dead cell was 50μm^2 and a stained live cell was 80μm^2. Thereafter, the cells were counted using the analyze particles function. The following formula was used to calculate the percentage of live and dead cells:

$$\% \text{ of live cells} = \frac{\#\text{ of live cells}}{\text{sum of total cells (live + dead)}} * 100$$

In order to calculate the number of adhered cells, total DAPI stained area in an image (each image was 217μm × 162μm) was measured, then divided by the average measured cell nucleus size (50μm^2).

6.2.13 Statistical Analysis

All of the data are presented as a mean ± standard error of the mean. Experiments were performed in triplicates and repeated three independent times. PASW software (version 18.0) was utilized for statistical analysis. A nonparametric statistical analysis was used to test for statistically significant differences between the different material groups over all time points for the RTPCR, MTT assay, BCA assay, viability and cell adhesion studies. Parametric statistical methods could not be completed due to insufficient power from a small sample size, mean values

were either not normally distributed or the variances of the data were not heterogeneous. The exact tests were conducted in order to be able to make reliable inferences by computing exact p values for a very wide class of hypothesis tests, including one-, two-, and K sample tests, tests for unordered and ordered categorical data, and tests for measures of association.

6.3 Results

6.3.1 Nanopattern Fabrication

Figure 22 depicts the successful fabrication of patterns with periods of either 3600 grooves/mm or 1800 grooves/mm, which translates to a 277nm width versus a 555nm width respectively, and both patterns had a depth of 200nm.

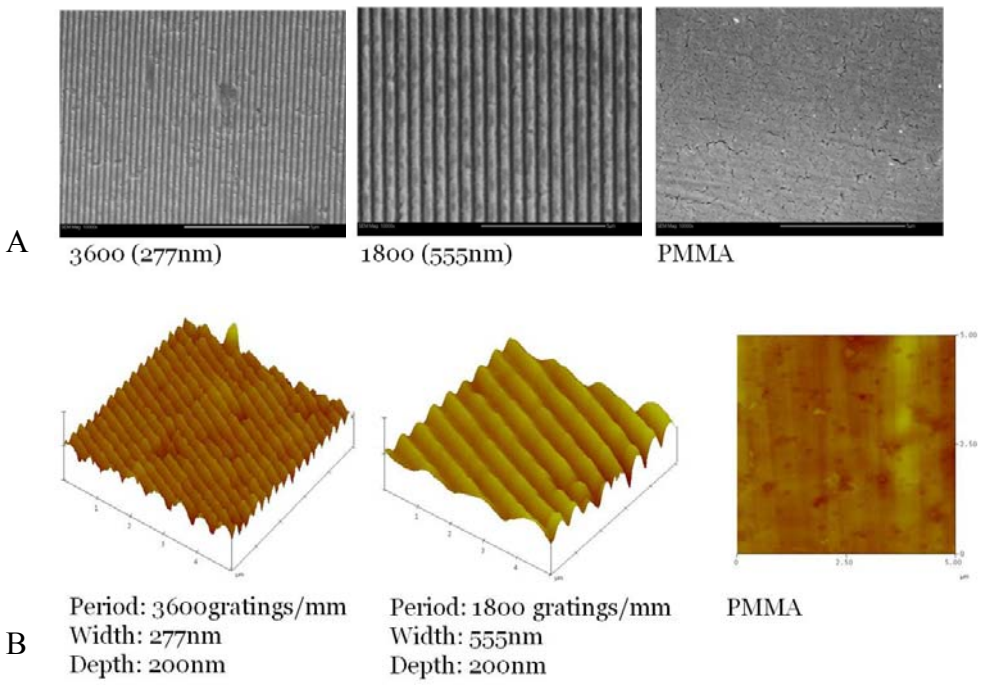

Figure 22. Images of the two nanopattern substrates and flat PMMA substrate (prior to hot embossing). A) Scanning Electron Microscopy B) Atomic Force Microscopy

6.3.2 Protein Assay

Results from the protein assay demonstrated at least 9µg/ml of collagen was adsorbed onto all surfaces, while 7µg/ml of fibronectin adsorbed onto the surfaces (Figure 23). There was significantly more ($p<0.01$) collagen adsorption on all surfaces compared to fibronectin adsorption. Moreover, there was significantly less ($p<0.05$) fibronectin adsorption on the 3600 patterned surface compared to the 1800 patterned, non-patterned, and PMMA surfaces. There was significantly elevated levels ($p<0.05$) of collagen adsorption on the PMMA surface compared to the 1800 patterned surface.

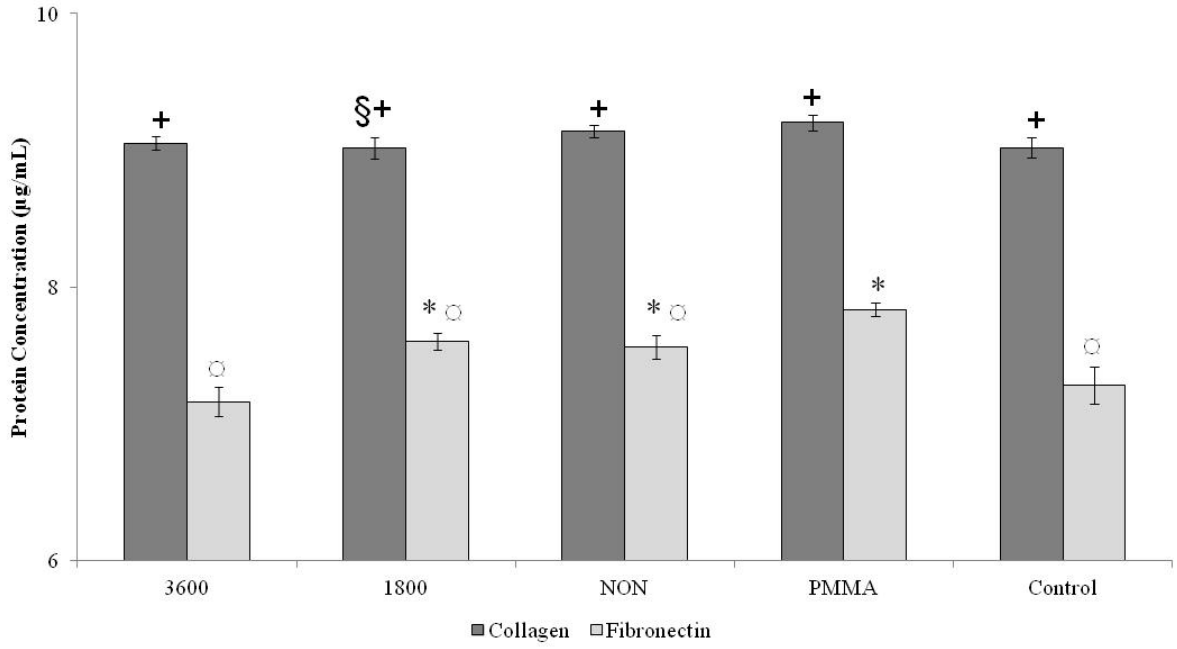

Figure 23. Micro BCA protein adsorption assay results. *$p<0.05$ fibronectin data compared to 3600, ¤$p<0.05$ fibronectin data compared to PMMA, §$p<0.05$ collagen data compared to PMMA, +$p<0.01$ fibronectin data on all surfaces compared to collagen data on all surfaces.

6.3.3 Ellipsometry

Ellipsometry results (Figure 24) indicated that the rate of collagen adsorption was 10-fold faster as compared to the fibronectin adsorption. Results demonstrated that both of the nanopatterned substrates had faster rates of collagen and fibronectin adsorption compared to the non-pattern surfaces. Additionally, the 3600 pattern substrates had the highest rate of both fibronectin and collagen adsorption compared to 1800 pattern and non-pattern substrates.

A

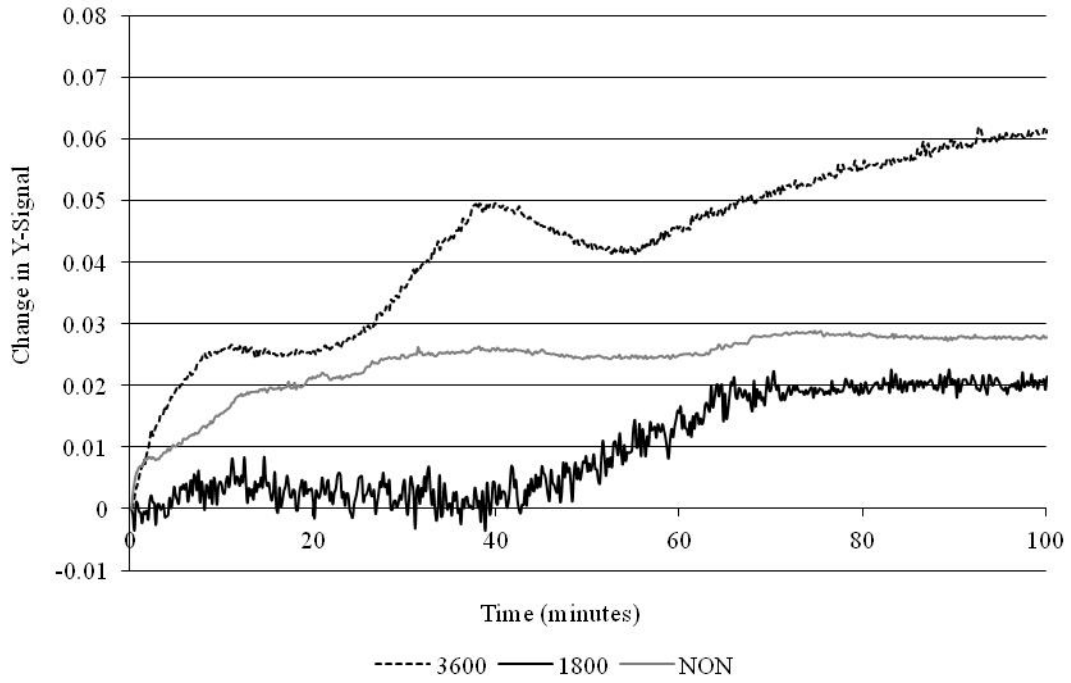

B

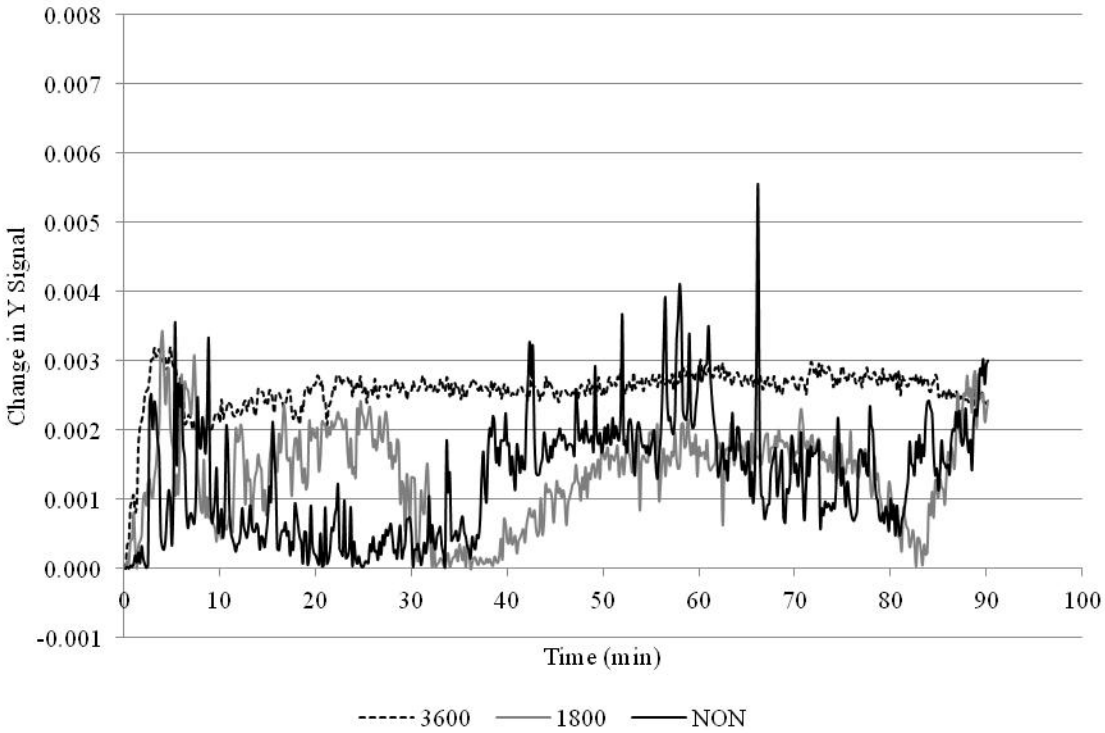

Figure 24. Ellipsometry results depicting the rate of (A) collagen (B) fibronectin adsorption on the two different sized patterns and non-patterned surface.

6.3.4 Contact Angle

Contact angle measurements revealed that the adsorption of fibronectin and collagen on the material substrates made the surfaces more hydrophilic (Table 5).

Table 5. Contact angle measurements, shown and mean ± standard error.

	No Protein	Collagen	Fibronectin
3600	76 ± 2	66 ± 1	65 ± 3
1800	62 ± 1	63 ± 1	62 ± 3
NON	74 ± 2	65 ± 1	76 ± 2
PMMA	66 ± 3	57 ± 2	56 ± 1
Control	68 ± 1	58 ± 2	57 ± 1

6.3.5 Cell Alignment

Phase contrast images taken at days one, three and seven, showed that over time the cells began to orient themselves in one direction (Figure 25). Cells appeared to have a unique temporal response dependent on the pattern surface. Cells grown on the 1800 pattern began to align in one direction after only one day in culture. In contrast, cells cultured on the 3600 pattern did not fully orient in one direction until three days in culture. As can be seen from the Figure 25, cells grown on the non-patterned surface were randomly oriented along the surface at all time points.

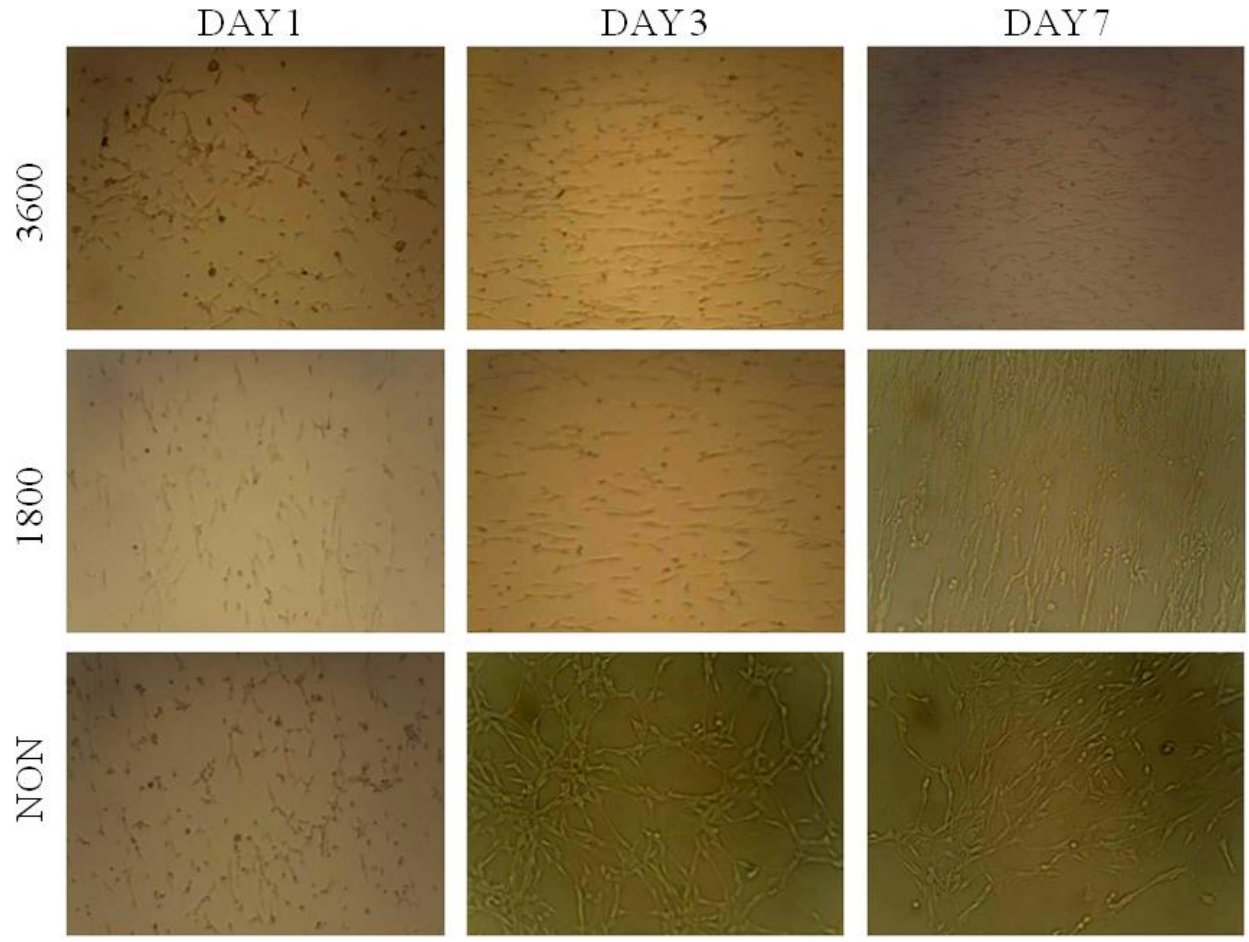

Figure 25. Phase contrast images of astrocytes aligned on patterned and nonpatterned PMMA surfaces (20X).

6.3.6 SEM

SEM images (Figure 26) reveal that by day three, cells on both of the patterned surfaces grew along the nanopattern. Moreover, the cells growing on the nanopattern surfaces had an elongated shape compared to the typical astrocyte star-like shape seen on the non-pattern substrate. Cells followed the pattern whether in low densities or in complete confluence.

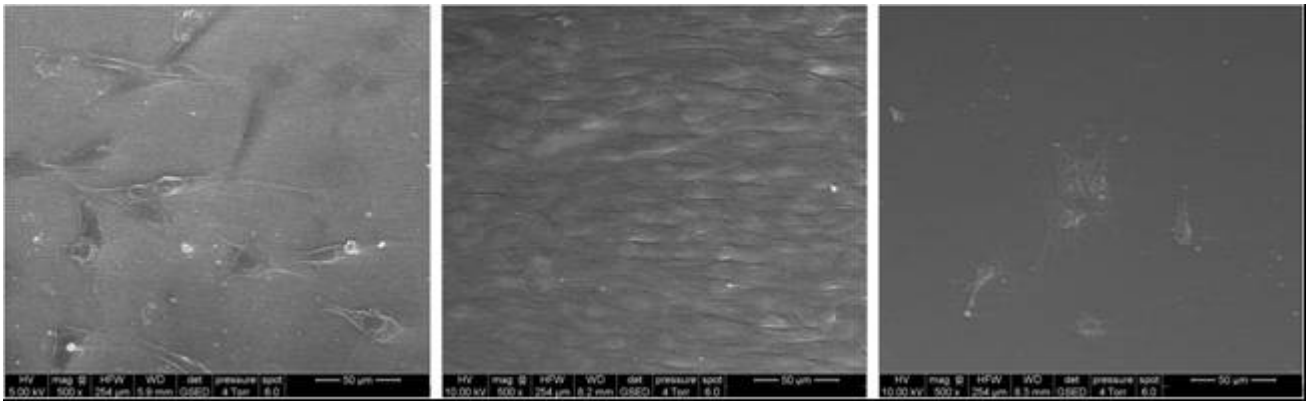

Figure 26. SEM images of astrocytes growing on the hot embossed PMMA substrates on day three in culture (from left to right), 3600 nanopattern, 1800 nanopattern, and non-pattern.

6.3.7 Viability Assay

Results of the viability assay revealed that all of the substrates tested had at least 89% viability at both time points. Cells cultured on the 1800 nanopattern substrates had significantly higher ($p<0.05$) viability on day three compared to cells cultured on 3600 nanopattern, PMMA and control substrates (Figure 27). Cells grown on the 3600 nanopattern substrates had significantly lower ($p<0.05$) viability on day three compared to cells grown on non-nanopattern and control substrates. Cells grown on the control and non-nanopattern substrates had significantly higher ($p<0.05$) viability on day three compared to those grown on PMMA. However, by day seven, cells cultured on PMMA had significantly higher ($p<0.05$) viability compared to 1800 nanopattern, 3600 nanopattern, and control substrates. Cells grown on the non-nanopattern substrates had significantly higher ($p<0.05$) viability compared to the 3600 nanopattern on day seven.

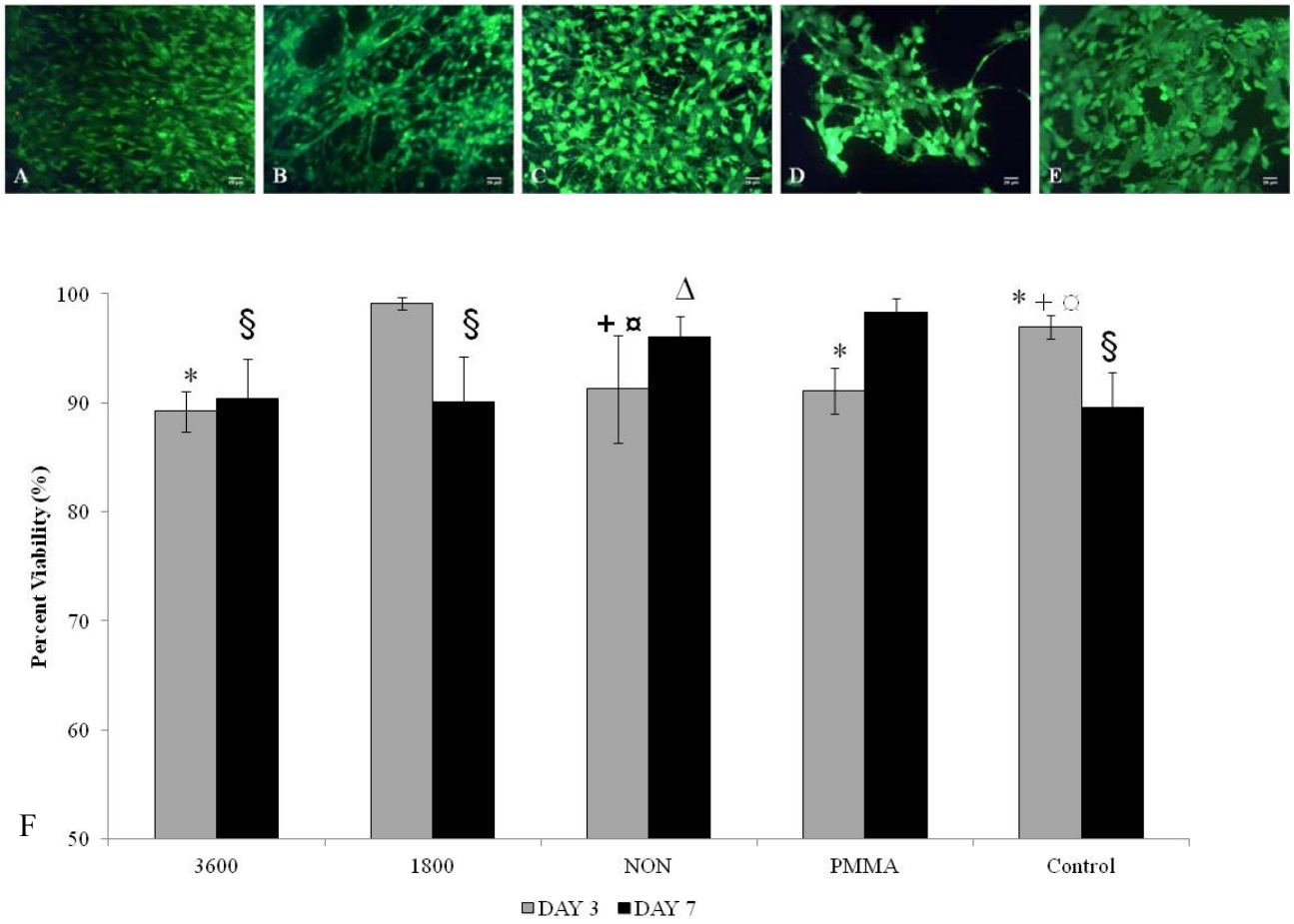

Figure 27. Live/Dead images taken on day seven a) 3600 nanopatterned b) 1800 nanopatterned c) non-nanopatterned d) PMMA e) control polystyrene f) viability results of cells on materials surface on days 3 and 7 days *in vitro* *p<0.05 data on day three compared to 1800, +p<0.05 data on day three compared to 3600, ¤p<0.05 data on day three compared to PMMA §p<0.05 data on day seven compared to PMMA, Δp<0.05 data on day seven compared to 3600

6.3.8 MTT Proliferation Assay

Results of the MTT proliferation assay demonstrated a significant increase (p<0.05) in cell proliferation between day one and day three with 1800 nanopattern, 3600 nanopattern, and non-nanopattern substrates (Figure 28). There was a significant increase (p<0.05) in proliferation between day three and seven with 1800 nanopattern, 3600 nanopattern, non-nanopattern and control substrates (Figure 28). At day one, all nanopatterned substrates had significantly fewer

($p<0.05$) cells compared to the control, yet significantly more ($p<0.05$) cells compared to PMMA (Figure 28). Results on day three showed similar findings, all substrates had significantly fewer ($p<0.05$) cells compared to the control and significantly more cells compared to PMMA (Figure 29). The 3600 nanopattern and non-nanopattern substrates had significantly fewer ($p<0.05$) cells on day three compared to the 1800 pattern substrate (Figure 29). Day seven results showed all test substrates had significantly higher ($p<0.05$) number of cells compared to PMMA (Figure 30). However, compared to the control, only 1800 pattern, non-pattern, and PMMA had significantly more cells on day seven (Figure 30). Moreover, compared to the 3600 pattern, the 1800 pattern and non-pattern had significantly fewer ($p<0.05$) cells on day seven (Figure 30). Non-nanopattern substrates had significantly fewer ($p<0.05$) cells compared to 1800 pattern (Figure 30).

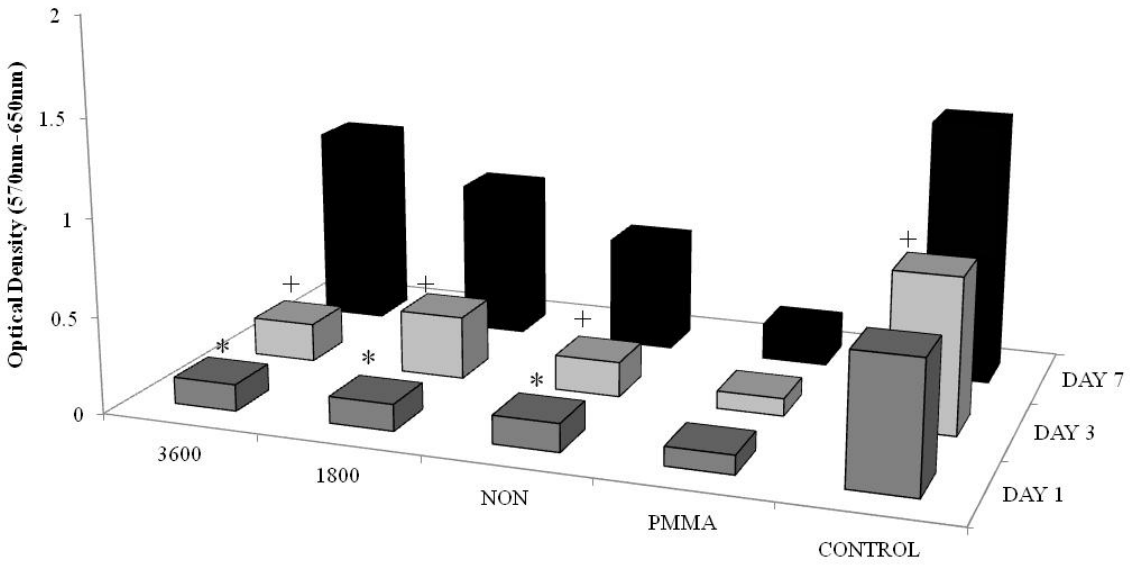

Figure 28. MTT proliferation assay. *$p<0.05$ day one data compared to day three data, +$p<0.05$ day three data compared to day seven data

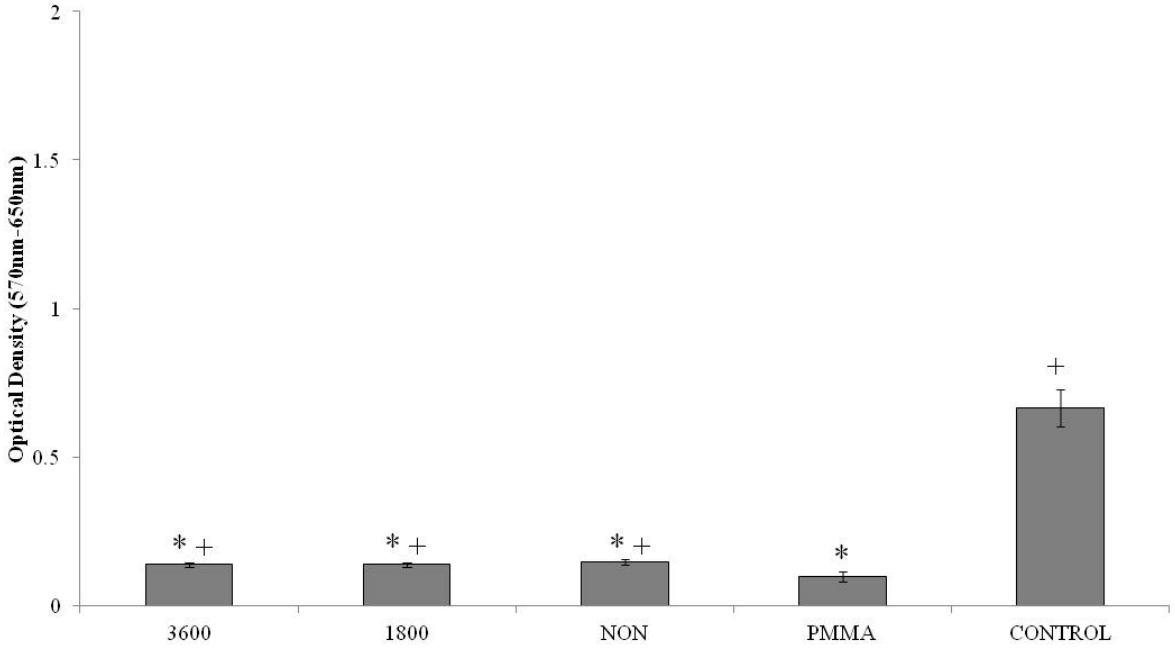

Figure 29. MTT proliferation assay. *p<0.05 data compared to control +p<0.05, data compared to PMMA

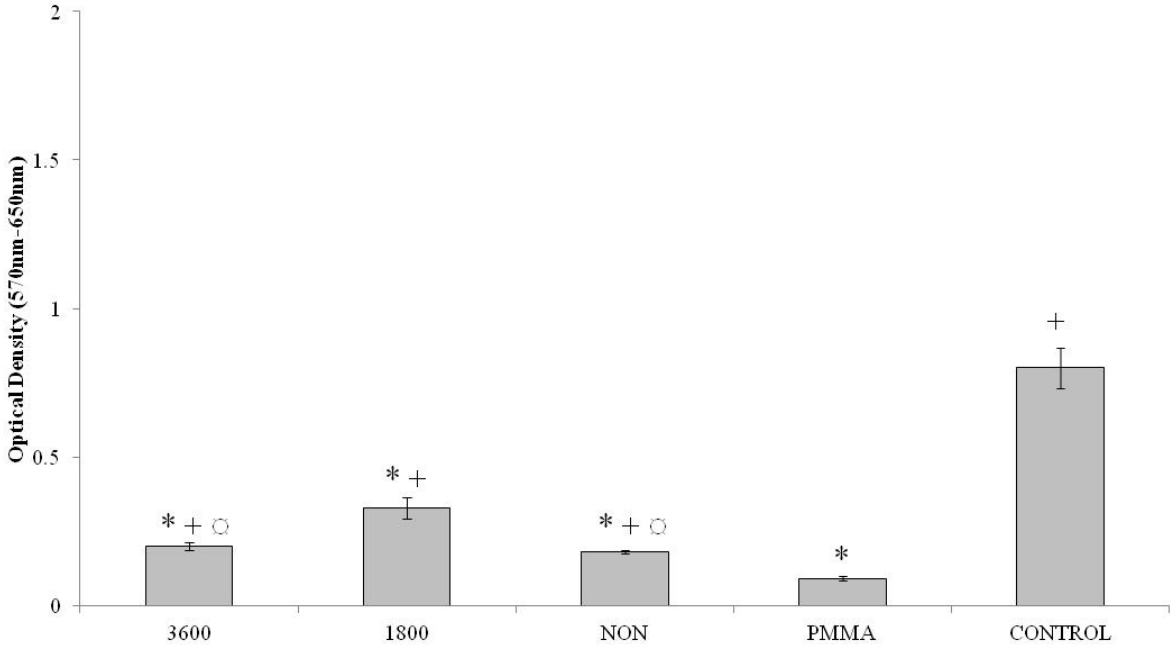

Figure 30. MTT proliferation assay. *p<0.05 data compared to control +p<0.05, data compared to PMMA, ¤p<0.05 data compared to 1800 pattern

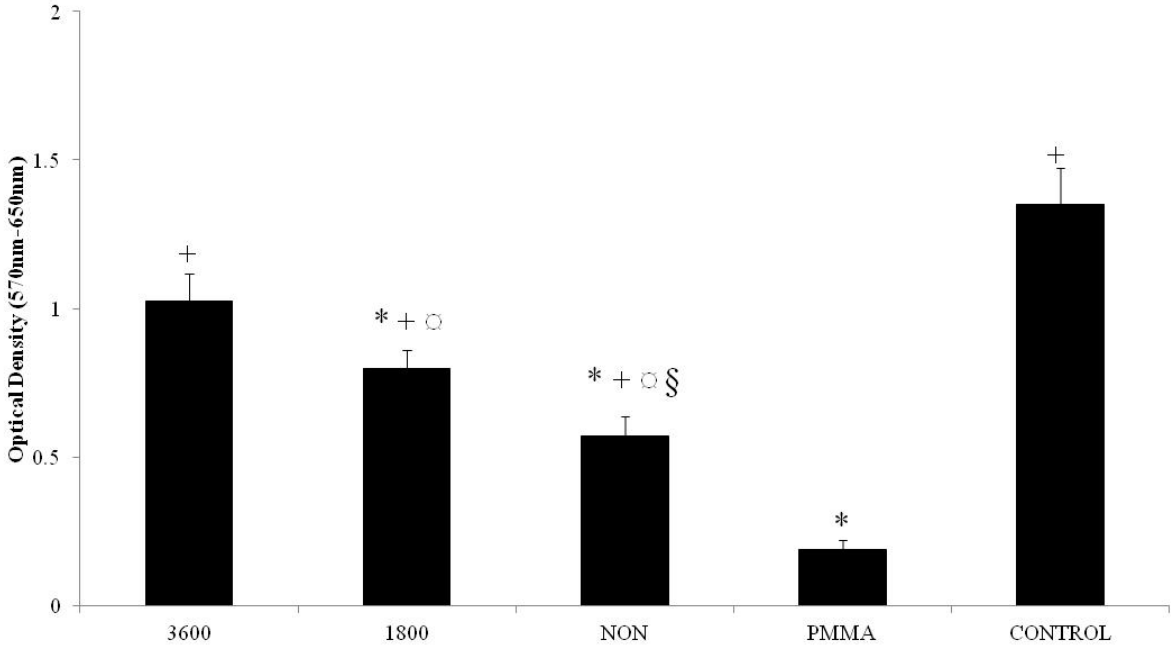

Figure 31. MTT proliferation assay. *p<0.05 data compared to control +p<0.05, data compared to PMMA, ¤p<0.05 data compared to 3600 pattern, §p<0.05 data compared to 1800 pattern

6.3.9 Relative Gene Expression

Results of GFAP relative gene expression on 3600 nanppattern were significantly lower ($p<0.05$) on day seven compared to 3600 nanopattern on day three and control on day seven. It is important to note, that GFAP relative gene expression on 3600 nanopattern was lower on day seven compared to all substrates (Figure 32). Moreover, GFAP relative gene expression was higher on the non-nanopattern substrates compared to all other substrates on both days. MAP2k1 relative gene expression of 3600 pattern on day seven was significantly lower ($p<0.05$) compared to control. Result of MAP2k1 relative gene expression show PMMA had higher levels compared to all other substrates on day three (Figure 33).

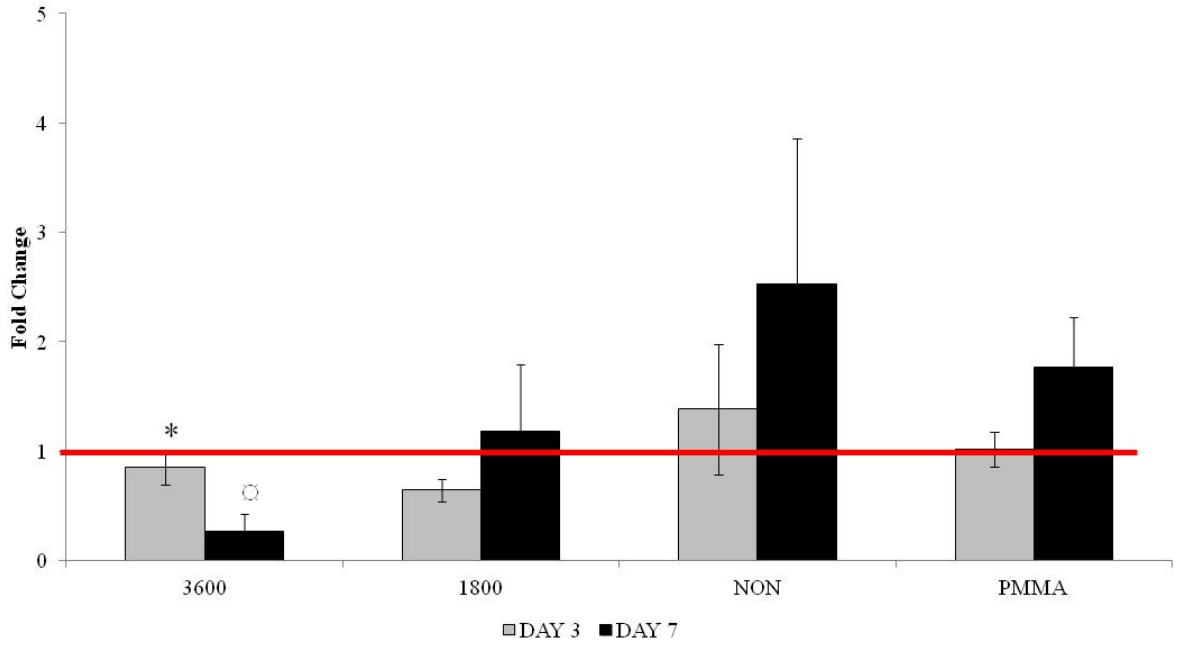

Figure 32. RTPCR GFAP relative gene expression. The control is represented as the red line. *p<0.05 data compared to 3600 on day seven, ¤p<0.05 data compared to control at day seven

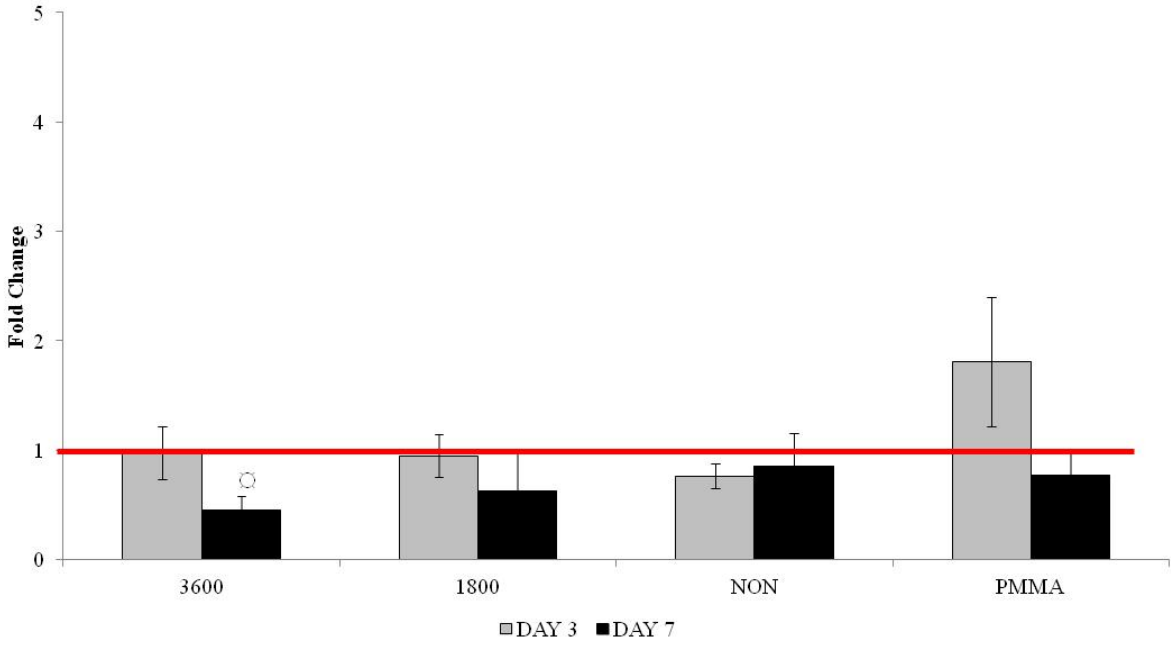

Figure 33. RTPCR MAP2k1 relative gene expression. The control is represented as the red line. ¤p<0.05 data compared to control at day seven

6.3.10 Cell Nuclei and Cytoskeleton Staining/ Cell Adhesion

Cell nuclei stained with DAPI were used to measure the number of adhered cells after one day in culture in order to quantify cell adhesion characteritics. Cells grown directly on the substrates, without any protein coating had significantly fewer ($p<0.05$) cells adhered across all substrate types compared to cells cultured on collagen or fibronectin coated substrates (Figure 34). There were significantly more ($p<0.05$) cells adhered on PMMA coated with fibronectin compared to PMMA coated with collagen (Figure 34). To the contrary, there were significantly fewer ($p<0.05$) cells adhered on 1800 patterned substrate coated with fibronectin compared to 1800 patterned substrate coated with collagen (Figure 34).

Compared to uncoated 1800 patterned substrate, there were significantly fewer ($p<0.05$) cells adhered on the 3600 patterned, PMMA and control substrates not coated with protein (Figure 35). Similarly, compared to the non-patterned uncoated substrate, there were significantly fewer ($p<0.05$) cells adhered on the uncoated 3600 patterned, uncoated 1800 patterned, PMMA and control substrates (Figure 35). There were significantly fewer ($p<0.05$) cells adhered on the uncoated 3600 patterned and uncoated control surface compared to PMMA (Figure 35).

There were significantly fewer ($p<0.05$) cells adhered on collagen coated 3600 pattern, 1800 pattern, non-pattern, and PMMA compared to the control (Figure 36). Compared to the collagen coated non-pattern substrates, there were significantly fewer ($p<0.05$) cells adhered on the 3600 pattern and PMMA substrates (Figure 36).

Compared to both fibronectin coated 3600 pattern and 1800 pattern, there were significantly more ($p<0.05$) cells adhered on the fibronectin coated non-pattern, PMMA, and control substrates (Figure 37).

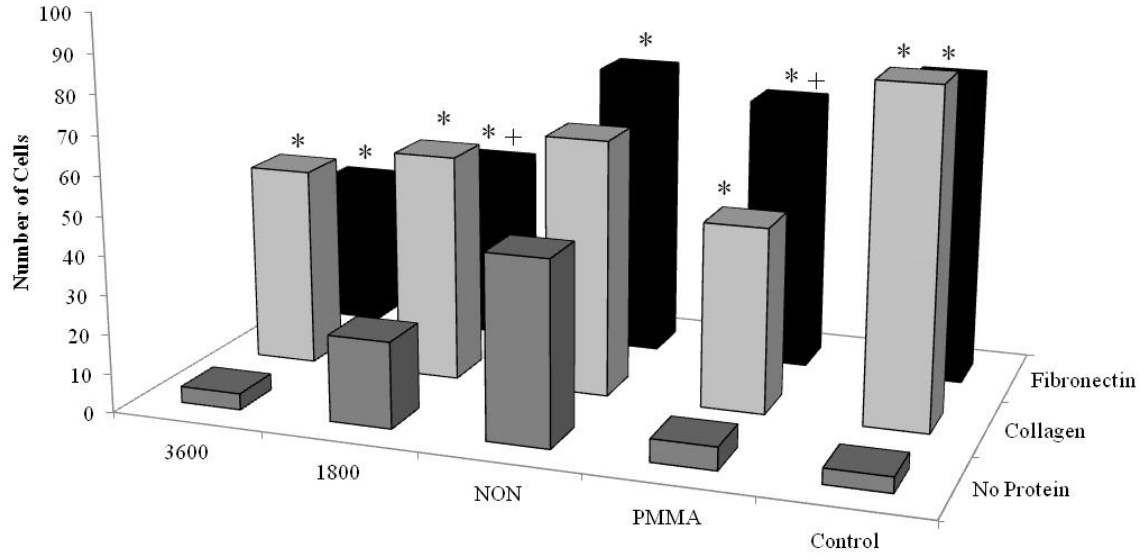

Figure 34. Number of cells adhered on substrates coated with either 10µg/ml fibronectin or 10µg/ml collagen or no protein at day one in culture. *p<0.05 data compared to no protein, +p<0.05 data compared to collagen

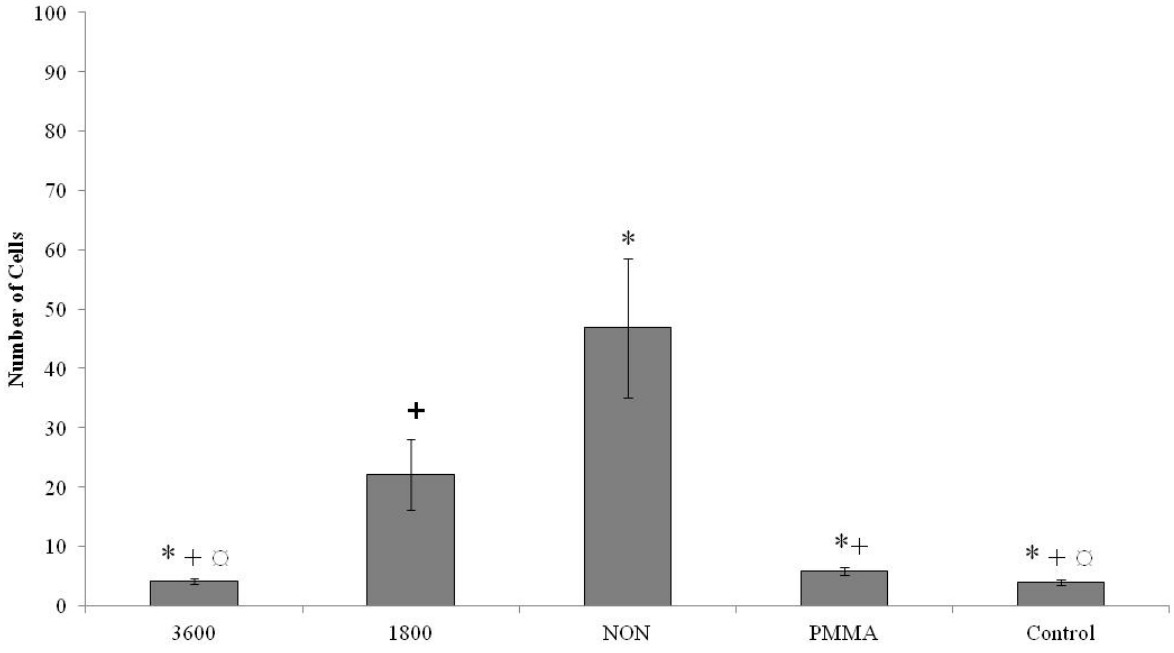

Figure 35. Number of cells adhered on substrates not coated with proteins at day one in culture. *p<0.05 data compared to 1800, +p<0.05 compared to NON, ¤p<0.05 compared to PMMA

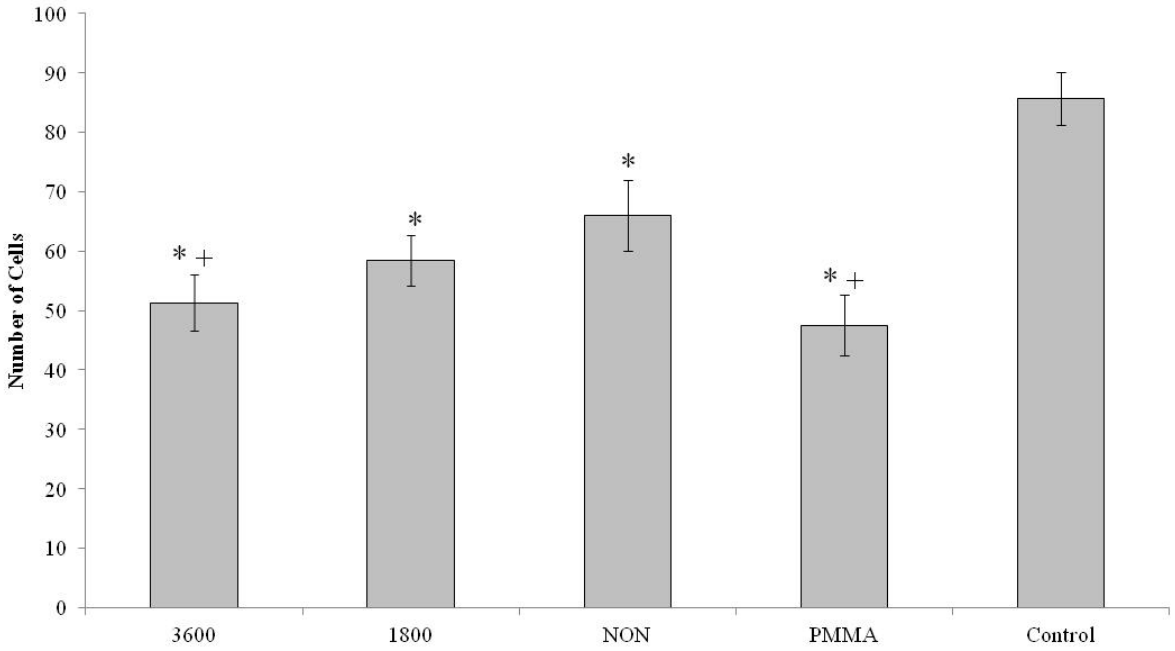

Figure 36. Number of cells adhered on substrates coated with 10µg/ml collagen at day one in culture. *p<0.05 data compared to control, +p<0.05 data compared to NON

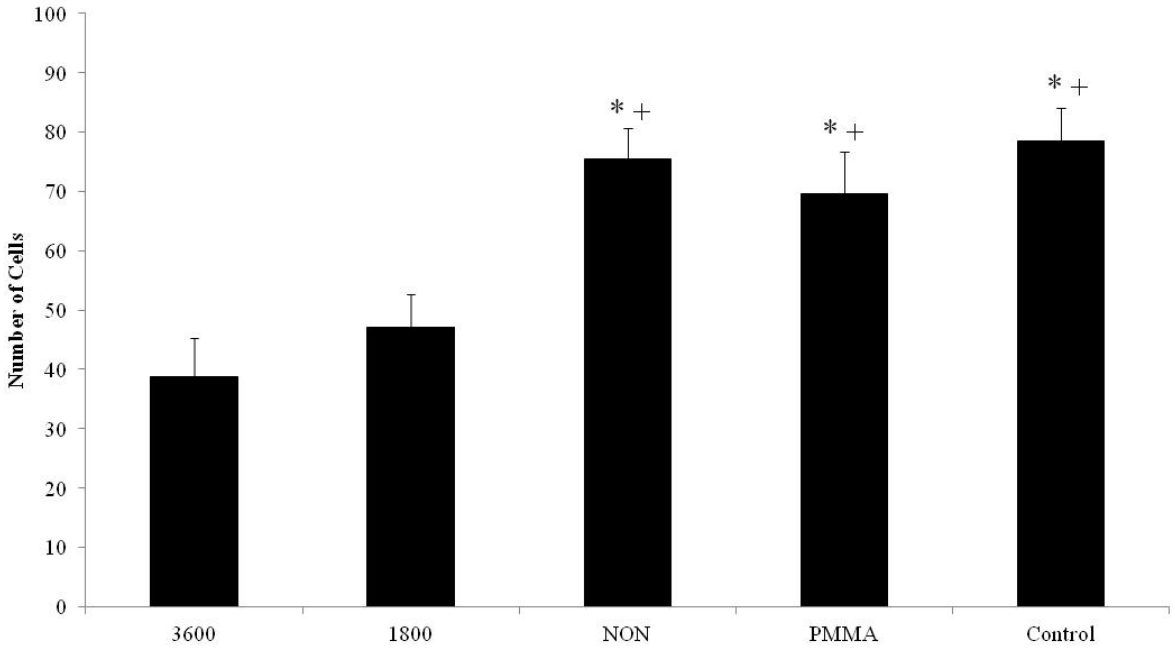

Figure 37. Number of cells adhered on substrates coated with 10µg/ml fibronectin at day one in culture. *p<0.05 data compared to 3600, +p<0.05 data compared to 1800

Results from the cell nuclei and cytoskeleton staining visually showed fewer numbers of cells on the substrates uncoated compared to the fibronectin and collagen-coated substrates (Figure 38). Moreover, these images revealed the cell morphology on the patterned substrates to be elongated compared to the star like morphology of the cells on the non-patterned, PMMA, and control substrates (Figure 38). Cells on the 1800 patterned substrate had elongated morphology on both of the protein coated surfaces and the uncoated surfaces. However, cells on the 3600 pattern substrate had a more defiant elongated morphology on both of the protein coated surfaces, and more of a star like morphology on the surface not coated with any proteins (Figure 38).

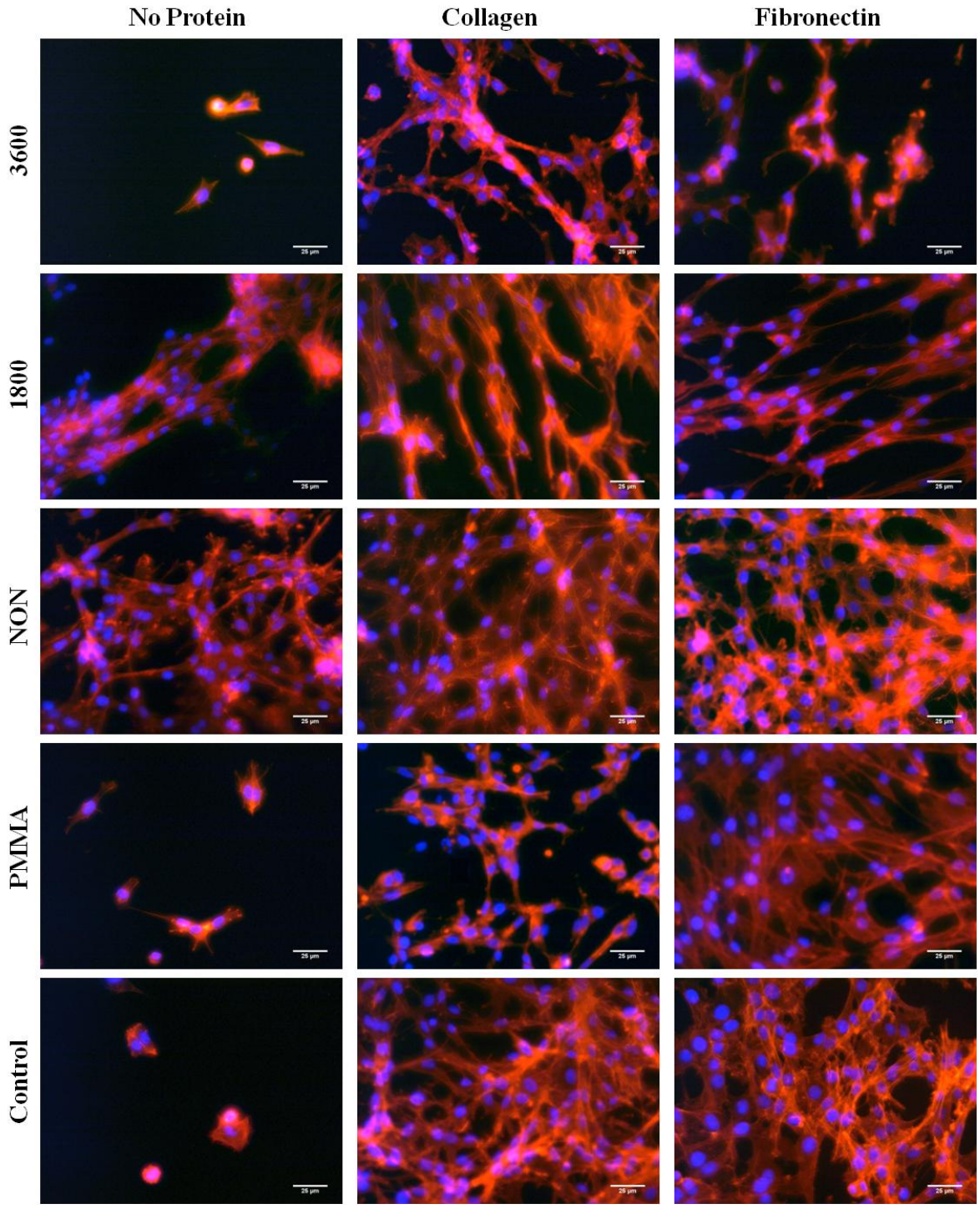

Figure 38. Rhodamine phlalloidin cytoskeleton stain double stained with DAPI for cell nucleus on day one (40X) of cells on 3600 patterned, 1800 patterned, non-patterned, PMMA, and control surfaces coated with either 10µg/ml collagen, 10µg/ml fibronectin or no protein

6.4 Discussion

Studies have shown that in a healthy adult brain, commonly found ECM proteins, such as fibronectin and collagen are scarce beneath the blood brain barrier and choroid plexus (Tate et al., 2007; Zimmermann and Dours-Zimmermann, 2008). When brain tissue damage occurs, (ie during neural electrode implantation), the levels of fibronectin is found to be increased, most likely entering through the injured blood brain barrier (Tate et al., 2007). The binding of fibronectin to the glial cell receptor (RGD peptide) has been shown to elevate their adhesion, migration, proliferation and production of cytokines (Hermanns et al., 2006; Mayeed et al., 2009; Tate et al., 2007; Thanawala et al., 2007). This increase in glial cell number is paralleled with an increase in their reactivity, therefore resulting in glial scar formation (Hermanns et al., 2006; Mian et al., 2007; Tate et al., 2007). As such, one of the goals of an optimal neural electrode biomaterial includes a reduced amount of glial activation which is linked to the increased fibronectin adsorption. This study showed the rate of fibronectin and collagen adsorption was higher on both of the nanopatterned surfaces compared to the non-patterned surface, although the amount of adsorbed protein was not always greater. In fact, there was significantly less fibronectin adsorption on the 3600 pattern compared to the 1800 pattern, non-pattern and PMMA. These results suggest that although the protein is adsorbing faster on the nanopattern surfaces, the nanopattern features on the 3600 pattern substrate may inhibit the amount of protein adsorbed.

Protein adsorption facilitates the cellular interaction with the substrate surface. The number and strength of cells adhered to a substrate is inherently affected by the level of protein adsorption (Alaerts et al., 2001; Dupont-Gillain et al., 2004; Ni et al., 2009; Salakhutdinov et al., 2008). Surface topography has been shown to either directly influence the cell response, or

indirectly effect the cell responses through the affects they have on the adsorption of proteins (Kamath et al., 2008; Kriparamanan et al., 2006; Tang et al., 1998; Thevenot et al., 2008). Cell adhesion results comparing substrates coated with fibronectin, collagen or no protein revealed that on all protein coated substrates, there was significantly more cell adhesion on both of the protein coated substrates compared to the substrates without any protein coating. The results demonstrate that the adsorption of both fibronectin and collagen decreased the contact angle of the substrates, therefore making them more hydrophilic, which is consequently desirable for cell attachment. Furthermore, it was found that there were significantly fewer number of cells adhered on both of the nanopatterned surfaces coated with fibronectin compared to the non-patterend, PMMA and the control. In fact, the fibronectin coated 3600 pattern substrate had the least number of cells compared to all other substrates. Similarly, Achyuta et al found that a decrease in fibronectin adsorption on the material surface resulted in a decrease in microglia attachment to that material because microglia adhesion on synthetic materials is known to be mediated by fibronectin (Achyuta et al., 2010). Overall, the amount of collagen adsorption did not differ significantly between the patterned and non-patterned substrates. However, the amount of cell adhesion on the collagen coated 3600 pattern was significantly less than the non-patterned substrate. The decrease of cell adhesion on both the fibronectin and collagen coated 3600 pattern and 1800 pattern, compared to the non-pattern and control substrates, may be due to conformational changes occurring in the proteins as they adhere to the patterned surface. Keller et al observed ultrahigh molecular weight polyethylene (UHMWPE) surface nanotopography alters the protein orientation and partially aligns single human plasma fibrinogen molecules (Keller et al., 2011). Tang et al have done numerous studies analyzing the cell response to various coating of functional groups on material surfaces (Kamath et al., 2008; Tang et al., 1998;

Thevenot et al., 2008). They found subsequent cellular responses were partially mediated by the surface chemistries of the materials due to the functional group coatings (Kamath et al., 2008; Tang et al., 1998; Thevenot et al., 2008).

Activated astrocytes are characterized by hypertrophy, hyperplasia, upregulation of GFAP, increased formation of filaments, irregularly shaped nuclei (Buffo et al., 2010; Gervasi et al., 2008; Laird et al., 2008; Polikov et al., 2006; Polikov et al., 2005). Nanotopography has been shown to affect the cells' adhesion, morphology, alignment, proliferation, gene expression profiles and even prevent biofouling and contamination on the material's surface (Kriparamanan et al., 2006). This was evident in the presented study. Relative gene expression of GFAP was the lowest on both patterned substrates compared to the non-patterned, PMMA and control substrates. In fact, the 3600 pattern substrate had a decrease in GFAP over time, and had the lowest GFAP gene expression on day seven compared to all materials. These results indicate that the nanopatterned PMMA substrates inhibit GFAP expression, with the 3600 pattern having the largest effect. The MAP2k1 relative gene expression decreased over time with both of the pattern substrates; again have the lowest levels with the 3600 pattern by day seven. These results imply that cells grown on the 3600 pattern are less hyperplasic within days indicating less astrocyte reactivity. O'Keefe et al did a study on the effects of microgrooves on fibroblast gene expression (O'Keefe et al., 2001). They found there were many initial gene changes and also down-regulation of gene response with time (O'Keefe et al., 2001). This was thought to happen due to the deformation in the cell and nucleus morphology (O'Keefe et al., 2001).

Cell alignment generally means the polarization and elongation of the cells in the direction of the nanogrooves. This is thought to be due to the rearrangements of the cytoskeleton

induced by the surface. This study demonstrated that nanoscale patterning alters cell attachment and organization on surface. By day one in culture cells on the pattern surfaces began to orient and align themselves along the nanopattern. Curtis et al observed that when fibroblasts were seeded onto a nanostructured surface, the first event which took place was the cytoskeleton arrangement (Curtis, 2005; Curtis et al., 2004; Das et al., 2008; Fok-Seang et al., 1998). Within the first five minutes post seeding, the actin aggregation occurred then within 20 minutes the microtubules aligned (Curtis, 2005; Curtis et al., 2004; Das et al., 2008; Fok-Seang et al., 1998). Furthermore, the differences found in gene expression between the nanopatterned and non-patterned surfaces may be due to the rearrangements of the cytoskeleton occurring from adhering and aligning along the nanopatterned surface. The transductions of mechanical forces cause the changes in gene expression. Studies have shown mechanical forces directly correlate with gene expression and protein production (Asparuhova et al., 2009; Avvisato et al., 2007; Sarasa-Renedo and Chiquet, 2005). The mechanical forces occurring *in vivo* are thought to cause shifting in the ECM, therefore stimulating the cells to establish new contact with the ECM (Asparuhova et al., 2009; Chiquet et al., 2003; Sarasa-Renedo and Chiquet, 2005). The physical stretching of the cell is then thought to expose previously hidden sites thereby resulting in altered responses (Asparuhova et al., 2009; Chiquet et al., 2003; Sarasa-Renedo and Chiquet, 2005).

Distinctive results were found comparing the protein and cell response to the 3600 pattern versus the 1800 pattern. The 3600 pattern had less fibronectin and collagen adsorption, but at a higher rate of adsorption compared to the 1800 pattern. There were fewer cells attached, proliferating and viable on the 3600 pattern compared to the 1800 pattern. Finally, the relative GFAP and MAP2k1 gene expression was lower on the 3600 pattern compared to the 1800 pattern. These results indicate that the addition of surface topography must be explicit. In fact,

studies have shown there are specific features sizes that induce special protein and cell reactions to the surface topography. Petrossians et al showed that there was less adhesion and proliferation of astrocytes and fibroblasts on carbon nanofibers compared to microcarbon fibers (Petrossians et al., 2011; Rose et al., 1985). Studies done by Shain et al found that astrocytes prefer to grow and adhere onto patterned surfaces of varying dimensions over smooth silicon surfaces *in vitro* (Kriparamanan et al., 2006; Szarowski et al., 2003). Seil et al studied the astrocyte adhesion and proliferation on zinc oxide nanoparticle polyurethane composites. They found that there was a significant decrease in astrocyte adhesion and proliferation when there were more zinc oxide nanoparticles on the surface (Rose et al., 1985). Collectively, it has been shown that cells are very particular to the surface they grow on; their response varies with minute feature alterations on the nanoscale. Our study confirmed this marvel, exhibiting that an increase of 278nm in nanogroove width elicits varied protein and cell response.

The mechanism involved with the cellular response to a nanopatterned surface is not well understood. As previously mentioned, it is thought that the effects of the surface topography either directly influence the cell response, or indirectly effect the cell responses through the affects they have on the adsorption of proteins (Kriparamanan et al., 2006). This study showed that both of these thoughts are accurate. The cells' proliferation, viability, adhesion, alignment and gene expression without protein adsorption and determined the nanopattern affected all of these cell responses was studied. Furthermore, the protein adsorption, rate of adsorption, the cells' adhesion and alignment on surfaces coated with proteins was examined. It was determined that the protein and cell response was affected. Indeed, it was demonstrated that protein coating on the surface increased cell adhesion and alignment, however, this occurrence was found regardless of protein coating. Nanoscale surface features better imitate the nanoscale protein rich

environment of the ECM found *in vivo* (Rose et al., 1985). The surface area of the nanoscale roughness samples is much larger, therefore allowing for more interaction between the cells and proteins on the surface (Rose et al., 1985). Moreover, nanomaterials have more of a surface energy than flat surface due to their increase in grain boundaries. This increase of surface energy is thought to not only increase the amount of protein adsorption, but the conformation of the proteins adsorbed as well (Rose et al., 1985).

6.5 Conclusion

Results of this study agree with current literature showing that topography effects protein and cell behavior. It was found that both proteins and cells were affected by the nanopatterning of PMMA. The aim of the current study was to determine optimal feature sizes for neural electrode fabrication, which was defined as eliciting a non-reactive astrocytic response. The 3600 patterned surface was determined to elicit less of a response as compared to the other patterned and non-patterned surfaces. The surface instigated cell alignment along the nanopattern, less protein adsorption, less cell adhesion, proliferation and viability, inhibition of GFAP and MAP2k1 compared to all other substrates tested. Further investigation applying these feature sizes in an *in vivo* setting is required to fully appreciate the beneficial effects of this specific nanopatterned surface.

CHAPTER 7

7.1 Comparative Assessment of Iridium Oxide and Platinum Alloy Wires using an *in vitro* Glial Scar Assay

There has been great advancement in neural prostheses research over the last 35 year (Mian et al., 2005). Currently, over 200,000 devices are implanted into patients (Gobbels et al., 2010; Mian et al., 2005). The majority of these devices are either implanted into the spinal cord or a peripheral nerve. To date, there are limited clinical microelectrodes that are implanted in the brain (Mian et al., 2005). The long-term effect of chronically implanted electrodes is the formation of a glial scar made up of reactive astrocytes and the matrix proteins they generate (Polikov et al., 2005; Seil and Webster, 2008). The prolonged excitation of neurons due to the over stimulation of electrode materials has shown to cause damage to the electrode and the neural tissue (Agnew et al., 1986; Cogan et al., 2004a; Negi et al., 2010b). Tissue damage is thought to occur from either initial bio-incompatibility of the electrode materials or the result of electrical overstimulation of the material which causes leaching of toxic by-products from the electrode materials into the physiological environment (Cogan et al., 2004a; McCreery et al., 1990; Negi et al., 2010b).

Ideal electrode materials should have low impedance, high capacitance and should be able to deliver a charge to the interface and tissue without inducing chemical reactions on the electrodes (Kotov et al., 2009; Negi et al., 2010a; Negi et al., 2010b). Higher charge injection capacity is thought to lower the potential required for stimulation, thus reducing the injury at the stimulation site (Negi et al., 2010a). Higher charge injection capacity (mC/cm^2) requires less area to transfer charge, therefore allowing neural electrodes to be smaller in size (S. Negi, 2009).

Smaller electrodes would have many advantages such as increasing neural selectivity, decreasing the immune system response and reducing neural damage (Kotov et al., 2009; S. Negi, 2009).

Currently, two of the most widely used conductive materials in neural electrodes are platinum and iridium oxide. Platinum is widely used for neural stimulation because it is resistant to corrosion and can transfer charge using reversible reactions that do not harm tissue (Merrill et al., 2005; Petrossians, 2011). Platinum has charge injection capacities in the range of 50-150$\mu C/cm^2$ (Cogan et al., 2005; Negi et al., 2010a; Rose and Robblee, 1990). Recent studies have shown platinum iridium alloys are more desirable biomaterial for electrodes due to their larger charge injection capacities (300 $\mu C/cm^2$), lower electrochemical impedance, and increased mechanical properties compared to pure platinum (Kotov et al., 2009; Negi et al., 2010a; Petrossians, 2011; Petrossians et al., 2011; Rose and Robblee, 1990). Iridium oxide has some advantages over platinum for neural stimulation electrode material due to its higher charge injection capacity, resistance to corrosion and lower impedance (Negi et al., 2010a; Negi et al., 2010b; S. Negi, 2009). Moreover, iridium oxide is well known for its reversible redox reactions which significantly increase the charge injection capacity to the range of 2-3 mC/cm^2 (Cogan et al., 2005; Kotov et al., 2009; Negi et al., 2010b).

There have been numerous studies on the mechanical and electrical properties of materials used in neural electrode devices. Studies have proven that there is neuronal tissue damage due to prolonged stimulation of electrode materials. However, it is unclear whether the damage is strictly due to the electrical stimulation, or bio-incompatibility of the electrode materials. There is a huge gap in research studying the biocompatibility of neural electrode biomaterials (Ereifej et al., 2011). After two decades of *in vivo* testing, the mechanism depicting

the failure of chronic neural electrodes was still unclear. Moreover, studies involving *in vivo* implantation are expensive, time consuming, and almost impossible to control at a molecular level in which the mechanisms of failure can be understood (Achyuta et al., 2010; Polikov et al., 2006; Polikov et al., 2005). Recently, Polikov et al adapted an *in vitro* glial scar assay in order to assess the inflammatory response on a molecular level (Achyuta et al., 2010; Polikov et al., 2006). They remarked on the benefits of having an *in vitro* system mimicking the effects of the *in vivo* world. Polikov et al adapted an *in vitro* cell culture system developed by Hong et al (Polikov et al., 2006). Hong et al used this model to test the neuroinflammatory mechanisms behind neurodegenerative diseases (Polikov et al., 2006). This model allows for the dissection of the brain at a detailed cellular level; containing neurons, astrocytes, and microglia, which are believed to produce the "glial scar" (Achyuta et al., 2010; Polikov et al., 2006; Polikov et al., 2005).

Both platinum alloy and iridium oxide have been identified as good candidates as neural electrode biomaterials due to their mechanical and electrical properties, however, effect of glial scar formation for these two materials is lacking. It is imperative to assess the biocompatibility of materials before employing them in neural electrode fabrication. Recent work performed in our lab utilized a combination of techniques for characterizing the biocompatibility of cells *in vitro* on neural electrode materials (Ereifej et al., 2011). In this study, we applied a glial scarring assay to observe the cellular reactivity to platinum alloy and iridium oxide wires in order to assess the biocompatibility based on previously defined characteristics. Through real-time PCR, immunostaining and imaging techniques, we will advance the understanding of the biocompatibility of these materials.

7.2 Methodology

7.2.1 Materials

Platinum alloy wires (80% platinum and 20% iridium) were produced by California Fine Wire Company. Platinum wires had a 20 μm diameter. Iridium oxide thin films were deposited on platinum wires using a pulsed-DC magnetron (using an unbalanced, planar magnetron source model ST20 from AJA International, and plasma power supply, model MDX 1.5K from Advanced Energy) reactive sputtering technique in Ar/O_2 plasma. The Ir sputtering target (Plasmaterials, INC) had a diameter of 2 inch (purity 99.9%). A thin titanium adhesion layer was deposited in the same sputtering process. Prior to deposition the chamber was evacuated to a base pressure of 10^{-7} Torr by a mechanical pump first and then by a cryogenic pump. The sputtering power was fixed at 150W with a pulsing frequency of 100 kHz and reverse bias duration of 2μsec. The oxygen flow rate was maintained at 8 sccm and the argon flow rate was maintained at 40 sccm. The sputtering pressure was maintained at 5mTorr. The amorphous films were sputtered at room temperature. A Dektak profilometer was used to measure the thickness of the IrO_2 thin film and was found to be 200 nm. Materials were washed using an Ultraomet 2003 Sonic Cleaner (Buehler, Bluff, IL) in ethanol, followed by distilled water, for 15 minutes in each solvent. Samples were autoclaved for 30 minutes at 121^{o}C and sterilized under UV light. Sterilized wires were cut into 5mm pieces, of which one wire was placed into each well over the cultured cells. Controls were the cells growing on the poly-d-lysine (MW 30-70k, Sigma-Aldrich, St. Louis, MO, P6407) coated glass wafers without wires.

7.2.2 Surface Chemistry Characterization

To characterize the surface composition of the elements found in IrO_2, a high resolution x-ray photoelectron spectroscopy (XPS) using monochromatic AlKa radiation in a Perkin Elmer

model S500 XPS Spectrometer was used. This technique was used to confirm iridium was present (Figure 39).

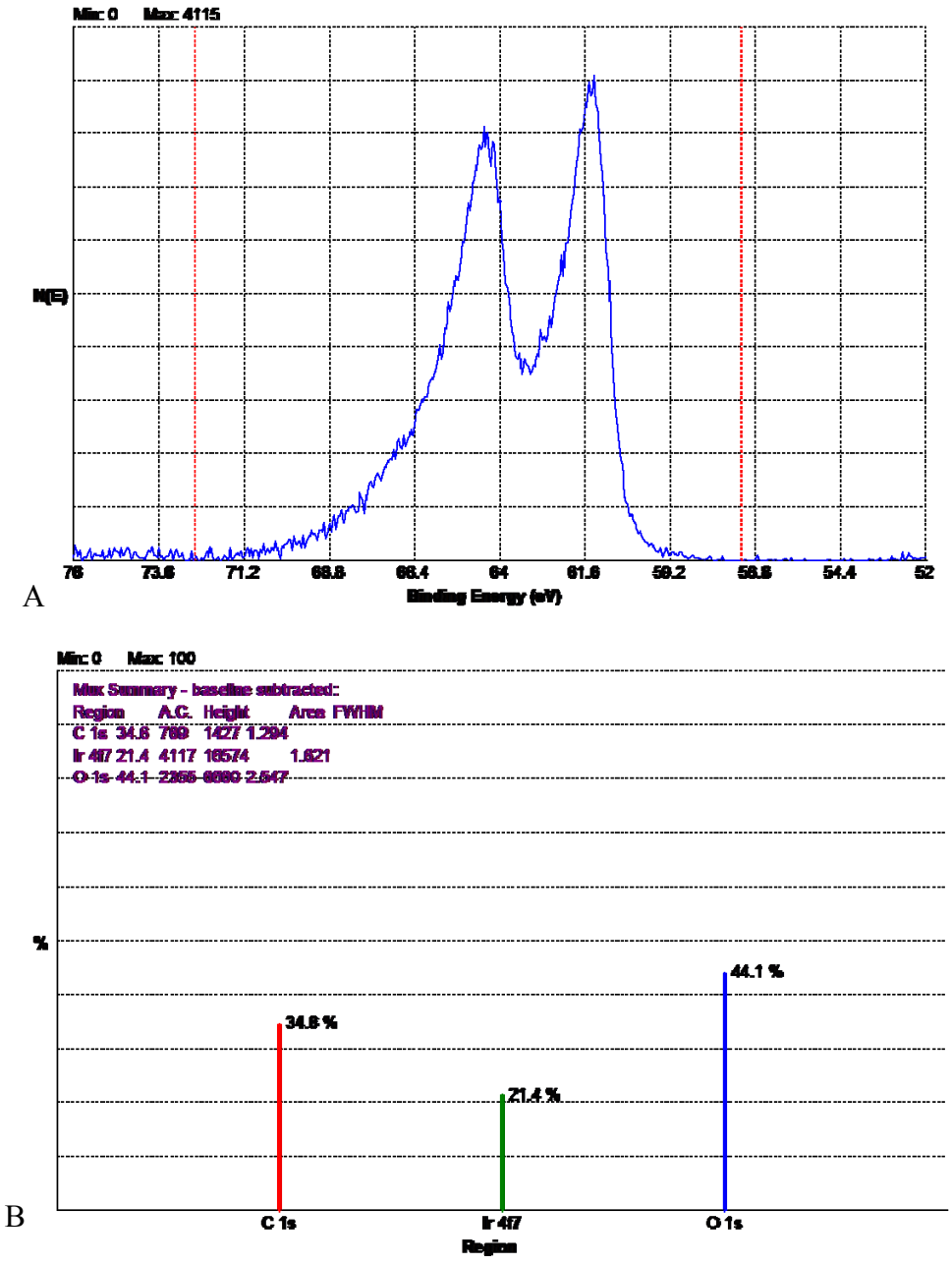

Figure 39. A) High Resolution XPS on IrO2 wire. The y-axis displays the number of electrons measured, while the x-axis shows the binding energy of the electrons. B) Iridium peak from XPS survey scan. The composition of sputtered iridium oxide thin film was confirmed to be IrO_2 by high resolution XPS scan.

7.2.3 Primary Mixed Neuronal Cell Culture

The Wayne State University Institutional Animal Care and Use Committee approved experimental protocols described herein. A mixed neuronal cell culture (including neurons, astrocytes and microglia) was isolated from Sprague-Dawley embryonic day 17 rat pups. The mother rat was euthanized by rapid asphyxiation with carbon dioxide (CO_2) gas; assurance of death was conducted by a thoracotomy. Rat pups were dissected out following Liu et al's protocol and then decapitated (Liu and Hong, 2003). Cortex tissues of the pups' brain were dissected in sterile Hank's Buffered Sodium Solution (HBSS) containing 1% penicillin-streptomycin. Following which, the tissues were dissociated and seeded at a density of 7×10^5 cells/well. Prior to seeding, 5mg of poly-d-lysine (MW 30-70k, Sigma-Aldrich, St. Louis, MO, P6407) was dissolved in 250mL of DNA/RNA free distilled water (sterilized by 0.22um filter). The poly-D-lysine was coated onto the samples (1ml/well) and incubated overnight at 37^{o}C. This altered the surface charge allowing the neurons to adhere onto the surface. The wells were then washed twice with sterile distilled water and once with sterile HBSS. The cells were maintained in 56% minimal essential medium (MEM), 20% Dulbecco's Modified Eagle's Medium (DMEM), 10% fetal bovine serum (FBS), 10% horse serum (HS), 4% penicillin/streptomycin. The samples were housed in a humidified incubator with the following setting conditions: 90% humidity, 5% CO_2 and 37.8^{o}C.

7.2.4 Real Time PCR

Real time PCR was used to measure gene expression from samples relative to the control. The total RNA from the cells was extracted on day one, four and seven post seeding with Trizol (Invitrogen, Carlsbad, CA) following the manufacturer's protocol. The RNA concentration and purity was determined using a spectrophotometer through UV absorbance at 260nm and 280nm.

Reverse transcriptase using the random primers converted the mRNA to a cDNA template using a thermal cycler (Mastercycler Gradient, Eppendorf, Hauppauge, NY). For PCR analysis, we used cDNA equivalent to 40ng of total RNA. Specific primer pairs (Table 5) for astrocyte activation, glial fibrillary acidic protein (GFAP) were employed. As an internal control, we used the house-keeping gene glyceraldehyde-3-phosphate dehydrogenase (GAPDH). The PCR master mix included 1 x SYBR® Green (Applied Biosystems, Foster City, CA), and forward and reverse primers (0.4μM each). cDNA templates and master mix were read in a 96-well optical plate using a 7500 Fast Real-Time PCR System (Applied Biosystems, Foster City, CA). The following profile was used: 50°C for 2 min, 95°C for 10 min, and 40 cycles of 95°C for 15s and 60°C for 1 minute. Threshold cycle (Ct) values for each sample and primer pair were obtained and analyzed with the delta-delta (ΔΔ) Ct method (Livak and Schmittgen, 2001; Schmittgen and Livak, 2008) in order to calculate the fold change (R) in each target gene. The following equations were used:

$$\Delta Ct = Ct_{sample} - Ct_{GAPDH}$$

$$\Delta\Delta Ct = \Delta Ct_{test\ surface} - \Delta Ct_{control\ surface}$$

$$R = 2^{-\Delta\Delta Ct}$$

Table 6. Primer sequences for real-time PCR used in glial assay studies.

Cells	Category	Gene	Primer Sequence
Primary brain cells	Housekeeping gene	GAPDH	5'-TGGCCTTCCGTGTTCCTACC-3' (F)
			5'-AGCCCAGGATGCCCTTTAGTG-3' (R)
	Activation gene	GFAP	5'-GTTGTGTTCAAGCAGCCTGG-3' (F)
			5'-CCAGTGAGTAAAGGTGACAG-3' (R)

7.2.5 Immunostaining

The mixed primary brain cell cultures were stained with fluorescent antibodies in order to image each cell type specifically. At day seven post seeding, the cells were fixed in a 4% paraformaldehyde solution for 20 minutes at room temperature. Following three rinses in 1×PBS, the samples were incubated in a 0.25% Triton solution (in 1×PBS) for 20 minutes at room temperature (RT) in order to permeate the cell's membrane and then rinsed three times with 1×PBS to ensure all of the detergent was removed. After which, the cells were blocked for one hour in a 5% goat serum at RT. Milli-Mark Pan Neuronal Marker (Millipore, Billerica, MA) was used to stain neurons (1:500 in 1×PBS), for two hours at 37^{o}C. Samples were washed with 5% fetal bovine serum (FBS) blocking solution (in 1×PBS) for ten minutes each wash for a total of three washes. Alexa Fluor 488 goat anti-mouse IgG (Abcam, Cambridge, MA) secondary antibody (1:2000 in 1×PBS) was applied for one hour in the dark at RT. Cells were then washed three times with 1×PBS and blocked with 5% FBS for one hour in the dark at RT. Astrocyte specific primary antibody, GFAP (Millipore, Billerica, MA) was used to stain astrocytes (1:1000 in 1×PBS) for two hours at 37^{o}C. Cells were washed with 5% FBS three times before adding the secondary antibody for the astrocytes. GFAP Alexa Fluor 555 goat anti-rabbit IgG (Invitrogen, Carlsbad,CA) secondary antibody (1:2000 in 1×PBS) was used for one hour in the dark at RT. Samples were washed three times with 1×PBS and blocked for one hour in 5% FBS at RT in the dark. Triple staining of the nucleus was done using 2□g/mL of 4',6-diamidino-2-phenylindole (DAPI; Sigma-Aldrich, St. Louis, MO) for 20 minutes at RT in the dark. The samples were mounted on glass slides using ProLong Anti-Fade Gold reagent (Invitrogen, Carlsbad, CA) and viewed under a Zeiss Axio Observer Inverted Microscope (Carl Zeiss Inc).

7.2.6 Image Analysis

Image J software was used to measure the scar thickness, mean GFAP and DAPI intensities around the wires. Each image was first converted to an 8-bit grayscale, following which a threshold binary image was created. The thickness of the scar was found by measuring the width, from the edge of the wire to the edge of the scar, on each side then averaged. Grids made up of two rows, with eight boxes total (four boxes per row and the area of each box being 100 μm^2), were overlaid on top of the DAPI and GFAP images along the length of the wire. Only the area inside of the grid was used for measuring. The mean GFAP and DAPI intensities were measured using the same grid procedure. The average area within the grid stained with either GFAP or DAPI respectfully was then measured using the analyze particles function.

7.2.7 Statistical Analysis

All of the data are presented as a mean ± standard error of the mean. Experiments were performed with samples sizes of three to five and repeated three independent times. There were minimally 15 samples analyzed per group. PASW software (version 18.0) was utilized for statistical analysis. A nonparametric statistical analysis was used to test for statistically significant differences between the different material groups over time for the RTPCR, scar thickness and imunostaining studies. Parametric statistical methods could not be completed due to insufficient power from a small sample size, mean values were either not normally distributed or the variances of the data were not heterogeneous. The exact tests were conducted in order to be able to make reliable inferences by computing exact p values for a very wide class of hypothesis tests, including one-, two-, and K sample tests, tests for unordered and ordered categorical data, and tests for measures of association.

7.3 Results

7.3.1 Scar Thickness

Results demonstrated that scar thickness decreased around both the platinum alloy and the IrO_2 wires with time (Figure 40). Compared to day one, the scar thickness around the IrO_2 wires had significantly decreased ($p<0.01$) by days four and seven. Scar thickness around the platinum alloy wires also had a significant decrease in thickness ($p<0.01$) by day seven compared to days one and four. When comparing the materials, it was found that the scar thickness around the platinum alloy wires was significantly less ($p<0.05$) on day seven compared to the IrO_2 wires.

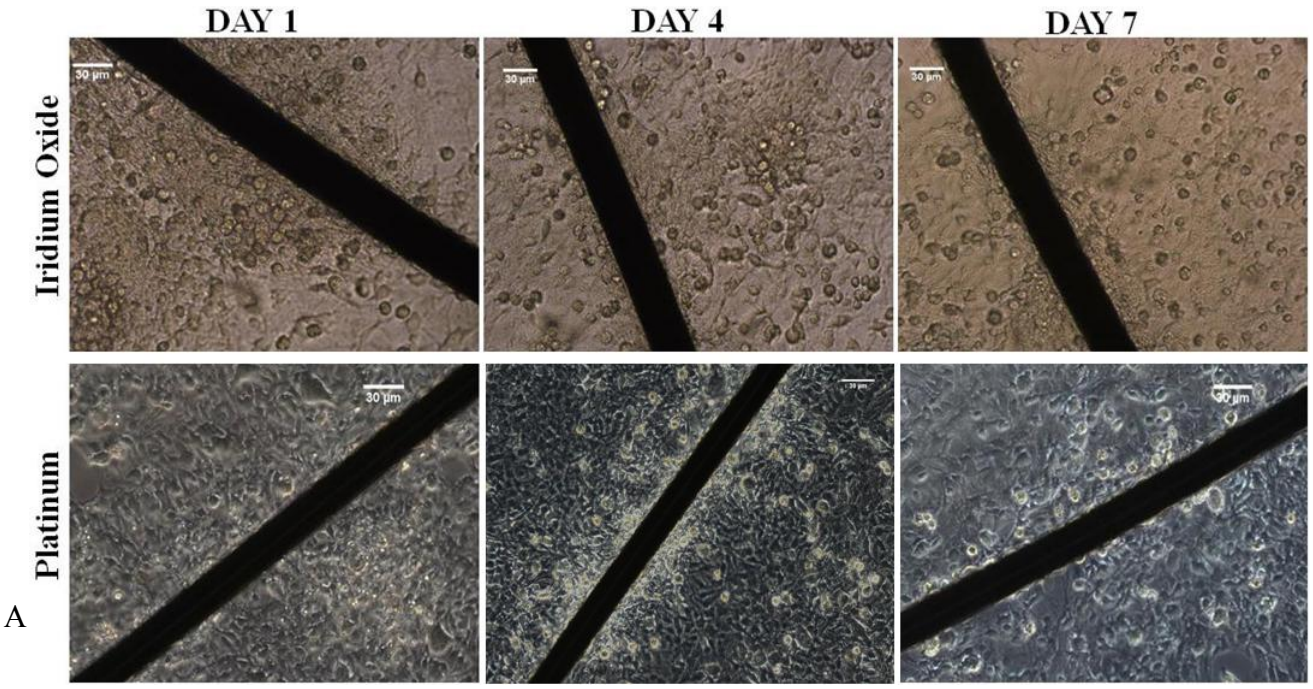

A

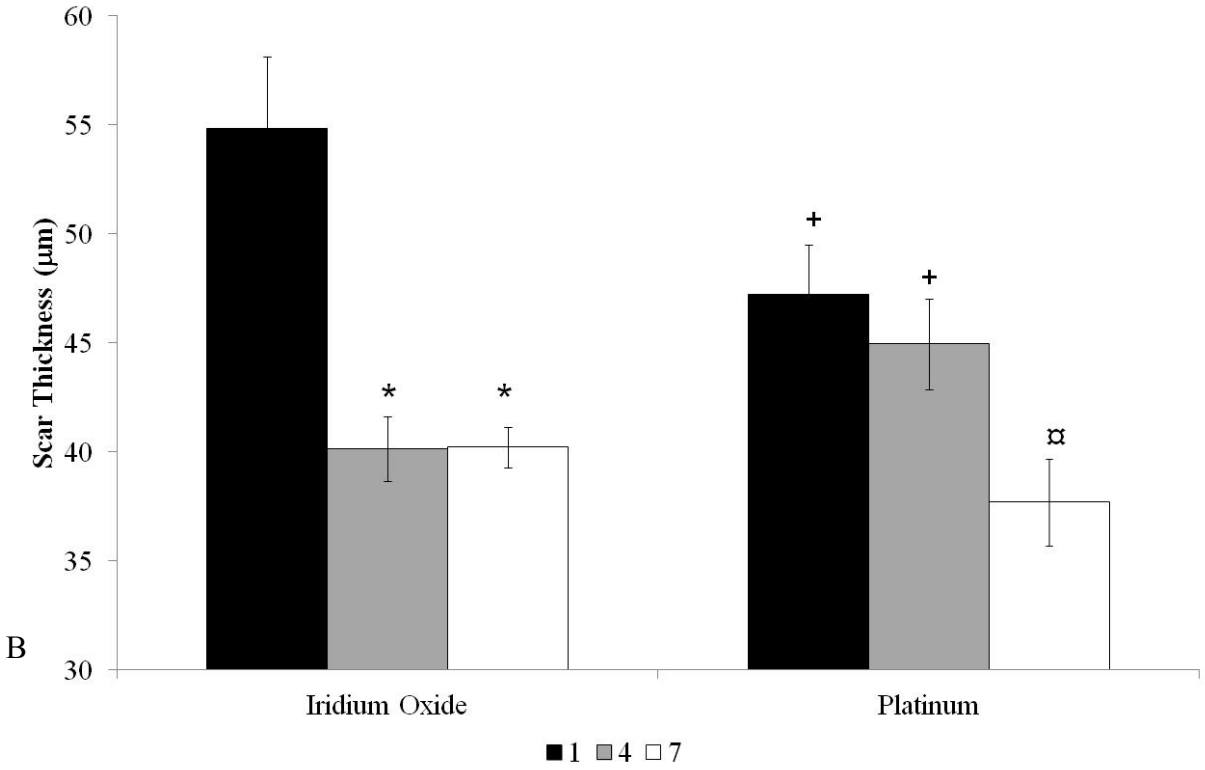

Figure 40. A) Phase contrast images of glial scar over time. B) Scar tissue thickness measurement. Both IrO2 and Pt wires had a decrease in scar thickness. IrO2 had a thicker scar on days one and seven compared to Pt. *$p<0.01$ data compared to IrO2 on day one, +$p<0.01$ data compared to platinum alloy on day seven, ¤$p<0.05$ data compared to IrO_2 on day seven

7.3.2 Relative Gene Expression

Cells cultured with IrO_2 wires had significantly higher ($p<0.01$) GFAP relative gene expression on day one compared to both the control and those cultured with platinum alloy wires (Figure 41). There was not any statistical significance found on days four and seven. However, it is important to note that cells cultured with platinum alloy wires had less GFAP gene expression compared to IrO_2 wires on all three days.

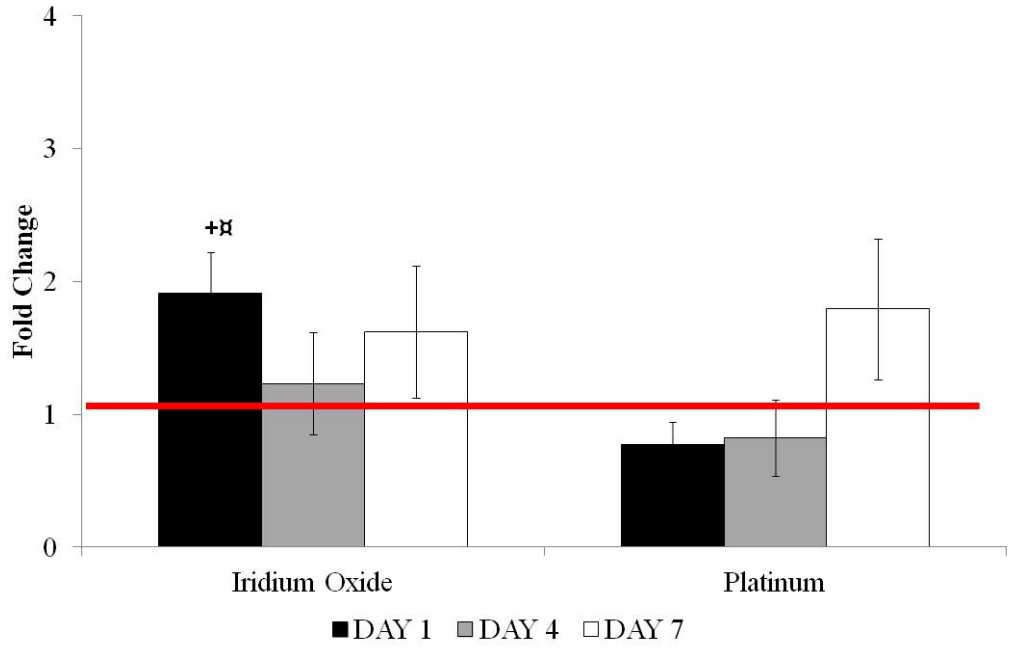

Figure 41. RTPCR GFAP relative gene expression. The control is represented by the red horizontal line. +p<0.01 compared to platinum alloy on day one, ¤p<0.01 compared to control on day one. Cells cultured with platinum alloy wires had overall lower levels of GFAP expression compared to IrO_2 wires.

7.3.3 Immunostaining

Immunostaining of neuronal cells' nuclei and activated astrocytes revealed not only fewer activated astrocytes around platinum alloy wires, but fewer cells overall compared to IrO_2 wires (Figure 42). The mean GFAP fluorescence intensity was significantly elevated ($p<0.01$) in cell cultures with IrO_2 wires compared to cultures with platinum alloy wires and control cultures without any wires (Figure 43). Control cultures had significantly lower ($p<0.01$) GFAP mean intensities compared to cell cultures with either the platinum alloy or IrO_2 wires. The mean DAPI intensity of cells cultured with platinum alloy wires was significantly lower ($p<0.01$) compared to control and IrO_2 wires cultures (Figure 44).

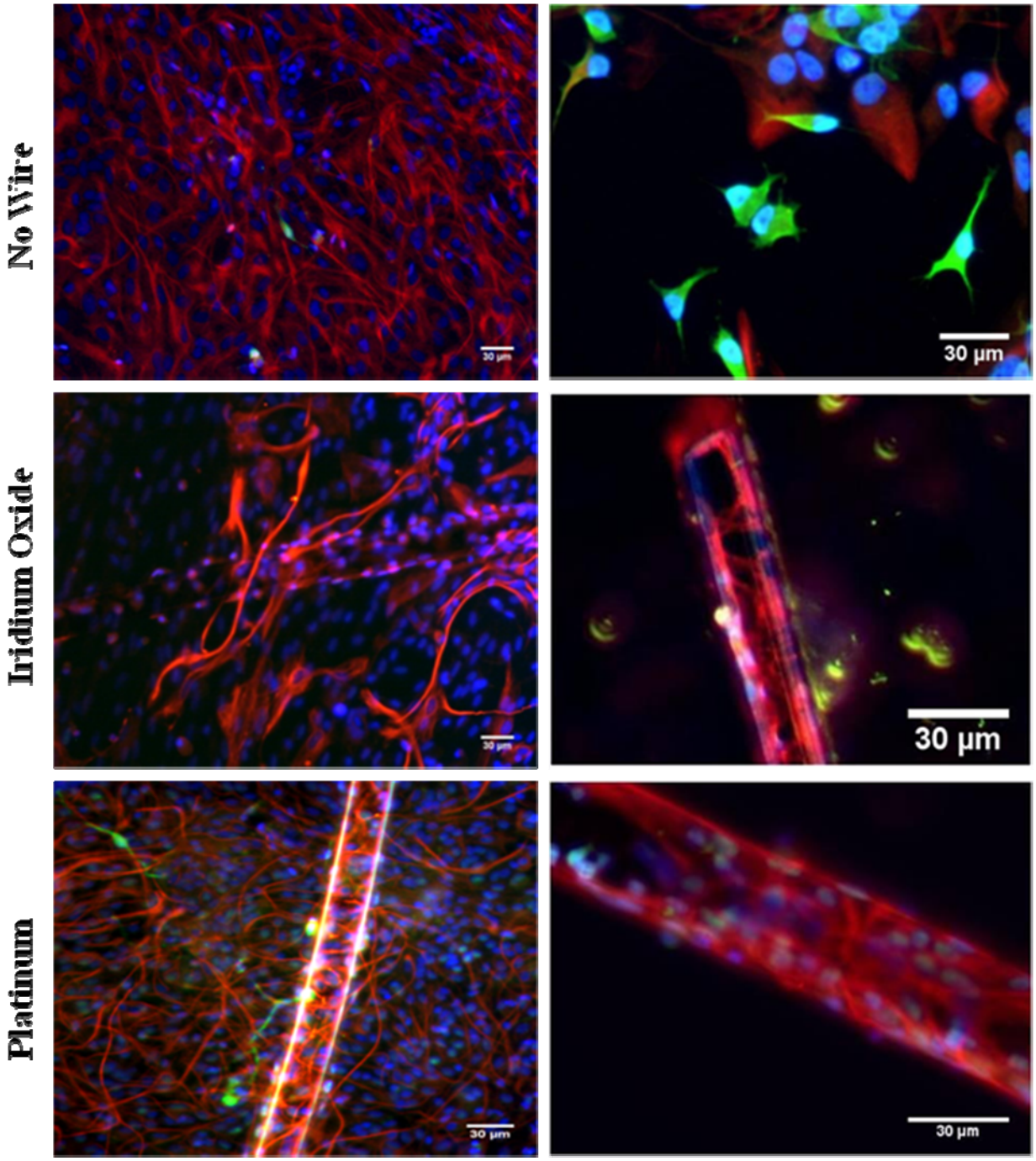

Figure 42. Triple fluorescent labeling with DAPI staining cell nuclei (blue), GFAP staining astrocytes (red), and Millimark staining neurons (green). Images were taken at day seven.

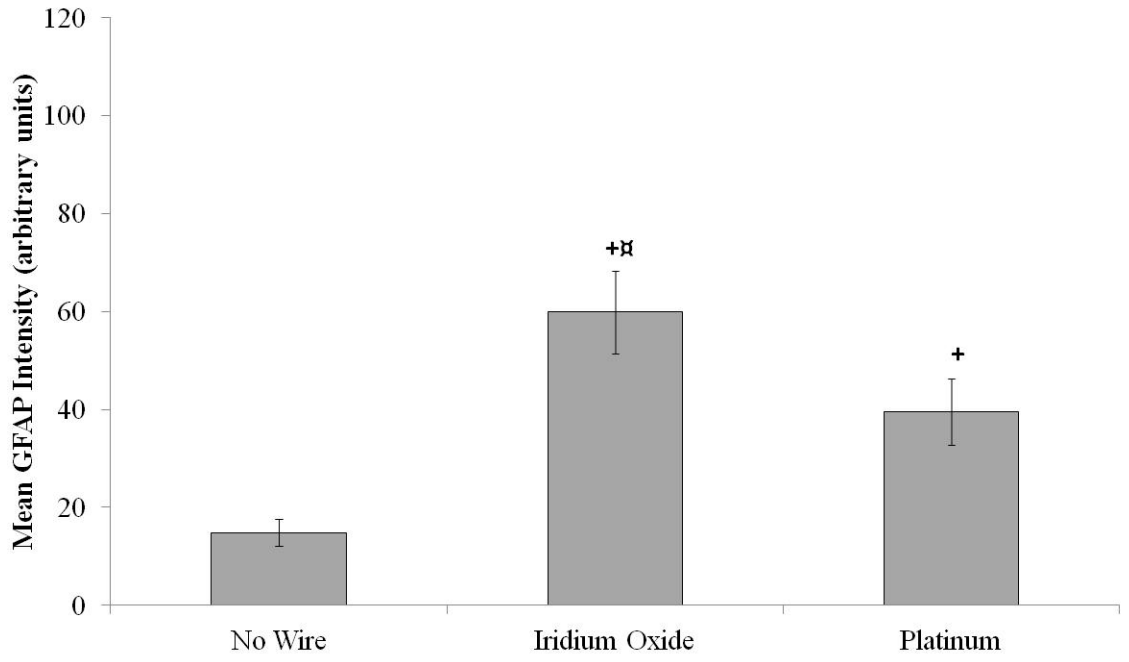

Figure 43. Mean GFAP fluorescence intensity within a distance of 100 µm on either side of the wire on day seven. +p<0.01 data compared to control (no wire), ¤p<0.01 data compared to platinum alloy. Platinum alloy wires had the lowest mean GFAP intensity

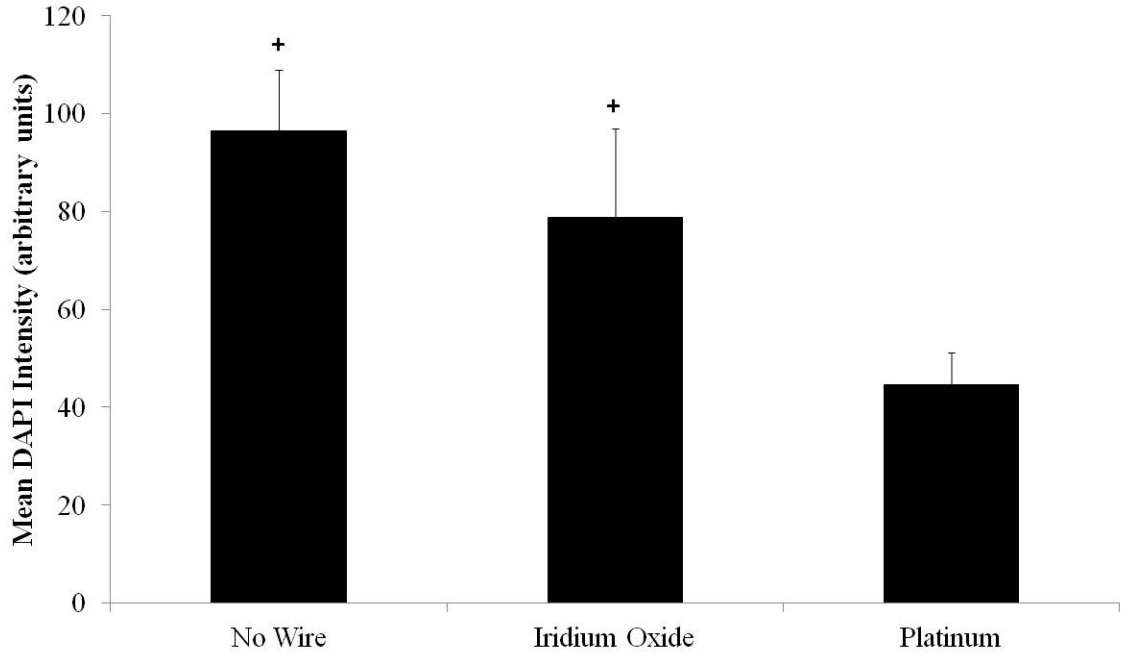

Figure 44. Mean DAPI fluorescence intensity within a distance of 100 µm on either side of the wire on day seven. +p<0.01 data compared to platinum alloy. Platinum alloy wires had the lowest mean DAPI intensity.

7.4 Discussion

There is limited information assessing the biocompatibility of neural electrode materials, especially the biomaterials used to electrically stimulate the neurons, such as iridium oxide and platinum alloys. In fact, the few studies involving cells to calibrate biocompatibility of these materials have only utilized neurons (Gobbels et al., 2010; Khan and Newaz, 2010; Lee et al., 2003; Thanawala et al., 2007). These types of studies have classified platinum alloys and iridium oxide as biocompatible on the basis that neurons grew on top of the materials, usually requiring a protein coating such as poly-d-lysine (Gobbels et al., 2010; Khan and Newaz, 2010; Lee et al., 2003; Thanawala et al., 2007). Although it is imperative for the electrically stimulating biomaterial to attract neurons, it is equally crucial for the material to also evade glial cell activation and prevent the formation of glial scars.

It has been established that the inflammatory response within the brain tissue is characterized by the presence of reactive astrocytes and microglia, which form the glial scar around the implanted electrode (Kidambi et al., 2010; Szarowski et al., 2003). Furthermore, activated astrocytes are identified as hypertrophic, hyperplasic, have an upregulation of intermediate filament GFAP and filament formation (Gervasi et al., 2008). This study employed the distinguished characteristics of an inflammatory response in order to determine the biocompatibility of platinum alloy and iridium oxide wires for the use of neural electrode fabrication. We measured the thickness of the scar tissue around the wires, the relative gene expression of GFAP, the fluorescence intensity of GFAP and DAPI as markers of biocompatibility.

The glial scar functions to encapsulate the electrode, separating the damaged brain tissue and the foreign device from the undamaged, healthy tissue (Polikov et al., 2005). This normal defensive mechanism leads to an increasing distance between the electrode and its target neurite processes. Thus, increasing the impedance of the electrode and decreasing signal strength (Polikov et al., 2005). The strength and quality of the recorded electrical signal is determined by the location of the neuron in relation to the electrode recording sites. In order to maintain a recording and accurately observe action potentials, the maximum distance between neuron and electrode, commonly referred to as the "kill zone", can only be between 50-100 μm (McCreery and Agnew, 1983; Polikov et al., 2005; Turner et al., 1999; Wang et al., 2011).

In vivo and *in vitro* studies have shown over time, the glial scar decreases in thickness, however it becomes denser and more organized (Achyuta et al., 2010; Polikov et al., 2006; Szarowski et al., 2003; Turner et al., 1999). We found a similar trend with both the platinum alloy and IrO_2 wires; the scar thickness decreased inversely proportional with time, therefore making this *in vitro* data credible. Interestingly, the glial scar formed around either the platinum alloy or IrO_2 wires in this study was a fraction of the size (40 - 60μm) compared to glial scars found in previous literature (50 - 600μm) both *in vivo* (Szarowski et al., 2003; Turner et al., 1999) or *in vitro* using comparable cell seeding densities (Polikov et al., 2006; Polikov et al., 2009). The compactness of the scar thickness measured in this study implies less of an inflammatory response. Although in comparison to each other, the platinum alloy wires have proven to be more biocompatible, the IrO_2 wires are not necessarily bio-incompatible.

Results of the RT-PCR and GFAP immunostaining validated one another. The RT-PCR findings demonstrated less GFAP relative gene expression from astrocytes in culture with the

platinum alloy wires compared to the IrO_2 wires on all three time points. Moreover, the mean GFAP fluorescence intensity was lower with the platinum alloy wires compared to the IrO_2 wires. Increased GFAP expression is an indication of reactive astrocytes. Studies have shown that the molecular composition of the glial scar and the production of inhibitory molecules by reactive astrocytes impair axon regeneration (2003; Seil and Webster, 2008). Astrocytes in the glial scar are known to upregulate inhibitory molecules, such as, chondroitin sulfate proteoglycans (CSPGs), tenascin, Semaphorin 3, ephrin-B2, and slit proteins which play a role in the CNS axons inability to regenerate (Fitch and Silver, 2008). It has been shown that reactive astrocytes secrete proteoglycans that inhibit the growth of neuritis in injured spinal cord and brain models (Griffith and Humphrey, 2006). These results suggest that there were fewer activated astrocytes around the platinum alloy wires, thus signifying platinum alloy wires to be more biocompatible compared to IrO_2 wires.

Furthermore, platinum alloy wires had the lowest mean DAPI fluorescence intensity compared to IrO_2 wires. This further validates the superior biocompatibility of platinum alloy wires compared to the IrO_2 wires. IrO_2 wires having higher levels of DAPI intensity indicates the presence of more cells than around the platinum alloy wires. Neurons make up less than 25% of the cells in the brain, which leaves the other 75% to be a combination of glial cells (Polikov et al., 2005). Therefore, the majority of the cells around the wires are made up of astrocytes and microglia, both of which are undesirable to have around electrodes. Studies have shown that increased proximity of glial cells to neural electrodes are directly correlated with increased glial scarring and reduced neuron viability (Achyuta et al., 2010; Biran et al., 2005; Szarowski et al., 2003; Turner et al., 1999).

Previous studies comparing the mechanical and electrical properties of platinum alloys to IrO_2 always depict IrO_2 as the superior material. However, comparison of the biocompatibility of these two materials reveals platinum alloys to be superior. Thanawala et al observed the adhesion of cortical neurons isolated from rat embryo brain onto platinum and IrO_2 film strips (Thanawala et al., 2007). They found poor cell attachment on IrO_2 surfaces compared to platinum surfaces, thus indicating superior biocompatibility of the platinum surface. Potential differences between the documented studies, such as utilizing neurons alone or the use of mixed cell cultures, appear to confirm the importance of the glial cells when evaluating material compatibility.

7.5 Conclusions

It is well known that when compared by electrical properties, such as impedance and charge injection capacity, iridium oxide has the advantage with lower impedance and a higher charge injection capacity compared to platinum, thus making it more favorable for neural electrode fabrication. However, results of this study demonstrate that although the electrical properties may be better, iridium oxide wires exhibited a more significant reactive response as compared to platinum alloy wires. Cells cultured with platinum alloy wires had less GFAP gene expression, lower average GFAP intensity, and smaller glial scar thickness. Collectively, these results indicated that platinum alloy wires were more biocompatible than the iridium oxide wires. Future research involving functionality of neurons as well as further glial scar assessment will substantiate our current findings.

CHAPTER 8

8.1 Assessment of Organotypic Brain Slice Response on Nanopatterned Polydimethylsiloxane Surface

A long-term effect of chronically implanted neural electrodes is the formation of a glial scar made up of reactive astrocytes, microglia and the matrix proteins they generate (Polikov et al., 2005; Seil and Webster, 2008). The initial response to implanted electrodes is an acute neuroinflammation mediated by microglia followed by astrocyte reactivity, which leads to astrogliosis (Rao et al., 2012; Sofroniew and Vinters, 2010). Studies have shown that a variety of cytokines are involved with the initial and modulation phases of reactive astrogliosis (Farina et al., 2007; John et al., 2003; Liberto et al., 2004; Rao et al., 2012). These cytokines include interleukin-1beta (IL-1β), tumor necrosis factor alpha (TNFα), and transforming growth factor beta 1 (TGFβ1). Astrocytes express receptors to this signaling molecules and their binding results in an astrocytic reactive response (Farina et al., 2007; John et al., 2003; Liberto et al., 2004; Rao et al., 2012). In addition to receiving these signals, astrocytes also can generate and release cytokines such as IL-1β and TNFα which promote neurotoxicity whereas TGFβ1 acts as a neuroprotective (Farina et al., 2007; John et al., 2003; Liberto et al., 2004; Rao et al., 2012). Another known marker for activated astrocytes is an upregulation of intermediate filament, glial fibrillary acidic protein (GFAP) (Gervasi et al., 2008; Polikov et al., 2006; Polikov et al., 2005; Szarowski et al., 2003; Turner et al., 1999). IL-1β, TNFα, and TGFβ1 can be expressed by both microglia and astrocytes (Farina et al., 2007; John et al., 2003; Liberto et al., 2004; Rao et al., 2012). The acute neuroinflammatory response is typically short-lived and unlikely to be harmful to neuronal survival (Glass et al., 2010; Rao et al., 2012; Yoles et al., 2001). The acute response can be resolved by a negative feedback mechanism resulting in reduced levels of IL-1β and

TNFα and increased levels of TGFβ1 (Liberto et al., 2004; Moolwaney and Igwe, 2005; Rao et al., 2012). Acute neuroinflammation is considered beneficial to the CNS, because it prevents further tissue destruction and contributes to repairing the damaged tissue (Liberto et al., 2004; Rao et al., 2012). Although the acute response is considered beneficial to the CNS, if not resolved, it will transform into a chronic response thus rendering in the formation of a glial scar around the implanted electrode. Therefore, the chronic presence of the electrode results in glial scarring around the implantation site which consequently impedes the electrode signal. One of the goals of neural electrode fabrication is to design a material that minimizes this acute neuroinflammation.

Current scientific strategies to inhibit the initiation of glial scarring around a chronic device range from altering the geometry, roughness, size, shape and materials of the device (Grill et al., 2009; Kotov et al., 2009; Kotzar et al., 2002; Szarowski et al., 2003). In order to properly design a successful neural electrode, biomedical engineers strive to understanding of the cellular environment. *In vivo* conditions comprise of cells living in the extracellular matrix (ECM) meshwork with a three-dimensional and high aspect ratio topographical textures on a micron and nano scale (Kriparamanan et al., 2006; Millet et al., 2010; Wu et al., 2006). This 3-D environment provides cells the topographical cues required for them to differentiate and perform their specific functions. Studies have shown that surfaces which mimic the nanotopography of the natural environment *in vivo* result in an improved biocompatible response (Curtis et al., 2004; Ding et al., 2010; Kotov et al., 2009; Millet et al., 2010; Zervantonakis et al., 2011). Nanotopography has been demonstrated to affect the cells' morphology, alignment, adhesion, proliferation, gene expression profiles and even prevent biofouling and contamination on the material's surface (Curtis, 2005; Curtis et al., 2004; Das et al., 2008; Fok-Seang et al., 1998;

Kriparamanan et al., 2006). Topography affects gene expression of cytokines, growth factors, signaling molecules, and cytoskeleton-linked molecules (Kriparamanan et al., 2006). Studies utilizing nanotopography with neural electrode materials have primarily focused on surface alterations of the active sites on the conducting material (Brunetti V, 2010; Gobbels et al., 2010; Negi et al., 2010a). Negi et al studied how increasing the surface area available for neuronal contact would improve the spatial resolution and selectivity (Negi et al., 2010a). Other studies examined the effect nanotopography has on glial cells, specifically on the reduction of the glial cells inflammatory response (Kotov et al., 2009; Pennisi et al., 2011; Pennisi et al., 2009).

In the present study, nanopatterning of polydimethylsiloxane (PDMS) was attempted as a method for reducing the inflammatory response of glial cells. PDMS elastomer is a standard material that is commonly used in studies involving topographical surface modifications due to its optimal physical properties. PDMS is an inexpensive, highly viscoelastic, hydrophobic polymer with fairly low surface energy and thermal stability (Berdichevsky et al., 2010; Choi et al., 2009; H. Makamba, 2003; Millet et al., 2007; Zervantonakis et al., 2011). PDMS provides easy release from the patterned substrate mold during processing which gives it the advantage of rapid prototyping capabilities and the ability to fabricate complex patterns down to the nanometer scale (Choi et al., 2009; H. Makamba, 2003; Millet et al., 2007; Zervantonakis et al., 2011). Moreover, devices fabricated with PDMS have been useful for biological studies due to their ease of fabrication, high gas permeability, optical transparency, and low water permeability of the structures formed from this material (David C Duffy, 1999; H. Makamba, 2003; Millet et al., 2007; Samuel K. Sia, 2003; T. C. Merkel, 2000). Recently, devices fabricated with PDMS have been incorporated as structural components for patterning neuronal growth in culture and

studying the neural circuit physiology (Berdichevsky et al., 2009; Berdichevsky et al., 2010; Hanson et al., 2009; Millet et al., 2007).

A unique feature of this study is the use of *in vitro* brain slice cultures (organotypic cultures) in order to more accurately depict the native response. Organotypic cultures are used due to their ability to retain circuit architecture, connectivity and physiology specific to their *in vivo* origin (Berdichevsky et al., 2009; Morin et al., 2006). Therefore, this culture system has many advantages over the traditional monoculture *in vitro* biocompatibility testing methods (Berdichevsky et al., 2009; Morin et al., 2006). The aim of the present study was to determine whether nanotopography can reduce inflammatory markers typically resultant from neural electrode implantation. The uniqueness of this *in vitro* model lies with the assumption that the slicing of the organotypic brain tissue elicits the typical injury found with neural electrode insertion. PDMS was spin coated on nanopatterned substrates, peeled and rolled into cylindrical pins in order to comply with the 3D geometry of neural electrodes. Thereafter, PDMS pins were placed in organotypic cultures for glial cell examination. Specifically, observation of cell alignment and surveillance of GFAP, IL-1β, TNFα, and TGFβ1 gene expression around the PDMS pins was performed.

8.2 Methodology

8.2.1 Material Fabrication

The method of nanoimprint lithography (NIL), otherwise known as hot embossing was utilized to create the nanopatterned surface. Specifically, the JenOptik HEX03 hot embossing system (SSIM laboratory at Wayne State University) was used. Goodfellow UV-grade PMMA was the substrate. The processing temperature was 105-195°C and the applied controllable force was 300N – 3kN. Molds were purchased from Edmund Optics (Barrington, NJ); reflective

holographic grated mold was used to make the patterned substrate with a period of 3600 grooves/mm, and a flat mirror mold was used for the non-patterned surface. The embossed substrates were cut into 1cm^2 wafers. PDMS was spin coated onto the PMMA wafers using a spin coater from Laurell Technologies Corporation (model: WS-650-23; North Wales, PA). The PDMS was purchased from Dow Corning, (Midland, MI; Sylgard 184 Elastomer kit) and prepared by mixing Sylgard 184 Silone Elastomer base and Sylgard 184 Silone Eastomer Curing agent (10:1, w/w). A 500 µl droplet was placed on the PMMA wafer. The program was set at 500rpm for five seconds and 1500rpm for 30 seconds. The samples were then baked at 60^{o}C for one hour. After cooling, the PDMS was peeled from the PMMA wafer and rolled around a 23 gauge needle to make cylinder pins, with the patterned side on the outside (Figure 45). PDMS samples were sterilized by washing with 70% ethanol and distilled water and left under UV light for one hour.

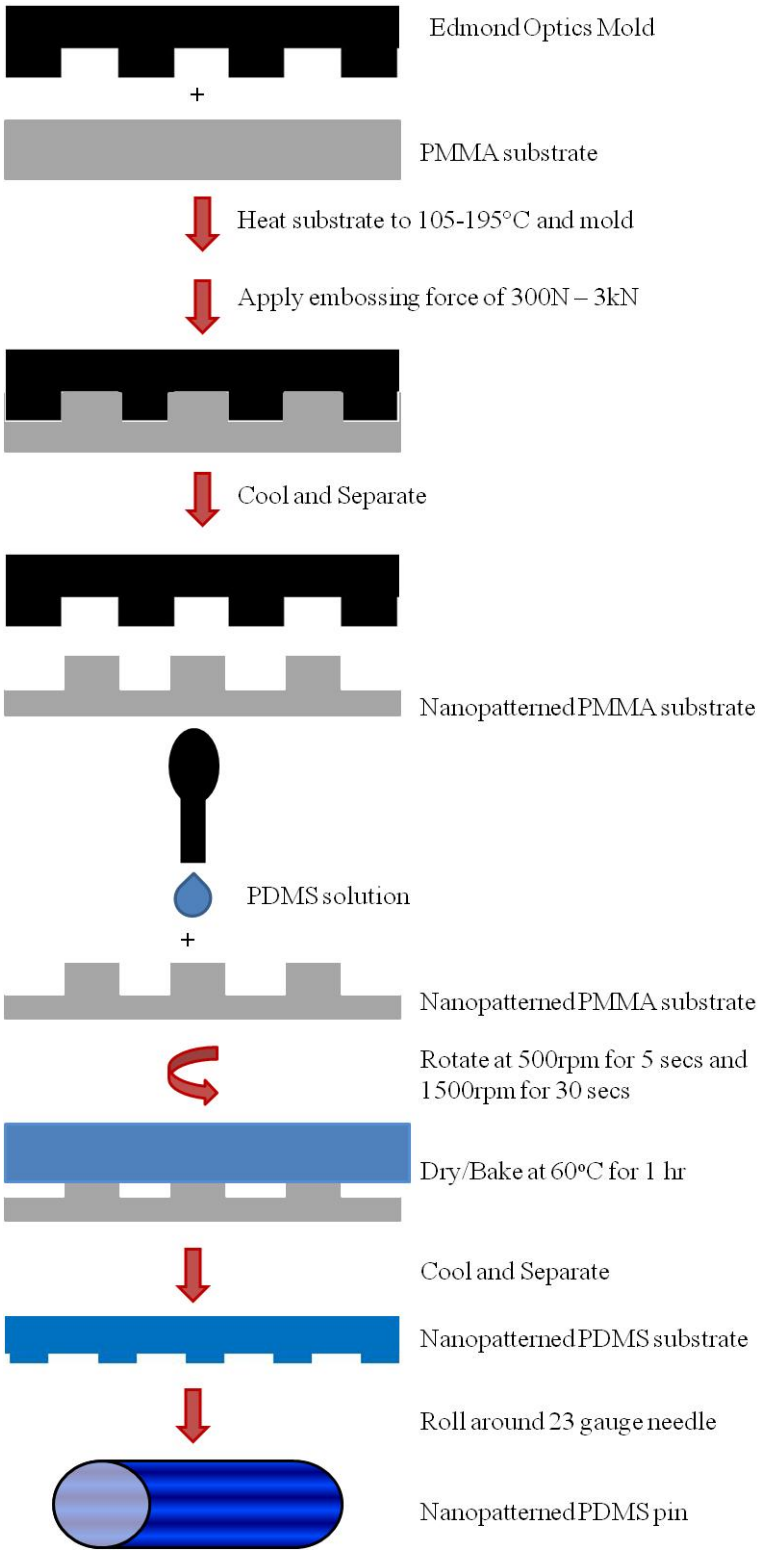

Figure 45. Schematic representation of material fabrication. Shown here is an example using the nanopatterned substrate; the same steps were used to make the non-patterned samples.

8.2.2 Atomic Force Microscopy

The dimensions of the nanopatterned PDMS substrates were characterized by Dimension 3100 AFM (VEECO) in the tapping mode in ambient air. The height, amplitude, and phase images were obtained using silicon tapping tips (nanoScience Instruments, VistruaProbes T300) with resonance frequency of 300 kHz and tip radius less than 10 nm. The scan rate was 1–3 Hz. Height images are plane-fit in the fast scan direction with no additional filtering operation. The dimensions of the nanopattern structure were determined using the sectional height analysis command (Nanoscope 5.30r3sr3) by manually measuring the lateral diameters and vertical heights of 3 - 5 different spots on each sample (Figure 46). Due to the viscosity of the PDMS solution, the dimensions of the PDMS nanopattern were smaller than the hot embossed nanopatterned PMMA substrates (Table 6).

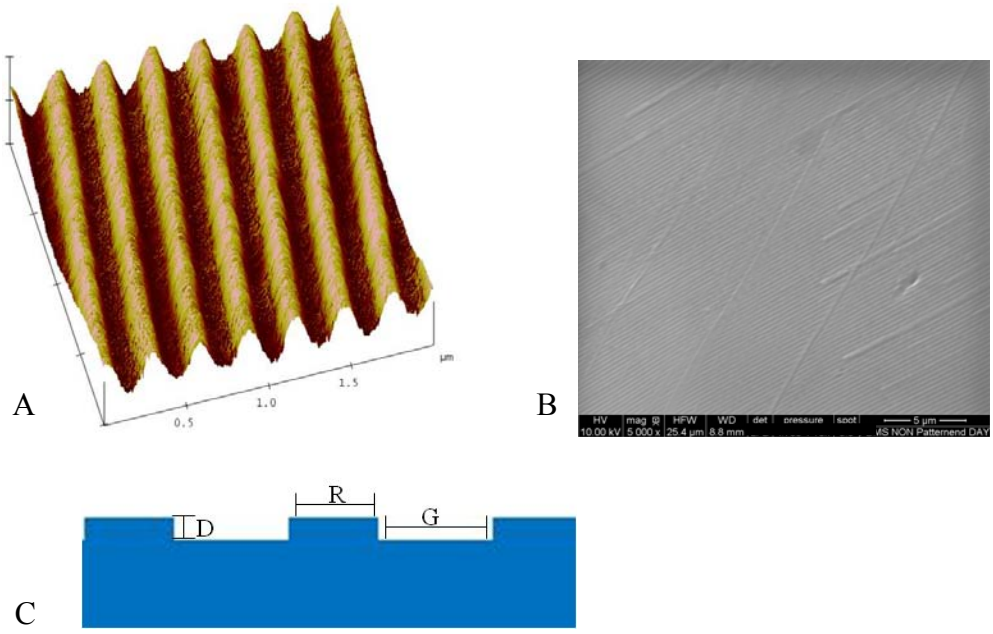

Figure 46. (A) AFM of patterned PDMS substrate. (B) SEM of patterned PDMS substrate. (C) Schematic of patterned dimensions; "D" refers to depth, "R" refers to width of ridge, and "G" refers to width of groove.

Table 7. Dimensions of nanopatterned substrates. PDMS dimension are reported as mean ± standard deviation.

	Depth (nm)	Width of ridge (nm)	Width of groove (nm)
PMMA	200	277	277
PDMS	15 ± 2	117 ± 11	170 ± 16

8.2.3 Scanning Electron Microscopy

Scanning electron microscopy (SEM) was utilized to image the cells and brain tissue on the substrate surface. In particular, the Environmental SEM Quanta FEG 450 (FEI Company, Hillsboro, OR) was used at an operating high voltage of 10kV and pressure of 5.5 Torr. On day seven, samples were fixed in a 4% paraformaldehyde solution for 30 minutes at room temperature (RT). Following three rinses in 1×PBS, the samples were then washed in distilled water in order to remove salt crystals from the PBS.

8.2.4 Brain Slice Culture

The Wayne State University Institutional Animal Care and Use Committee approved experimental protocols described herein. Sprague-Dawley postnatal five day old pups were used for brain slicing. Pups were euthanized by decapitation. Brains were removed and placed in ice cold dissection media made up of Hank's Buffered Sodium Solution (HBSS) containing 1% penicillin-streptomycin and 600M μL-Glutamine. Following which, the dissected brains were coated in a 4% agarose gel for slicing. Whole brain tissue slices, at a thickness of 400nm, were made using a Leica VT 10005 Vibrotome Line (Leica, Buffalo Grove, IL). Brain slices were grown on Millipore Millicell cell culture inserts (Millipore, Billerica, MA(Smeal et al., 2007). Brain tissue slices were maintained in 50% minimal essential medium (MEM), 1% penicillin-streptomycin, 25% Fetal Bovine Serum (FBS) and 25% dissection media. The tissues were housed in a humidified incubator with the following setting conditions: 90% humidity, 5% CO_2

and 37.8°C. Culture media was changed every two days. PDMS pins were placed on the brain tissue slices (Figure 47) immediately after tissue slices were set in the cell culture inserts, with controls being tissue slices growing without PDMS pins.

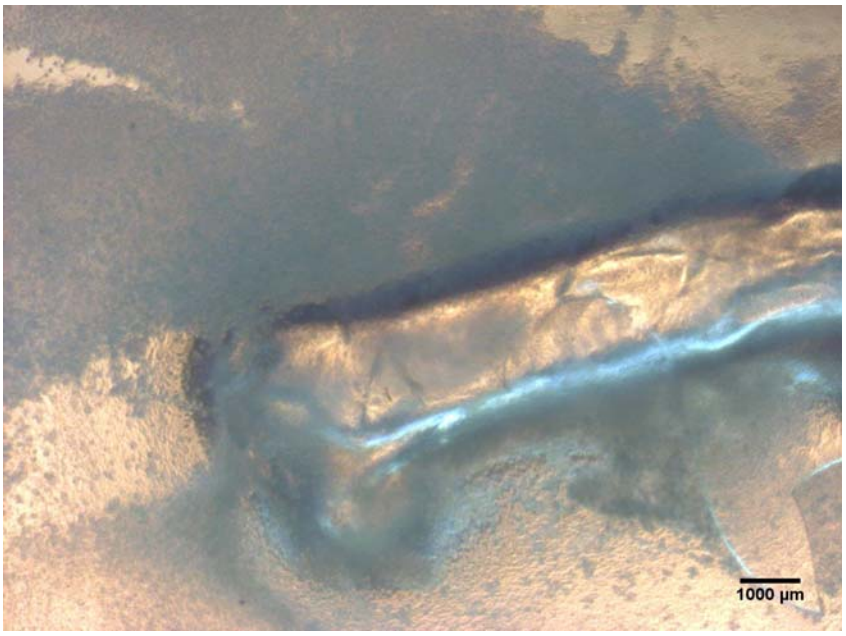

Figure 47. Phase contrast image of PDMS pin lying on top of a brain tissue slice. Image was taken on day seven of the nanopatterned PDMS pin.

8.2.5 Immunostaining Brain Slices

Brain slice tissues were stained with fluorescent antibodies in order to image astrocyte and cell nuclei attachment on the PDMS samples. At day seven, the cells were fixed in a 4% paraformaldehyde solution for 30 minutes at room temperature. Following three rinses in 1×PBS, the samples were incubated in a 5% blocking buffer (4.9% gelatin, 94% 1×PBS, 1% of 2% Na azide, and 0.1% triton) for one hour at room temperature (RT). Astrocyte specific primary antibody, GFAP (Millipore, Billerica, MA) was used to stain astrocytes (1:100 in blocking buffer) overnight at 4°C. Brain sections were washed with 1×PBS three times before adding the secondary antibody for the astrocytes. GFAP Alexa Fluor 555 goat anti-rabbit IgG

(Invitrogen, Carlsbad,CA) secondary antibody (1:100 in blocking buffer) was used for one and a half hours in the dark at RT. Samples were washed three times with 1×PBS. The samples were mounted on glass slides using ProLong Anti-Fade Gold with DAPI reagent (Invitrogen, Carlsbad, CA) to stain the cell nuclei. Samples were viewed under a Zeiss LSM-510 META NLO Laser Scanning Confocal Microscope (Carl Zeiss Inc).

8.2.6 Real Time PCR

Real time PCR was used to measure gene expression from samples relative to the control. The total RNA from the tissues was extracted on days one and seven with Trizol (Invitrogen, Carlsbad, CA) following the manufacturer's protocol. The RNA was then purified using RNeasy MinElute Cleanup kit and RNase-Free DNase kit (Qiagen, Valencia, CA). The RNA concentration and purity was determined using a NanoDrop (Thermo Scientific, Wilmington, DE). Reverse transcriptase using the random primers converted the mRNA to a cDNA template using a thermal cycler (Mastercycler Gradient, Eppendorf, Hauppauge, NY). For PCR analysis, we used cDNA equivalent to 40ng of total RNA. Specific primer pairs (Table 7) for astrocyte activation, glial fibrillary acidic protein (GFAP) and cytokines for inflammation, transforming growth factor beta 1(TGFβ1), interleukin 1 beta (IL1β) and tumor necrosis factor alpha (TNFα) were used. As an internal control, we used the house-keeping gene glyceraldehyde-3-phosphate dehydrogenase (GAPDH). The PCR master mix included 1×SYBR® Green (Applied Biosystems, Foster City, CA), and forward and reverse primers (0.4μM each). cDNA templates and master mix were read in a 96-well optical plate using a 7500 Fast Real-Time PCR System (Applied Biosystems, Foster City, CA). The following profile was used: 50°C for 2 min, 95°C for 10 min, and 40 cycles of 95°C for 15s and 60°C for 1 minute. Threshold cycle (Ct) values for each sample and primer pair were obtained and analyzed with the delta-delta (ΔΔ) Ct method

(Livak and Schmittgen, 2001; Schmittgen and Livak, 2008) in order to calculate the fold change (R) in each target gene. The following equations were used:

$\Delta Ct = Ct_{sample} - Ct_{GAPDH}$

$\Delta\Delta Ct = \Delta Ct_{test\ surface} - \Delta Ct_{control\ surface}$

$R = 2^{-\Delta\Delta Ct}$

Table 8. Primer sequences for real-time PCR used in nanopatterned PDMS studies.

Cells	Category	Gene	Primer Sequence
Organotypic Brain Slice Tissue Culture	Housekeeping gene	GAPDH	5'-TGGCCTTCCGTGTTCCTACC-3' (F)
			5'-AGCCCAGGATGCCCTTTAGTG-3' (R)
	Activation gene	GFAP	5'-GTTGTGTTCAAGCAGCCTGG-3' (F)
			5'-CCAGTGAGTAAAGGTGACAG-3' (R)
	Cytokine	TGF-β1	5'- ACCAACTACTGCTTCAGCTC -3'(F)
			5'- TGTTGGTTGTAGAGGGCAAG -3' (R)
	Cytokine	IL1β	5'-TCCATGAGCTTTGTACAAGG-3' (F)
			5'–GGTGCTGATGTACCAGTTGG-3' (R)
	Cytokine	TNFα	5'-AAATGGGCTCCCTCTCATCA-3' (F)
			5'-AGCCTTGTCCCTTGAAGAGA-3' (R)

8.2.7 Statistical Analysis

All of the data is presented as a mean ± standard error of the mean. Experiments were performed in triplicates and repeated three independent times. PASW software (version 18.0) was utilized for statistical analysis. A nonparametric statistical analysis was used to test for statistically significant differences between the different material groups over time for the

RTPCR. Parametric statistical methods could not be completed due to insufficient power from a small sample size, mean values were either not normally distributed or the variances of the data were not heterogeneous. The exact tests were conducted in order to be able to make reliable inferences by computing exact p values for a very wide class of hypothesis tests, including one-, two-, and K sample tests, tests for unordered and ordered categorical data, and tests for measures of association.

8.3 Results

8.3.1 Immunostaining

Immunostaining of astrocytes and cell nuclei revealed cells grown on the nanopatterend PDMS pins grew in one general direction, while cells growing on the non-patterned PDMS pins grew in random orientation (Figure 48). The nuclei of cells' growing on the nanopatterned pins were elongated in the same direction as the astrocyte processes. The nuclei of cells' grown on the non-patterned pins were rounder and not following any particular or uniform direction. Moreover, the cell distribution did not seem to differ between both material surfaces, there were the same amount of cells on both nanopatterned and non-patterned pins.

A

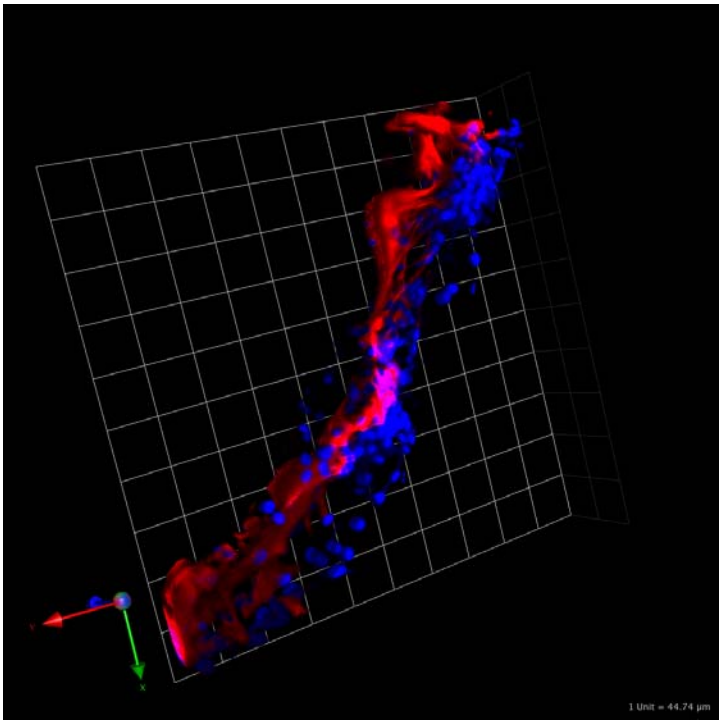

B

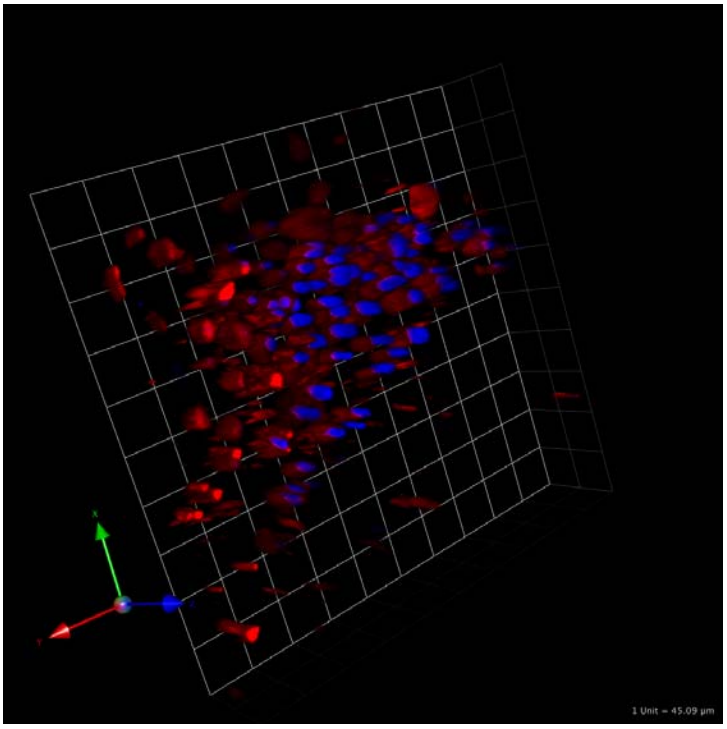

Figure 48. Confocal images at day seven of GFAP stained astrocytes and DAPI stained cell nuclei growing on (A) patterned PDMS pin (B) non-patterned PDMS pin.

8.3.2 SEM

SEM images confirmed that the cells growing on the nanopatterned surface were aligning with the pattern (Figure 49). As can be seen from the SEM images, cells on the nanopatterned surfaces were elongated along the pattern's direction. However, cells growing on the non-patterend surface were randomly oriented on the surface.

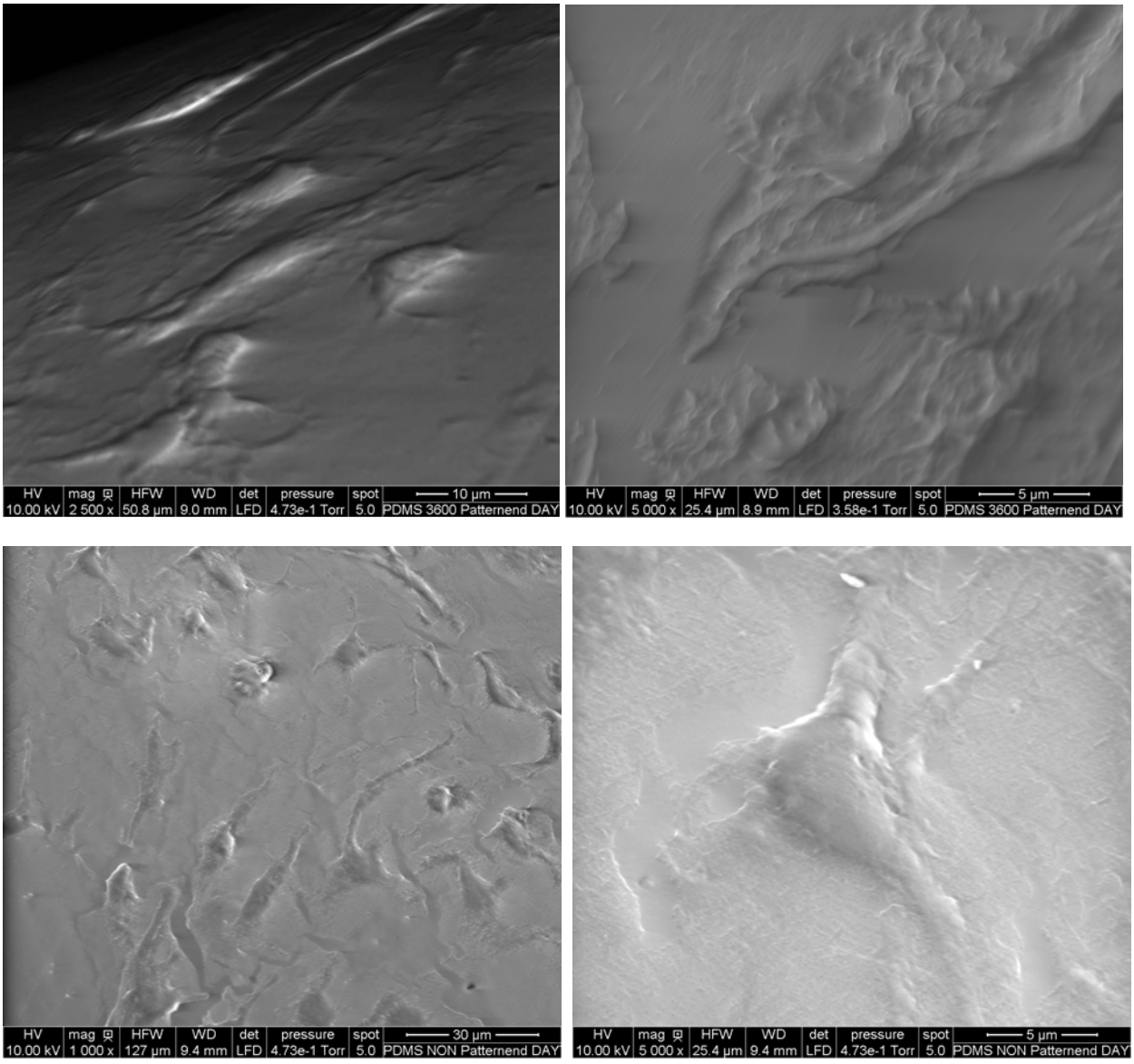

Figure 49. SEM images at day seven of cells growing on (A) nanopatterned PDMS pin. Cells are growing along the nanopaterned lines. (B) non-patterned PDMS pin.

8.3.3 Relative Gene Expression

Cells cultured with non-patterned PDMS pins had significantly lower ($p<0.01$) GFAP relative gene expression on day one compared to the control (Figure 50). There was not any statistical significance found with GFAP expression from brain slice cells cultured with the nanopatterned PDMS pins on either day. However, it is important to note that cells cultured with nanopatterned PDMS pins had a decrease in GFAP gene expression over time and levels were below the control on both days. Meanwhile, cells cultured with the non-patterned pins had an increase over time and resulted in GFAP relative gene expression a little higher than the control on day seven.

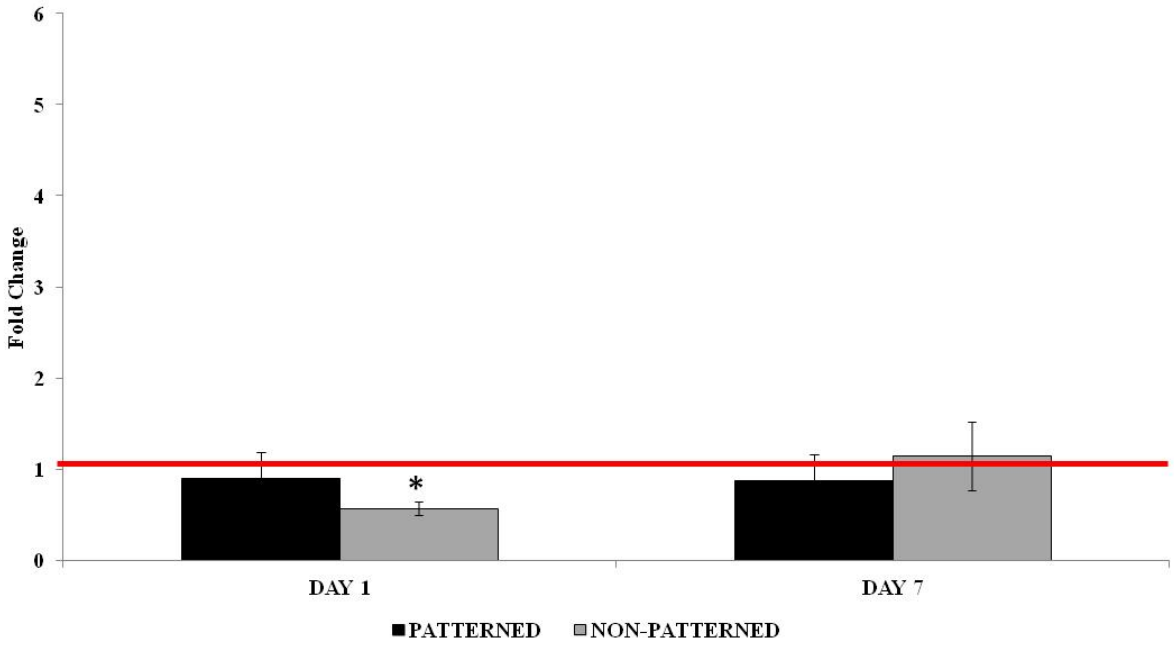

Figure 50. RTPCR GFAP relative gene expression. The control is represented as the red line. *$p<0.01$ data compared to control on day one.

There were no significant differences found between patterned and non-patterned samples on either day with IL1β relative gene expression (Figure 51). Nevertheless, it was observed that brain slice cells cultured with both patterned and non-patterned PDMS pins had

IL1β relative gene expression higher than the control on both days. Additionally, it is notable that cells cultured with patterned PDMS pins showed a slight decrease in IL1β relative gene expression over time, while those with non-patterned pins showed a slight increase over time.

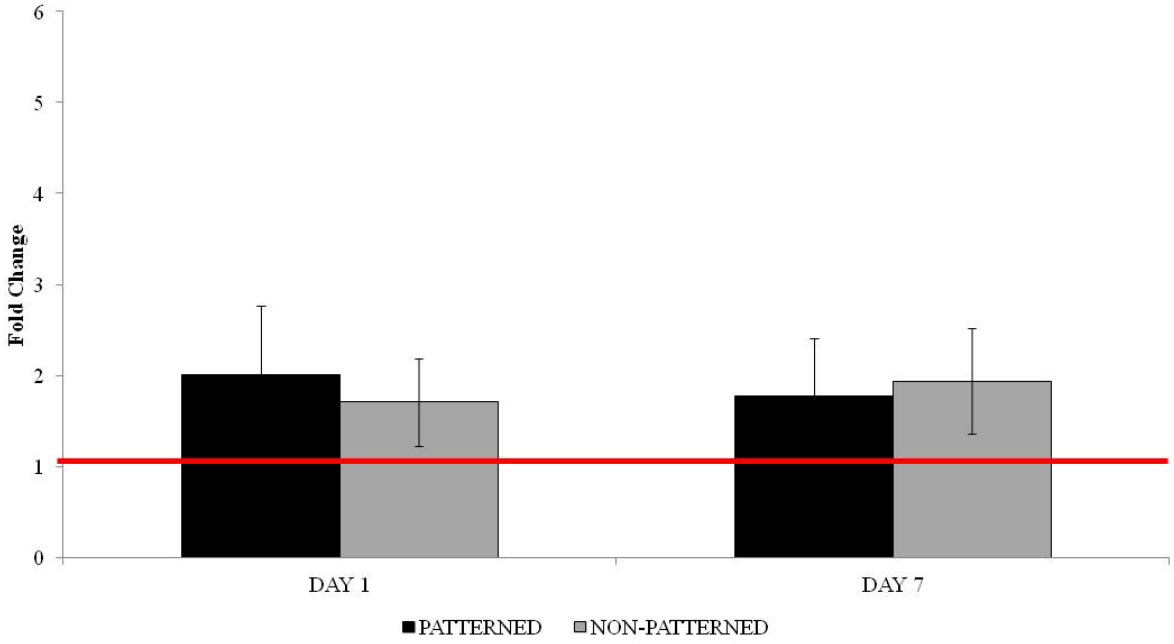

Figure 51. RTPCR IL1β relative gene expression. The control is represented as the red line.

Brain slice cells cultured with patterned PDMS pins had significantly lower ($p<0.01$) TNFα relative gene expression compared to the control on day one (Figure 52). Conversely, cells cultured with non-patterned PDMS had significantly higher ($p<0.01$) TNFα relative gene expression compared to the control on day one. Both materials showed a decrease of TNFα relative gene expression over time, with patterned having lower TNFα relative gene expression compared to non-patterned on both days.

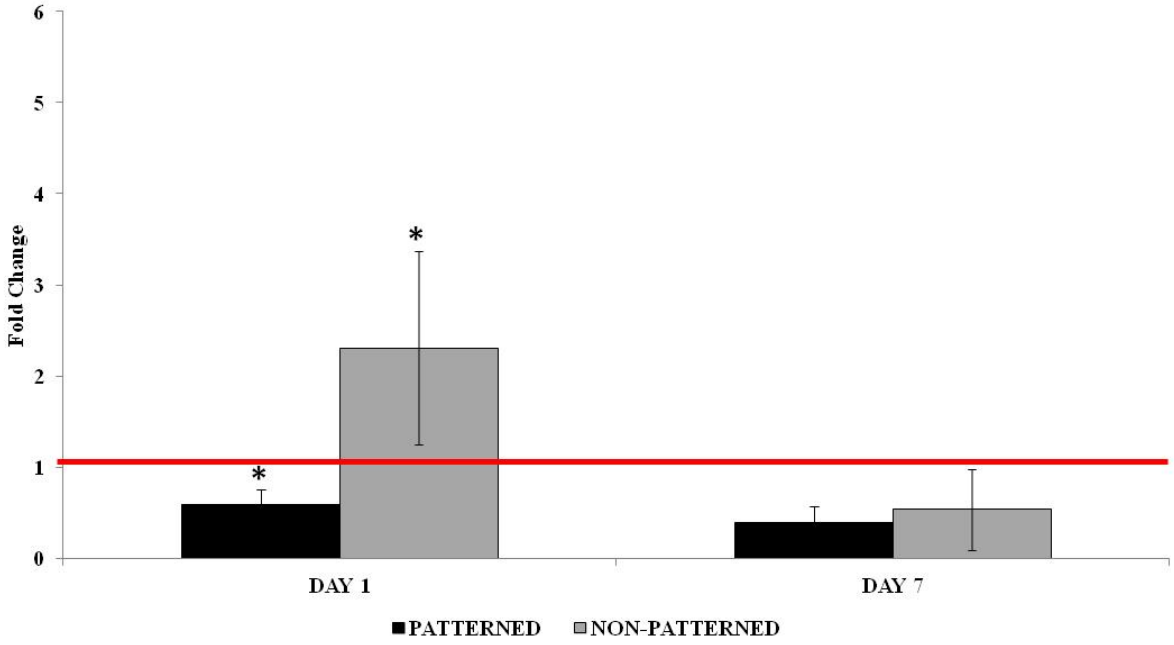

Figure 52. RTPCR of TNFα relative gene expression. The control is represented as the red line. *p<0.05 data compared to control at day one.

There was no significance found between materials and days with the TGFβ1 relative gene expression (Figure 53). However, it is important to note that the cells cultured with the non-patterned pins had higher TGFβ1 relative gene expression levels compared to cells cultured with the nanopatterned pins on both days. Moreover, brain slice cells cultured with both materials showed an increase of TGFβ1 relative gene expression over time.

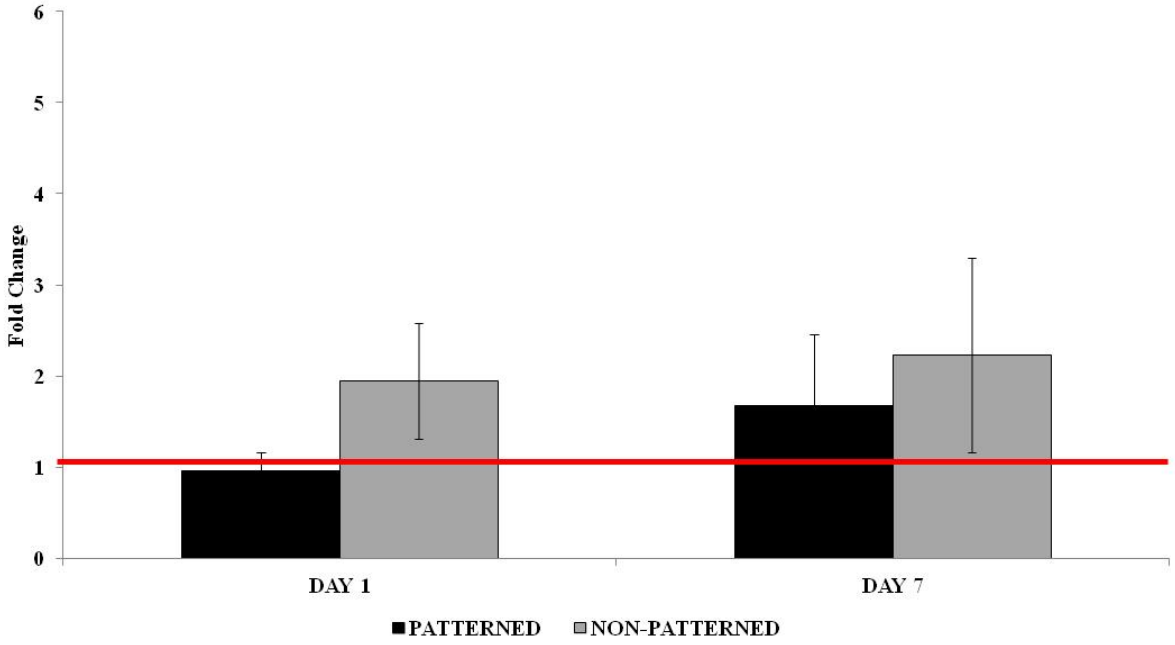

Figure 53. RTPCR of TGFβ1 relative gene expression. The control is represented as the red line.

8.4 Discussion

Nanofabrication allows for better understanding of cell behavior by mimicking the nano-world around the cell created by the nanotopographies of the ECM and the nanochemistry that composes the cell membrane (Blattler et al., 2006). It is the ability of a nanomaterial to mimic the roughness of natural tissue that is so interesting when designing optimal implants for the central nervous tissue. The mechanism involved with the cellular response to a nanopatterned surface is not well understood. It is thought that the effects of the surface topography either directly influence the cell response, or indirectly effect the cell responses through the affects they have on the adsorption of proteins (Kriparamanan et al., 2006). The confocal and SEM results of the present study give evidence that nanotopography influences cell response, both morphologically and molecularly. It was shown that topography as small as 120nm wide ridges

with a depth of 20nm were sensitive enough to control cell alignment and consequently alter gene expression.

Organotypic tissue slices cultured with nanopatterned PDMS pins demonstrated that the cells grew along the nanopattern, while non-patterned PDMS pins had randomly oriented cells along the pin. The aligned morphology of the cells was suspected to cause the differences in the gene expression observed between patterned and non-patterned pins. Topography has been shown to influence cell behavior (Bruder et al., 2007; Mieszawska and Kaplan, 2010). Studies done by Shain et al found that astrocytes prefer to grow and adhere onto patterned surfaces of varying dimensions over smooth silicon surfaces *in vitro* (Kriparamanan et al., 2006; Szarowski et al., 2003). Moreover, Yim et al studied effects of human mesenchymal stem cells grown on nanopatterned PDMS substrates (Yim et al., 2007). They found that nanotopography enhanced the upregulation of neuronal marker expression, compared to biochemical cues and non-patterned surfaces (Yim et al., 2007). The same study demonstrated that nanotopography had a significant effect on directing differentiation of adult stem cells (Yim et al., 2007). Gomez et al examined microchannel-patterned PDMS in order to assess the rate of axon initiation and overall axon length of embryonic hippocampal neurons (Gomez et al., 2007; Gomez and Schmidt, 2007). They found that PDMS microtopography was a crucial factor leading to 68% increase in axon initiation (Gomez et al., 2007; Gomez and Schmidt, 2007).

Typical inflammatory response to brain injury includes activated microglia at the site of injury. Activated microglia rapidly respond to protect neural cells by releasing trophic and anti-inflammatory factors such as TGFβ1, IL1β and TNFα (Parekkadan et al., 2008). One of the first effectors to be produced is IL-1β. Herx et al showed activated microglia produce IL-1β within

15 minutes following a cortical injury (Herx et al., 2000; Herx and Yong, 2001; Liberto et al., 2004). Microglia synthesize and release TGFβ1 following injury, along with proinflammatory interleukin-1 and tumor necrosis factor. TGF-β1 is immediately released after injury, controlling the inflammatory and neuronal response (Berdichevsky et al., 2010; Hermanns et al., 2006; Klapka and Muller, 2006). TGFβ1 is an astrocyte derived cytokine that works as a neuroprotective in the brain by increasing extracellular matrix protein production, consequently resulting in the formation of the glial scar (Farina et al., 2007; Rao et al., 2012). TNFα is a proinflammatory cytokine both astrocytes and microglia produce and act upon in response to specific signals (Downen et al., 1999; John et al., 2003; Liberto et al., 2004; Malipiero et al., 1990). Studies have shown activated microglia produce 95 times more TNFα than activated astrocytes (Liberto et al., 2004; Malipiero et al., 1990). Like IL-1β, TNFα is released at the beginning of reactive astrogliosis and functions to repair damage in the CNS, however it has been shown to be directly cytotoxic to neurons (Downen et al., 1999; John et al., 2003).

Recent work by Herx et al illustrated the importance of IL-1β to the initiation of reactive astrogliosis (Herx and Yong, 2001; John et al., 2003). This group demonstrated the presence of IL-1β resulted in an up-regulation of GFAP expression in astrocytes (Herx and Yong, 2001; John et al., 2003). Likewise, we found an analogous increase in IL-1β and GFAP with cells on the non-patterned PDMS pins, which demonstrates the documents inflammatory response. To the contrary, cells on the nanopatterned surface had a decrease in both IL-1β and GFAP gene expression over time. This evidence suggests a decrease in the inflammatory response, thus advocating biocompatibility of the nanopatterned pins.

Gene expression of GFAP decreased on nanopatterned surfaces over time, while increasing on non-patterned surfaces over time. GFAP relative gene expression remained close

to control values on both days and both samples. These results indicate nanopatterning did slightly improve the biocompatibility of the PDMS pins. Moreover, TGFβ1 gene expression increased over time with both patterned and non-patterned samples. However, TGFβ1 levels were lower from brain tissue slices cultured with nanopatterened pins compared to the non-patterned pins. In fact, on day one in culture, TGFβ1 gene expression with nanopatterned pins was lower than the control. These results indicate that the nanopatterning inhibits TGFβ1 expression. A study done by Logan et al showed inhibition of TGFβ1 prevents reactive astrocytes from forming a glial scar around the injury site, and a down-regulation of ECM molecules expression, such as laminin and fibronectin (John et al., 2003; Logan et al., 1994). Similarly, *in vitro* studies of TGFβ1 administration to primary astrocyte cultures revealed a down-regulation of several proinflammatory gene expression, such as TNFα (Dong and Benveniste, 2001; John et al., 2003; Shrikant and Benveniste, 1996; Smith and Hale, 1997). These studies also showed TGFβ1 induces the expression of multiple extracellular matrix molecules and cytoskeletal components thereby leading to the formation of a glial scar and inhibition of neuronal growth (Dong and Benveniste, 2001; Fok-Seang et al., 1998; John et al., 2003; Shrikant and Benveniste, 1996; Smith and Hale, 1997; Wyss-Coray et al., 2000). Results from this study suggest nanopatterning inhibits TGFβ1 expression, thereby preventing the cascade of events leading to glial scar formation.

Studies have revealed TNFα to be rapidly upregulated in injured or inflamed CNS animal models (John et al., 2003; Rostworowski et al., 1997; Taupin et al., 1993). This upregulation of TNFα was exhibited to be concurrent with the increase of GFAP in astrocytes which leads to glial scar formation (John et al., 2003; Rostworowski et al., 1997; Taupin et al., 1993). Results of this study are not in accord with previous findings depicting inflammation. In fact, results

from this study showed a decrease in TNFα over time with both nanopatterned and non-patterned PDMS pins. Moreover, it was observed that tissues cultured with the nanopatterned pins had lower TNFα levels compared to both the non-patterned and control samples. These results indicate that the nanopattern features inhibit TNFα gene expression which may simultaneously lead to the prevention of glial scar tissue formation.

Tissue cultures with the nanopatterned pins exhibited the typical acute neuroinflammatory response, which consists of a reduction of IL1β and TNFα levels over time and an increase in TGFβ1 levels over time. However, there was a decrease in GFAP levels over time, indicating the negative feedback mechanism had taken effect, astrocytes did not become reactive and the formation of a glial scar was avoided. On the other hand, tissue cultures with non-patterned PDMS pins had an increase of GFAP, IL-1β, and TGFβ1 over time, signifying the beginnings of a glial scar. It was observed that tissue cultures with nanopatterned PDMS pins had lower GFAP, IL1β, TNFα, and TGFβ1 relative gene expression compared to non-patterned PDMS by day seven. These results denote nanopatterning of the PDMS pins surface reduces the glial cells' inflammatory response, therefore indicating an improved biocompatibility.

8.5 Conclusions

The decreasing trend of GFAP, TNFα, IL-1β gene expression found from cells cultured with the nanopatterned PDMS pins indicates a reduction of inflammation. By day seven, all four markers tested were lower with nanopatterned pins compared to non-patterend pins. Results of this study confirm nanopatterning not only influences cell morphology, but molecularly as well. These results collectively indicate nanpatterning improves the biocompatibility of PDMS by reducing inflammatory markers such as GFAP, IL-1β, TGFβ1 and TNFα compared to the non-

patterned PDMS pins. Further investigation including neuron proximity, morphology and functionality will enhance our current findings.

CHAPTER 9

9.1 CONCLUSIONS

These studies have utilized a combination of *in vitro* techniques in order to assess the biocompatibility of biomaterials used for neural electrode fabrication and design. Initially, the astrocyte response was studied to compare the biocompatibility of silicon, platinum, PMMA and SU-8. It is well documented that reactive astrocytes are characterized by hypertrophy, hyperplasia, upregulation of GFAP, formation of filaments, enlarged, irregularly shaped nuclei, activated cell proliferation site production of a glial scar tissue rich in ECM proteins (Buffo et al., 2010; Gervasi et al., 2008; Laird et al., 2008; Polikov et al., 2006; Polikov et al., 2005). Therefore, these studies focused on examining these characteristics. Results indicate little to no antimony in the SU-8 formula used in this study, which is evident of the non-cytoxicity of SU-8. Moreover, there was at least 93% viability of cells on SU-8 for up to one week *in vitro*, the initial adhesion of cells was strongest on SU-8, the proliferation rates were steady and consistent with the control, the morphology of the nucleus was consistent with the control, and GFAP was lowest on SU-8 day seven. Overall, these observations suggest SU-8 to be biocompatible. Results determined the cellular characteristics, reactions and growth rates of astrocytes grown on PMMA resembled closely to that of cells grown on the control surface, thus confirming the biocompatibility of PMMA. Additionally, the astrocyte GFAP gene expressions of cells grown on PMMA were lower than the control, signifying a lack of astrocyte reactivity. Furthermore, it was shown astrocytes depict reactive characteristics when grown on platinum and silicon surfaces, thus rendering the need to find more biocompatible, conducting materials for neural electrode fabrication.

Based on the findings from the biomaterials study, it was decided to optimize PMMA by changing the surface characteristic of the material. Through the process of hot embossing, nanopatterns were placed on the surface in order to test the hypothesis that nanopattterning can improve the cellular response to the material. Results of this study agreed with current literature showing that topography effects protein and cell behavior. Nanopatterning increased the rate of protein adsorption, influenced cells to align along the direction of the pattern, inhibited the GFAP gene expression, and decreased the amount of cell adhesion compared to the non-patterned substrate. Moreover, it was determined that the size of the nanopattern induced particular protein and cell responses. Specifically, it was concluded that for the use in neural electrode fabrication and design, the 3600mm/gratings pattern feature sizes were optimal. The 3600 mm/gratings pattern depicted cell alignment along the nanopattern, less protein adsorption, less cell adhesion, proliferation and viability, inhibition of GFAP and MAP2k1 compared to all other substrates tested.

Results from the initial biomaterials study also indicated platinum was negatively affected the cells and may not be a suitable material for neural electrodes. This lead to pursuing studies with iridium oxide and platinum alloy wires for the glial scar assay. It is known that when compared by electrical properties, such as impedance and charge injection capacity, iridium oxide has its advantages with lower impedance and a higher charge injection capacity compared to platinum. These advantages would appear to make iridium oxide more favorable for neural electrode fabrication. However, results of this study demonstrate that although the electrical properties may be better, iridium oxide wires exhibited a more significant reactive response as compared to platinum alloy wires. Astrocytes cultured with platinum alloy wires had less GFAP gene expression, lower average GFAP intensity, and smaller glial scar thickness.

Collectively, these results indicated that platinum alloy wires were more biocompatible than the iridium oxide wires.

Results from the nanopatterning PMMA study prompted a more thorough investigation of the nanopatterning effects using an organotypic brain slice model. PDMS was utilized as the substrate due to its optimal physical properties. PDMS is highly viscoelastic, which made it possible to roll after it was nanopatterned. Confocal and SEM imaging illustrated cells from the brain tissue slices were aligned along the nanopattern on the PDMS pins. Decreases in several inflammatory markers (GFAP, TNFα, IL-1β) determined from gene expression analysis, was shown with the nanopatterned PDMS pins. By day seven, all four markers tested were lower with nanopatterned pins compared to non-patterend pins. Results of this study confirm nanopatterning not only influences cell morphology, but alters molecular cascades within the cells as well. These results collectively indicate nanpatterning improves the biocompatibility of PDMS by reducing inflammatory markers such as GFAP, IL-1β, TGFβ1 and TNFα compared to the non-patterned PDMS pins.

The results of these studies provide essential information for the neural electrode research community. There is a lack of information available in the scientific community on acceptable and effective materials for neural electrode fabrication. The results of the presented studies provide more information which could lead to classifying guidelines to create biocompatible neural electrode materials.

CHAPTER 10

10.1 FUTURE WORK

Based on the results of these studies, there are several possible directions for future investigations.

1. The present study demonstrated the importance of biocompatibility testing of materials used in neural electrode fabrication. These studies mainly focused on the astrocyte response to the materials. Future studies focusing on the microglia, oligodendrocyte and neuron response to materials is imperative to fully grasp the biocompatibility of the materials used in neural electrodes. Research has shown different cells have various responses to materials and topographies, therefore it is imperative to assure all brain cells are biocompatible with materials used in neural electrode fabrication.

- Microglia reactivity assessment based on cell morphology, proliferation, viability, adhesion, and gene expression of inflammatory cytokines should be studied. *In vitro* investigation of a microglia cell line grown on non-patterned biomaterials and nanopatterned biomaterials is required to fully understand the inflammatory response to these materials.

- Neuron proximity, morphology and functionality should be conducted to determine if the neural electrode materials attract and excite neurons. Preliminary *in vitro* studies utilizing a neuronal cell line in order to examine the neuron

morphology, adhesion, viability, and proximity to recording sites on the material are necessary.

- Mixed cell cultures consisting of neurons and oligodendrocytes should be grown on the biomaterials. In which case, oligodendrocyte proximity to neurons and functionality to provide ample myelin sheath around axons will be examined.

2. Future studies employing either the glial assay or the organotypic brain slice model from the current studies will enhance the understanding of the physiological and functional neuronal response to the material in an *in vitro* setting. Neuron electrophysiology is a vital need for final assessment of the biomaterials. Therefore, these studies should incorporate techniques such as the patch clamp in order to assess the performance of the neurons with the electrode materials under investigation.

3. The nanopatterning used in these studies proved to encourage cell alignment and decrease glial cell reactivity. Additional exploration of surface modifications based on the findings from these studies may continue to improve glial cells biocompatibility and enhance neuron functionality. Further investigation on various nanopattern geometries based on the feature sizes presented in these studies may demonstrate further increases in biocompatibility of biomaterials.

4. Chronic studies evaluating glial scarring in an *in vivo* setting will add to the results of these studies. *In vitro* studies have time limitations due to cellular confluence and the natural process of apoptosis that occurs once confluence is surpassed. Therefore, in order to assess the glial scarring occurring in chronically implanted neural electrodes, an *in vivo*

model should be utilized to test novel and optimized biomaterials which have passed *in vitro* biocompatibility testing.

5. These studies evaluated numerous materials used in all aspects of neural electrode fabrication; materials employed for the conducting surface, as well as material used as backbone support and insulation. Based on these findings, a neural electrode prototype design utilizing these materials and topographies may proceed.

REFERENCES

2003. Fundamental Neuroscience, in: Squire, B., McConnell, Roberts, Spitzer, Zigmond (Ed.), Second Edition ed. Academic Press.

Achyuta, A.K., Polikov, V.S., White, A.J., Lewis, H.G., Murthy, S.K., 2010. Biocompatibility assessment of insulating silicone polymer coatings using an in vitro glial scar assay. Macromol Biosci 10, 872-880.

Agnew, W.F., Yuen, T.G., McCreery, D.B., 1983. Morphologic changes after prolonged electrical stimulation of the cat's cortex at defined charge densities. Exp Neurol 79, 397-411.

Agnew, W.F., Yuen, T.G., McCreery, D.B., Bullara, L.A., 1986. Histopathologic evaluation of prolonged intracortical electrical stimulation. Exp Neurol 92, 162-185.

Alaerts, J.A., De Cupere, V.M., Moser, S., Van den Bosh de Aguilar, P., Rouxhet, P.G., 2001. Surface characterization of poly(methyl methacrylate) microgrooved for contact guidance of mammalian cells. Biomaterials 22, 1635-1642.

Asparuhova, M.B., Gelman, L., Chiquet, M., 2009. Role of the actin cytoskeleton in tuning cellular responses to external mechanical stress. Scand J Med Sci Sports 19, 490-499.

Avvisato, C.L., Yang, X., Shah, S., Hoxter, B., Li, W., Gaynor, R., Pestell, R., Tozeren, A., Byers, S.W., 2007. Mechanical force modulates global gene expression and beta-catenin signaling in colon cancer cells. J Cell Sci 120, 2672-2682.

Berdichevsky, Y., Sabolek, H., Levine, J.B., Staley, K.J., Yarmush, M.L., 2009. Microfluidics and multielectrode array-compatible organotypic slice culture method. J Neurosci Methods 178, 59-64.

Berdichevsky, Y., Staley, K.J., Yarmush, M.L., 2010. Building and manipulating neural pathways with microfluidics. Lab Chip 10, 999-1004.

Bhandari, R., Negi, S., Rieth, L., Solzbacher, F., 2010. A Wafer-Scale Etching Technique for High Aspect Ratio Implantable MEMS Structures. Sens Actuators A Phys 162, 130-136.

Bhushan, B., 2008. Nanotribology and nanomechanics in nano/biotechnology. Philos Transact A Math Phys Eng Sci 366, 1499-1537.

Biran, R., Martin, D.C., Tresco, P.A., 2005. Neuronal cell loss accompanies the brain tissue response to chronically implanted silicon microelectrode arrays. Exp Neurol 195, 115-126.

Blattler, T., Huwiler, C., Ochsner, M., Stadler, B., Solak, H., Voros, J., Grandin, H.M., 2006. Nanopatterns with biological functions. J Nanosci Nanotechnol 6, 2237-2264.

Bruce Alberts, A.J., Julian Lewis, Martin Raff, Keith Roberts, Peter Walter 2008. Molecular Biology of the Cell, Fifth Edition ed. Garland Science, Taylor & Francis Group, New York.

Bruder, J.M., Lee, A.P., Hoffman-Kim, D., 2007. Biomimetic materials replicating Schwann cell topography enhance neuronal adhesion and neurite alignment in vitro. J Biomater Sci Polym Ed 18, 967-982.

Brunetti V, M.G., Rizzello L, Sorce B, Sabella S, Cingolani R, Pompa PP., 2010. Neurons sense nanoscale roughness with nanometer sensitivity. Proc Natl Acad Sci U S A 107, 6264-6269.

Buffo, A., Rolando, C., Ceruti, S., 2010. Astrocytes in the damaged brain: molecular and cellular insights into their reactive response and healing potential. Biochem Pharmacol 79, 77-89.

Bullara, L.A., McCreery, D.B., Yuen, T.G., Agnew, W.F., 1983. A microelectrode for delivery of defined charge densities. J Neurosci Methods 9, 15-21.

Burton, Z., Bhushan, B., 2005. Hydrophobicity, adhesion, and friction properties of nanopatterned polymers and scale dependence for micro- and nanoelectromechanical systems. Nano Lett 5, 1607-1613.

Chiquet, M., Renedo, A.S., Huber, F., Fluck, M., 2003. How do fibroblasts translate mechanical signals into changes in extracellular matrix production? Matrix Biol 22, 73-80.

Choi, J.H., Kim, Y.M., Park, Y.W., Park, T.H., Dong, K.Y., Ju, B.K., 2009. Hydrophobic nanopatterning on a flexible gas barrier film by using a poly(dimethylsiloxane) elastomer. Nanotechnology 20, 135303.

Chung, S., Sudo, R., Vickerman, V., Zervantonakis, I.K., Kamm, R.D., 2010. Microfluidic platforms for studies of angiogenesis, cell migration, and cell-cell interactions. Sixth International Bio-Fluid Mechanics Symposium and Workshop March 28-30, 2008 Pasadena, California. Ann Biomed Eng 38, 1164-1177.

Chung, S., Sudo, R., Zervantonakis, I.K., Rimchala, T., Kamm, R.D., 2009. Surface-treatment-induced three-dimensional capillary morphogenesis in a microfluidic platform. Adv Mater 21, 4863-4867.

Cogan, S.F., 2008. Neural stimulation and recording electrodes. Annu Rev Biomed Eng 10, 275-309.

Cogan, S.F., Ehrlich, J., Plante, T.D., Gingerich, M.D., Shire, D.B., 2010. Contribution of oxygen reduction to charge injection on platinum and sputtered iridium oxide neural stimulation electrodes. IEEE Trans Biomed Eng 57, 2313-2321.

Cogan, S.F., Ehrlich, J., Plante, T.D., Smirnov, A., Shire, D.B., Gingerich, M., Rizzo, J.F., 2009. Sputtered iridium oxide films for neural stimulation electrodes. J Biomed Mater Res B Appl Biomater 89, 353-361.

Cogan, S.F., Guzelian, A.A., Agnew, W.F., Yuen, T.G., McCreery, D.B., 2004a. Over-pulsing degrades activated iridium oxide films used for intracortical neural stimulation. J Neurosci Methods 137, 141-150.

Cogan, S.F., Plante, T.D., Ehrlich, J., 2004b. Sputtered iridium oxide films (SIROFs) for low-impedance neural stimulation and recording electrodes. Conf Proc IEEE Eng Med Biol Soc 6, 4153-4156.

Cogan, S.F., Troyk, P.R., Ehrlich, J., Gasbarro, C.M., Plante, T.D., 2007. The influence of electrolyte composition on the in vitro charge-injection limits of activated iridium oxide (AIROF) stimulation electrodes. J Neural Eng 4, 79-86.

Cogan, S.F., Troyk, P.R., Ehrlich, J., Plante, T.D., 2005. In vitro comparison of the charge-injection limits of activated iridium oxide (AIROF) and platinum-iridium microelectrodes. IEEE Trans Biomed Eng 52, 1612-1614.

Cogan, S.F., Troyk, P.R., Ehrlich, J., Plante, T.D., Detlefsen, D.E., 2006. Potential-biased, asymmetric waveforms for charge-injection with activated iridium oxide (AIROF) neural stimulation electrodes. IEEE Trans Biomed Eng 53, 327-332.

Curtis, A., 2005. The potential for the use of nanofeaturing in medical devices. Expert Rev Med Devices 2, 293-301.

Curtis, A.S., Gadegaard, N., Dalby, M.J., Riehle, M.O., Wilkinson, C.D., Aitchison, G., 2004. Cells react to nanoscale order and symmetry in their surroundings. IEEE Trans Nanobioscience 3, 61-65.

Dalby, M.J., Pasqui, D., Affrossman, S., 2004. Cell response to nano-islands produced by polymer demixing: a brief review. IEE Proc Nanobiotechnol 151, 53-61.

Das, S.K., Chung, S., Zervantonakis, I., Atnafu, J., Kamm, R.D., 2008. A microfluidic platform for studying the effects of small temperature gradients in an incubator environment. Biomicrofluidics 2, 34106.

David C Duffy, O.J.A.S., Scott T Brittain and George M Whitesides, 1999. Rapid prototyping of microfluidic switches in poly(dimethyl siloxane) and their actuation by electro-osmotic flow. Journal of Micromechanics and Microengineering 9.

De Boeck, M., Lombaert, N., De Backer, S., Finsy, R., Lison, D., Kirsch-Volders, M., 2003. In vitro genotoxic effects of different combinations of cobalt and metallic carbide particles. Mutagenesis 18, 177-186.

Ding, H., Millet, L.J., Gillette, M.U., Popescu, G., 2010. Actin-driven cell dynamics probed by Fourier transform light scattering. Biomed Opt Express 1, 260-267.

Dong, Y., Benveniste, E.N., 2001. Immune function of astrocytes. Glia 36, 180-190.

Dow, K.E., Wang, W., 1998. Cell biology of astrocyte proteoglycans. Cell Mol Life Sci 54, 567-581.

Downen, M., Amaral, T.D., Hua, L.L., Zhao, M.L., Lee, S.C., 1999. Neuronal death in cytokine-activated primary human brain cell culture: role of tumor necrosis factor-alpha. Glia 28, 114-127.

Duffy, H.S., John, G.R., Lee, S.C., Brosnan, C.F., Spray, D.C., 2000. Reciprocal regulation of the junctional proteins claudin-1 and connexin43 by interleukin-1beta in primary human fetal astrocytes. J Neurosci 20, RC114.

Dupont-Gillain, C.C., Alaerts, J.A., Dewez, J.L., Rouxhet, P.G., 2004. Patterned layers of adsorbed extracellular matrix proteins: influence on mammalian cell adhesion. Biomed Mater Eng 14, 281-291.

Elfar, S.D., Cottaris, N.P., Iezzi, R., Abrams, G.W., 2009. A cortical (V1) neurophysiological recording model for assessing the efficacy of retinal visual prostheses. J Neurosci Methods 180, 195-207.

Ereifej, E.S., Khan, S., Newaz, G., Zhang, J., Auner, G.W., VandeVord, P.J., 2011. Characterization of astrocyte reactivity and gene expression on biomaterials for neural electrodes. J Biomed Mater Res A 99, 141-150.

Eric J. Nestler, S.E.H., Robert C. Malenka. , 2001. Molecular neuropharmacology: a foundation for clinical neuroscience, 2nd ed. ed. McGraw-Hill Medical, New York.

Farina, C., Aloisi, F., Meinl, E., 2007. Astrocytes are active players in cerebral innate immunity. Trends Immunol 28, 138-145.

Fitch, M.T., Silver, J., 2008. CNS injury, glial scars, and inflammation: Inhibitory extracellular matrices and regeneration failure. Exp Neurol 209, 294-301.

Fok-Seang, J., DiProspero, N.A., Meiners, S., Muir, E., Fawcett, J.W., 1998. Cytokine-induced changes in the ability of astrocytes to support migration of oligodendrocyte precursors and axon growth. Eur J Neurosci 10, 2400-2415.

Frampton, J.P., Hynd, M.R., Shuler, M.L., Shain, W., 2010. Effects of glial cells on electrode impedance recorded from neuralprosthetic devices in vitro. Ann Biomed Eng 38, 1031-1047.

Frazer, R.Q., Byron, R.T., Osborne, P.B., West, K.P., 2005. PMMA: an essential material in medicine and dentistry. J Long Term Eff Med Implants 15, 629-639.

Fujii, T., Masuda, N., Tamiya, S., Shima, M., Toda, E., Ito, D., Nakazawa, G., Matsukage, T., Ogata, N., Morino, Y., Tanabe, T., Ikari, Y., 2010. Angiographic evaluation of right upper-limb arterial anomalies: implications for transradial coronary interventions. J Invasive Cardiol 22, 536-540.

Gervasi, N.M., Kwok, J.C., Fawcett, J.W., 2008. Role of extracellular factors in axon regeneration in the CNS: implications for therapy. Regen Med 3, 907-923.

Glass, C.K., Saijo, K., Winner, B., Marchetto, M.C., Gage, F.H., 2010. Mechanisms underlying inflammation in neurodegeneration. Cell 140, 918-934.

Gobbels, K., Kuenzel, T., van Ooyen, A., Baumgartner, W., Schnakenberg, U., Braunig, P., 2010. Neuronal cell growth on iridium oxide. Biomaterials 31, 1055-1067.

Gomez, N., Lu, Y., Chen, S., Schmidt, C.E., 2007. Immobilized nerve growth factor and microtopography have distinct effects on polarization versus axon elongation in hippocampal cells in culture. Biomaterials 28, 271-284.

Gomez, N., Schmidt, C.E., 2007. Nerve growth factor-immobilized polypyrrole: bioactive electrically conducting polymer for enhanced neurite extension. J Biomed Mater Res A 81, 135-149.

Griffith, R.W., Humphrey, D.R., 2006. Long-term gliosis around chronically implanted platinum electrodes in the Rhesus macaque motor cortex. Neurosci Lett 406, 81-86.

Grill, W.M., Norman, S.E., Bellamkonda, R.V., 2009. Implanted neural interfaces: biochallenges and engineered solutions. Annu Rev Biomed Eng 11, 1-24.

Grundke-Iqbal, I., Raine, C.S., Johnson, A.B., Brosnan, C.F., Bornstein, M.B., 1981. Experimental allergic encephalomyelitis. Characterization of serum factors causing demyelination and swelling of myelin. J Neurol Sci 50, 63-79.

H. Makamba, J.H.K., K. Lim, N. Park and J. H. Hahn,, 2003. Surface modification of poly(dimethylsiloxane) microchannels. Electrophoresis 24, 3607-3619.

Hanson, J.N., Motala, M.J., Heien, M.L., Gillette, M., Sweedler, J., Nuzzo, R.G., 2009. Textural guidance cues for controlling process outgrowth of mammalian neurons. Lab Chip 9, 122-131.

Hermanns, S., Klapka, N., Gasis, M., Muller, H.W., 2006. The collagenous wound healing scar in the injured central nervous system inhibits axonal regeneration. Adv Exp Med Biol 557, 177-190.

Herx, L.M., Rivest, S., Yong, V.W., 2000. Central nervous system-initiated inflammation and neurotrophism in trauma: IL-1 beta is required for the production of ciliary neurotrophic factor. J Immunol 165, 2232-2239.

Herx, L.M., Yong, V.W., 2001. Interleukin-1 beta is required for the early evolution of reactive astrogliosis following CNS lesion. J Neuropathol Exp Neurol 60, 961-971.

Hocking, D.C., Smith, R.K., McKeown-Longo, P.J., 1996. A novel role for the integrin-binding III-10 module in fibronectin matrix assembly. J Cell Biol 133, 431-444.

Hopcroft, M., Kramer, T., Kim, G., Takashima, K., Higo, Y., Moore, D., Brugger, J., 2005. Micromechanical testing of SU-8 cantilevers. Fatigue & Fracture of Engineering Materials & Structures 28, 735-742.

Humphries, M.J., Obara, M., Olden, K., Yamada, K.M., 1989. Role of fibronectin in adhesion, migration, and metastasis. Cancer Invest 7, 373-393.

John, G.R., Lee, S.C., Brosnan, C.F., 2003. Cytokines: powerful regulators of glial cell activation. Neuroscientist 9, 10-22.

John, G.R., Scemes, E., Suadicani, S.O., Liu, J.S., Charles, P.C., Lee, S.C., Spray, D.C., Brosnan, C.F., 1999. IL-1beta differentially regulates calcium wave propagation between primary human fetal astrocytes via pathways involving P2 receptors and gap junction channels. Proc Natl Acad Sci U S A 96, 11613-11618.

John, G.R., Simpson, J.E., Woodroofe, M.N., Lee, S.C., Brosnan, C.F., 2001. Extracellular nucleotides differentially regulate interleukin-1beta signaling in primary human astrocytes: implications for inflammatory gene expression. J Neurosci 21, 4134-4142.

Kamath, S., Bhattacharyya, D., Padukudru, C., Timmons, R.B., Tang, L., 2008. Surface chemistry influences implant-mediated host tissue responses. J Biomed Mater Res A 86, 617-626.

Kane, S.R., Cogan, S.F., Ehrlich, J., Plante, T.D., McCreery, D.B., 2011. Electrical performance of penetrating microelectrodes chronically implanted in cat cortex. Conf Proc IEEE Eng Med Biol Soc 2011, 5416-5419.

Keller, T.F., Schonfelder, J., Reichert, J., Tuccitto, N., Licciardello, A., Messina, G.M., Marletta, G., Jandt, K.D., 2011. How the surface nanostructure of polyethylene affects protein assembly and orientation. ACS Nano 5, 3120-3131.

Khan, S., Newaz, G., 2010. A comprehensive review of surface modification for neural cell adhesion and patterning. J Biomed Mater Res A 93, 1209-1224.

Kidambi, S., Yarmush, J., Berdichevsky, Y., Kamath, S., Fong, W., Schianodicola, J., 2010. Propofol induces MAPK/ERK cascade dependant expression of cFos and Egr-1 in rat hippocampal slices. BMC Res Notes 3, 201.

Klapka, N., Muller, H.W., 2006. Collagen matrix in spinal cord injury. J Neurotrauma 23, 422-435.

Kotov, N.A., Winter, J.O., Clements, I.P., Jan, E., Timko, B.P., Campidelli, S., Pathak, S., Mazzatenta, A., Lieber, C.M., Prato, M., Bellamkonda, R.V., Silva, G.A., Kam, N.W.S., Patolsky, F., Ballerini, L., 2009. Nanomaterials for Neural Interfaces. Advanced Materials 21, 3970-4004.

Kotzar, G., Freas, M., Abel, P., Fleischman, A., Roy, S., Zorman, C., Moran, J.M., Melzak, J., 2002. Evaluation of MEMS materials of construction for implantable medical devices. Biomaterials 23, 2737-2750.

Kriparamanan, R., Aswath, P., Zhou, A., Tang, L., Nguyen, K.T., 2006. Nanotopography: cellular responses to nanostructured materials. J Nanosci Nanotechnol 6, 1905-1919.

Kühnel, W., 2003. Color atlas of cytology, histology, and microscopic anatomy, Fourth ed. Thieme Medical Publishers.

Laird, M.D., Vender, J.R., Dhandapani, K.M., 2008. Opposing roles for reactive astrocytes following traumatic brain injury. Neurosignals 16, 154-164.

Lee, I.S., Whang, C.N., Park, J.C., Lee, D.H., Seo, W.S., 2003. Biocompatibility and charge injection property of iridium film formed by ion beam assisted deposition. Biomaterials 24, 2225-2231.

Liberto, C.M., Albrecht, P.J., Herx, L.M., Yong, V.W., Levison, S.W., 2004. Pro-regenerative properties of cytokine-activated astrocytes. J Neurochem 89, 1092-1100.

Liu, B., Hong, J.S., 2003. Primary rat mesencephalic neuron-glia, neuron-enriched, microglia-enriched, and astroglia-enriched cultures. Methods Mol Med 79, 387-395.

Livak, K.J., Schmittgen, T.D., 2001. Analysis of relative gene expression data using real-time quantitative PCR and the 2(-Delta Delta C(T)) Method. Methods 25, 402-408.

Logan, A., Berry, M., Gonzalez, A.M., Frautschy, S.A., Sporn, M.B., Baird, A., 1994. Effects of transforming growth factor beta 1 on scar production in the injured central nervous system of the rat. Eur J Neurosci 6, 355-363.

MA Howard, T.M., CA Bauer, December 16, 1997. Human cerebral cortex neural prosthetic for tinnitus. University of Iowa Patent Foundation.

Malipiero, U.V., Frei, K., Fontana, A., 1990. Production of hemopoietic colony-stimulating factors by astrocytes. J Immunol 144, 3816-3821.

Mayeed, M.S., Al-Mekhnaqi, A.M., Auner, G.W., Newaz, G.M., 2009. A surface accumulator of Escherichia coli in water flow. Comput Methods Biomech Biomed Engin 12, 109-112.

McConnell, G.C., Rees, H.D., Levey, A.I., Gutekunst, C.A., Gross, R.E., Bellamkonda, R.V., 2009. Implanted neural electrodes cause chronic, local inflammation that is correlated with local neurodegeneration. J Neural Eng 6, 056003.

McCreery, D., Pikov, V., Lossinsky, A., Bullara, L., Agnew, W., 2004. Arrays for chronic functional microstimulation of the lumbosacral spinal cord. IEEE Trans Neural Syst Rehabil Eng 12, 195-207.

McCreery, D.B., Agnew, W.F., 1983. Changes in extracellular potassium and calcium concentration and neural activity during prolonged electrical stimulation of the cat cerebral cortex at defined charge densities. Exp Neurol 79, 371-396.

McCreery, D.B., Agnew, W.F., Yuen, T.G., Bullara, L., 1990. Charge density and charge per phase as cofactors in neural injury induced by electrical stimulation. IEEE Trans Biomed Eng 37, 996-1001.

McCreery, D.B., Bullara, L.A., Agnew, W.F., 1986. Neuronal activity evoked by chronically implanted intracortical microelectrodes. Exp Neurol 92, 147-161.

Merrill, D.R., Bikson, M., Jefferys, J.G., 2005. Electrical stimulation of excitable tissue: design of efficacious and safe protocols. J Neurosci Methods 141, 171-198.

Mian, A., Newaz, G., Georgiev, D.G., Rahman, N., Vendra, L., Auner, G., Witte, R., Herfurth, H., 2007. Performance of laser bonded glass/polyimide microjoints in cerebrospinal fluid. J Mater Sci Mater Med 18, 417-427.

Mian, A., Newaz, G., Vendra, L., Rahman, N., Georgiev, D.G., Auner, G., Witte, R., Herfurth, H., 2005. Laser bonded microjoints between titanium and polyimide for applications in medical implants. J Mater Sci Mater Med 16, 229-237.

Mieszawska, A.J., Kaplan, D.L., 2010. Smart biomaterials - regulating cell behavior through signaling molecules. BMC Biol 8, 59.

Miller, D.R., Peppas, N.A., 1985. The use of ellipsometry to study adsorption on hydrogels. Biomaterials 6, 33-40.

Millet, L.J., Bora, A., Sweedler, J.V., Gillette, M.U., 2010. Direct cellular peptidomics of supraoptic magnocellular and hippocampal neurons in low-density co-cultures. ACS Chem Neurosci 1, 36-48.

Millet, L.J., Stewart, M.E., Sweedler, J.V., Nuzzo, R.G., Gillette, M.U., 2007. Microfluidic devices for culturing primary mammalian neurons at low densities. Lab Chip 7, 987-994.

Moolwaney, A.S., Igwe, O.J., 2005. Regulation of the cyclooxygenase-2 system by interleukin-1beta through mitogen-activated protein kinase signaling pathways: a comparative study of human neuroglioma and neuroblastoma cells. Brain Res Mol Brain Res 137, 202-212.

Morin, F., Nishimura, N., Griscom, L., Lepioufle, B., Fujita, H., Takamura, Y., Tamiya, E., 2006. Constraining the connectivity of neuronal networks cultured on microelectrode arrays with microfluidic techniques: a step towards neuron-based functional chips. Biosens Bioelectron 21, 1093-1100.

Morin, F.O., Takamura, Y., Tamiya, E., 2005. Investigating neuronal activity with planar microelectrode arrays: achievements and new perspectives. J Biosci Bioeng 100, 131-143.

Morino, Y., Tamiya, S., Masuda, N., Kawamura, Y., Nagaoka, M., Matsukage, T., Ogata, N., Nakazawa, G., Tanabe, T., Ikari, Y., 2010. Intravascular ultrasound criteria for determination of optimal longitudinal positioning of sirolimus-eluting stents. Circ J 74, 1609-1616.

Muir, E., Du, J.S., Fok-Seang, J., Smith-Thomas, L.C., Housden, E.S., Rogers, J., Fawcett, J.W., 1998. Increased axon growth through astrocyte cell lines transfected with urokinase. Glia 23, 24-34.

Negi, S., Bhandari, R., Rieth, L., Solzbacher, F., 2010a. In vitro comparison of sputtered iridium oxide and platinum-coated neural implantable microelectrode arrays. Biomed Mater 5, 15007.

Negi, S., Bhandari, R., Rieth, L., Van Wagenen, R., Solzbacher, F., 2010b. Neural electrode degradation from continuous electrical stimulation: comparison of sputtered and activated iridium oxide. J Neurosci Methods 186, 8-17.

Ni, M., Tong, W.H., Choudhury, D., Rahim, N.A., Iliescu, C., Yu, H., 2009. Cell culture on MEMS platforms: A review. Int J Mol Sci 10, 5411-5441.

Nimmerjahn, A., 2009. Astrocytes going live: advances and challenges. Journal of Physiology 587, 1639-1647.

O'Keefe, G.M., Nguyen, V.T., Ping Tang, L.L., Benveniste, E.N., 2001. IFN-gamma regulation of class II transactivator promoter IV in macrophages and microglia: involvement of the suppressors of cytokine signaling-1 protein. J Immunol 166, 2260-2269.

Pankov, R., Yamada, K.M., 2002. Fibronectin at a glance. J Cell Sci 115, 3861-3863.

Parekkadan, B., Berdichevsky, Y., Irimia, D., Leeder, A., Yarmush, G., Toner, M., Levine, J.B., Yarmush, M.L., 2008. Cell-cell interaction modulates neuroectodermal specification of embryonic stem cells. Neurosci Lett 438, 190-195.

Pennisi, C.P., Dolatshahi-Pirouz, A., Foss, M., Chevallier, J., Fink, T., Zachar, V., Besenbacher, F., Yoshida, K., 2011. Nanoscale topography reduces fibroblast growth, focal adhesion size and migration-related gene expression on platinum surfaces. Colloids Surf B Biointerfaces 85, 189-197.

Pennisi, C.P., Sevcencu, C., Dolatshahi-Pirouz, A., Foss, M., Hansen, J.L., Larsen, A.N., Zachar, V., Besenbacher, F., Yoshida, K., 2009. Responses of fibroblasts and glial cells to nanostructured platinum surfaces. Nanotechnology 20, 385103.

Petrossians, A., Whalen J.J., Weiland J.D., Mansfeld F., 2011. Electrodeposition and Characterization of Thin-Film Platinum-Iridium Alloys for Biological Interfaces. Journal of Electrochemical Society 158, D269-D276.

Petrossians, A., Whalen, J.J., Weiland, J.D., Mansfeld, F., 2011. Surface modification of neural stimulating/recording electrodes with high surface area platinum-iridium alloy coatings. Conf Proc IEEE Eng Med Biol Soc 2011, 3001-3004.

Polikov, V.S., Block, M.L., Fellous, J.M., Hong, J.S., Reichert, W.M., 2006. In vitro model of glial scarring around neuroelectrodes chronically implanted in the CNS. Biomaterials 27, 5368-5376.

Polikov, V.S., Su, E.C., Ball, M.A., Hong, J.S., Reichert, W.M., 2009. Control protocol for robust in vitro glial scar formation around microwires: essential roles of bFGF and serum in gliosis. J Neurosci Methods 181, 170-177.

Polikov, V.S., Tresco, P.A., Reichert, W.M., 2005. Response of brain tissue to chronically implanted neural electrodes. J Neurosci Methods 148, 1-18.

Rao, J.S., Kellom, M., Kim, H.W., Rapoport, S.I., Reese, E.A., 2012. Neuroinflammation and Synaptic Loss. Neurochem Res.

Rauch, U., 2007. Brain matrix: structure, turnover and necessity. Biochem Soc Trans 35, 656-660.

Rose, T.L., Kelliher, E.M., Robblee, L.S., 1985. Assessment of capacitor electrodes for intracortical neural stimulation. J Neurosci Methods 12, 181-193.

Rose, T.L., Robblee, L.S., 1990. Electrical stimulation with Pt electrodes. VIII. Electrochemically safe charge injection limits with 0.2 ms pulses. IEEE Trans Biomed Eng 37, 1118-1120.

Rostworowski, M., Balasingam, V., Chabot, S., Owens, T., Yong, V.W., 1997. Astrogliosis in the neonatal and adult murine brain post-trauma: elevation of inflammatory cytokines and the lack of requirement for endogenous interferon-gamma. J Neurosci 17, 3664-3674.

S. Negi, R.B., L. Rieth, F. Solzbacher, 2009. Effect of sputtering pressure on pulsed-DC sputtered iridium oxide films. Sens Actuators B Chemical 137, 370-378.

Salakhutdinov, I., VandeVord, P., Palyvoda, O., Matthew, H., Tatagiri, G., Handa, H., Mao, G., Auner, G.W., Newaz, G., 2008. Fibronectin adsorption to nanopatterned silicon surfaces. J Nanomater, -
.

Samuel K. Sia, G.M.W., 2003. Microfluidic devices fabricated in Poly(dimethylsiloxane) for biological studies. ELECTROPHORESIS 24, 3563-3576.

Sarasa-Renedo, A., Chiquet, M., 2005. Mechanical signals regulating extracellular matrix gene expression in fibroblasts. Scand J Med Sci Sports 15, 223-230.

Schmittgen, T.D., Livak, K.J., 2008. Analyzing real-time PCR data by the comparative C(T) method. Nat Protoc 3, 1101-1108.

Seil, J.T., Webster, T.J., 2008. Decreased astroglial cell adhesion and proliferation on zinc oxide nanoparticle polyurethane composites. Int J Nanomedicine 3, 523-531.

Seker, E., Berdichevsky, Y., Begley, M.R., Reed, M.L., Staley, K.J., Yarmush, M.L., 2010. The fabrication of low-impedance nanoporous gold multiple-electrode arrays for neural electrophysiology studies. Nanotechnology 21, 125504.

Shirtcliffe, N.J., Aqil, S., Evans, C., McHale, G., Newton, M.I., Perry, C.C., Roach, P., 2004. The use off high aspect ratio photoresist (SU-8) for super-hydrophobic pattern prototyping. J Micromech Microeng 14, 1384-1389.

Shrikant, P., Benveniste, E.N., 1996. The central nervous system as an immunocompetent organ: role of glial cells in antigen presentation. J Immunol 157, 1819-1822.

Smeal, R.M., Gaspar, R.C., Keefe, K.A., Wilcox, K.S., 2007. A rat brain slice preparation for characterizing both thalamostriatal and corticostriatal afferents. J Neurosci Methods 159, 224-235.

Smith, G.M., Hale, J.H., 1997. Macrophage/Microglia regulation of astrocytic tenascin: synergistic action of transforming growth factor-beta and basic fibroblast growth factor. J Neurosci 17, 9624-9633.

Sofroniew, M.V., Vinters, H.V., 2010. Astrocytes: biology and pathology. Acta Neuropathol 119, 7-35.

Song, M., Uhrich, K.E., 2007. Optimal micropattern dimensions enhance neurite outgrowth rates, lengths, and orientations. Ann Biomed Eng 35, 1812-1820.

Stice, P., Muthuswamy, J., 2009. Assessment of gliosis around moveable implants in the brain. Journal of Neural Engineering 6, -.

Sudo, R., Chung, S., Zervantonakis, I.K., Vickerman, V., Toshimitsu, Y., Griffith, L.G., Kamm, R.D., 2009. Transport-mediated angiogenesis in 3D epithelial coculture. FASEB J 23, 2155-2164.

Szarowski, D.H., Andersen, M.D., Retterer, S., Spence, A.J., Isaacson, M., Craighead, H.G., Turner, J.N., Shain, W., 2003. Brain responses to micro-machined silicon devices. Brain Res 983, 23-35.

T. C. Merkel, V.I.B., K. Nagai, B. D. Freeman, I. Pinnau, 2000. Gas sorption, diffusion, and permeation in poly(dimethylsiloxane). Journal of Polymer Science Part B: Polymer Physics 38, 415-434.

Tang, L., Wu, Y., Timmons, R.B., 1998. Fibrinogen adsorption and host tissue responses to plasma functionalized surfaces. J Biomed Mater Res 42, 156-163.

Tate, C.C., Garcia, A.J., LaPlaca, M.C., 2007. Plasma fibronectin is neuroprotective following traumatic brain injury. Exp Neurol 207, 13-22.

Tate, C.C., Shear, D.A., Tate, M.C., Archer, D.R., Stein, D.G., LaPlaca, M.C., 2009. Laminin and fibronectin scaffolds enhance neural stem cell transplantation into the injured brain. J Tissue Eng Regen Med 3, 208-217.

Taupin, V., Toulmond, S., Serrano, A., Benavides, J., Zavala, F., 1993. Increase in IL-6, IL-1 and TNF levels in rat brain following traumatic lesion. Influence of pre- and post-traumatic treatment with Ro5 4864, a peripheral-type (p site) benzodiazepine ligand. J Neuroimmunol 42, 177-185.

Teixeira, A.I., Abrams, G.A., Bertics, P.J., Murphy, C.J., Nealey, P.F., 2003. Epithelial contact guidance on well-defined micro- and nanostructured substrates. J Cell Sci 116, 1881-1892.

Thanawala, S., Palyvoda, O., Georgiev, D.G., Khan, S.P., Al-Homoudi, I.A., Newaz, G., Auner, G., 2007. A neural cell culture study on thin film electrode materials. J Mater Sci Mater Med 18, 1745-1752.

Theil, D., Farina, C., Meinl, E., 2005. Differential expression of CD150 (SLAM) on monocytes and macrophages in chronic inflammatory contexts: abundant in Crohn's disease, but not in multiple sclerosis. J Clin Pathol 58, 110-111.

Thevenot, P., Cho, J., Wavhal, D., Timmons, R.B., Tang, L., 2008. Surface chemistry influences cancer killing effect of TiO2 nanoparticles. Nanomedicine 4, 226-236.

Turner, J.N., Shain, W., Szarowski, D.H., Andersen, M., Martins, S., Isaacson, M., Craighead, H., 1999. Cerebral astrocyte response to micromachined silicon implants. Exp Neurol 156, 33-49.

Vernekar, V.N., Cullen, D.K., Fogleman, N., Choi, Y., Garcia, A.J., Allen, M.G., Brewer, G.J., LaPlaca, M.C., 2009. SU-8 2000 rendered cytocompatible for neuronal bioMEMS applications. J Biomed Mater Res A 89, 138-151.

Voskerician, G., Shive, M.S., Shawgo, R.S., von Recum, H., Anderson, J.M., Cima, M.J., Langer, R., 2003. Biocompatibility and biofouling of MEMS drug delivery devices. Biomaterials 24, 1959-1967.

Wang, L., Wu, Z.Z., Xu, B.Q., Zhao, Y.P., Kisaalita, W.S., 2009. SU-8 microstructure for quasi-three-dimensional cell-based biosensing. Sensor Actuat B-Chem 140, 349-355.

Wang, Z., Millet, L., Chan, V., Ding, H., Gillette, M.U., Bashir, R., Popescu, G., 2011. Label-free intracellular transport measured by spatial light interference microscopy. J Biomed Opt 16, 026019.

Williams, J.C., Rennaker, R.L., Kipke, D.R., 1999. Long-term neural recording characteristics of wire microelectrode arrays implanted in cerebral cortex. Brain Res Brain Res Protoc 4, 303-313.

Woodford, B.J., Carter, R.R., McCreery, D., Bullara, L.A., Agnew, W.F., 1996. Histopathologic and physiologic effects of chronic implantation of microelectrodes in sacral spinal cord of the cat. J Neuropathol Exp Neurol 55, 982-991.

Wu, Z.Z., Zhao, Y., Kisaalita, W.S., 2006. Interfacing SH-SY5Y human neuroblastoma cells with SU-8 microstructures. Colloids Surf B Biointerfaces 52, 14-21.

Wyss-Coray, T., Lin, C., Sanan, D.A., Mucke, L., Masliah, E., 2000. Chronic overproduction of transforming growth factor-beta1 by astrocytes promotes Alzheimer's disease-like microvascular degeneration in transgenic mice. Am J Pathol 156, 139-150.

Yim, E.K., Pang, S.W., Leong, K.W., 2007. Synthetic nanostructures inducing differentiation of human mesenchymal stem cells into neuronal lineage. Exp Cell Res 313, 1820-1829.

Yoles, E., Hauben, E., Palgi, O., Agranov, E., Gothilf, A., Cohen, A., Kuchroo, V., Cohen, I.R., Weiner, H., Schwartz, M., 2001. Protective autoimmunity is a physiological response to CNS trauma. J Neurosci 21, 3740-3748.

Yonezawa, T., Hattori, S., Inagaki, J., Kurosaki, M., Takigawa, T., Hirohata, S., Miyoshi, T., Ninomiya, Y., 2010. Type IV collagen induces expression of thrombospondin-1 that is mediated by integrin alpha1beta1 in astrocytes. Glia 58, 755-767.

Yuen, T.G., Agnew, W.F., Bullara, L.A., Jacques, S., McCreery, D.B., 1981. Histological evaluation of neural damage from electrical stimulation: considerations for the selection of parameters for clinical application. Neurosurgery 9, 292-299.

Zervantonakis, I.K., Kothapalli, C.R., Chung, S., Sudo, R., Kamm, R.D., 2011. Microfluidic devices for studying heterotypic cell-cell interactions and tissue specimen cultures under controlled microenvironments. Biomicrofluidics 5, 13406.

Zhong, Y., Bellamkonda, R.V., 2008. Biomaterials for the central nervous system. J R Soc Interface 5, 957-975.

Zimmermann, D.R., Dours-Zimmermann, M.T., 2008. Extracellular matrix of the central nervous system: from neglect to challenge. Histochem Cell Biol 130, 635-653.

Zisman, K.W.B.a.W.A., 1965. The Wetting of Gold and Platinum by Water. The Journal of Physical Chemistry 69.

Zorba, V., Persano, L., Pisignano, D., Athanassiou, A., Stratakis, E., Cingolani, R., Tzanetakis, P., Fotakis, C., 2006. Making silicon hydrophobic: wettability control by two-lengthscale simultaneous patterning with femtosecond laser irradiation. Nanotechnology 17, 3234-3238.

ABSTRACT

STUDYING THE GLIAL CELL RESPONSE TO BIOMATERIALS AND SURFACE TOPOGRAPHY FOR IMPROVING THE NEURAL ELECTRODE INTERFACE

by

EVON EREIFEJ

MAY 2012

Advisor: Pamela J. VandeVord

Major: Biomedical Engineering

Degree: Doctor of Philosophy

Neural electrode devices hold great promise to help people with the restoration of lost functions, however, research is lacking in the biomaterial design of a stable, long-term device. Current devices lack long term functionality, most have been found unable to record neural activity within weeks after implantation due to the development of glial scar tissue (Polikov et al., 2006; Zhong and Bellamkonda, 2008). The long-term effect of chronically implanted electrodes is the formation of a glial scar made up of reactive astrocytes and the matrix proteins they generate (Polikov et al., 2005; Seil and Webster, 2008). Scarring is initiated when a device is inserted into brain tissue and is associated with an inflammatory response. Activated astrocytes are hypertrophic, hyperplastic, have an upregulation of intermediate filaments GFAP and vimentin expression, and filament formation (Buffo et al., 2010; Gervasi et al., 2008).

Current approaches towards inhibiting the initiation of glial scarring range from altering the geometry, roughness, size, shape and materials of the device (Grill et al., 2009; Kotov et al., 2009; Kotzar et al., 2002; Szarowski et al., 2003). Literature has shown that surface topography modifications can alter cell alignment, adhesion, proliferation, migration, and gene expression (Agnew et al., 1983; Cogan et al., 2005; Cogan et al., 2006; Merrill et al., 2005). Thus, the goals

of the presented work are to study the cellular response to biomaterials used in neural electrode fabrication and assess surface topography effects on minimizing astrogliosis.

Initially, to examine astrocyte response to various materials used in neural electrode fabrication, astrocytes were cultured on platinum, silicon, PMMA, and SU-8 surfaces, with polystyrene as the control surface. Cell proliferation, viability, morphology and gene expression was measured for seven days *in vitro*. Results determined the cellular characteristics, reactions and growth rates of astrocytes grown on PMMA resembled closely to that of cells grown on the control surface, thus confirming the biocompatibility of PMMA. Additionally, the astrocyte GFAP gene expressions of cells grown on PMMA were lower than the control, signifying a lack of astrocyte reactivity.

Based on the findings from the biomaterials study, it was decided to optimize PMMA by changing the surface characteristic of the material. Through the process of hot embossing, nanopatterns were placed on the surface in order to test the hypothesis that nanopattterning can improve the cellular response to the material. Results of this study agreed with current literature showing that topography effects protein and cell behavior. It was concluded that for the use in neural electrode fabrication and design, the 3600mm/gratings pattern feature sizes were optimal. The 3600 mm/gratings pattern depicted cell alignment along the nanopattern, less protein adsorption, less cell adhesion, proliferation and viability, inhibition of GFAP and MAP2k1 compared to all other substrates tested.

Results from the initial biomaterials study also indicated platinum was negatively affected the cells and may not be a suitable material for neural electrodes. This lead to pursuing studies with iridium oxide and platinum alloy wires for the glial scar assay. Iridium oxide

advantages of lower impedance and higher charge injection capacity would appear to make iridium oxide more favorable for neural electrode fabrication. However, results of this study demonstrate iridium oxide wires exhibited a more significant reactive response as compared to platinum alloy wires. Astrocytes cultured with platinum alloy wires had less GFAP gene expression, lower average GFAP intensity, and smaller glial scar thickness.

Results from the nanopatterning PMMA study prompted a more thorough investigation of the nanopatterning effects using an organotypic brain slice model. PDMS was utilized as the substrate due to its optimal physical properties. Confocal and SEM imaging illustrated cells from the brain tissue slices were aligned along the nanopattern on the PDMS pins. Decreases in several inflammatory markers (GFAP, TNFα, IL-1β) determined from gene expression analysis, was shown with the nanopatterned PDMS pins. Results of this study confirm nanopatterning not only influences cell morphology, but alters molecular cascades within the cells as well.

The results of these studies provide essential information for the neural electrode research community. There is a lack of information available in the scientific community on acceptable and effective materials for neural electrode fabrication. The results of the presented studies provide more information which could lead to classifying guidelines to create biocompatible neural electrode materials.

This research project was partially supported by the Wayne State University President's Translational Enhancement Award and by the Kales Scholarship for Biomedical Engineering students.

AUTOBIOGRAPHICAL STATEMENT

EVON S. EREIFEJ

EDUCATION

Ph.D. Biomedical Engineering, Wayne State University-WSU, Detroit, MI, 2012
M.S. Biomedical Engineering, Wayne State University-WSU, Detroit, MI, 2007
B.S. Biological Sciences, Wayne State University-WSU, Detroit, MI, 2005

POSITIONS

2011-2012 Adjunct Faculty, Biomedical Engineering, WSU, Detroit, MI
2010-2011 Research Assistant, Biomedical Engineering, WSU, Detroit, MI
2009- 2010 Graduate Research Assistant, Mechanical Engineering, WSU, Detroit, MI
2008-2009 Graduate Teaching Assistant, Engineering, WSU, Detroit MI
2007-2008 Adjunct Faculty, Biology, Macomb Community College, Warren, MI

HONORS AND AWARDS

2011 Anthony and Joyce Danielski Kales Scholarship
2011 Wayne State University Dissertation Research Support Award

PUBLICATIONS

Ereifej ES, Khan S, Newaz G, Zhang J, Auner GW, VandeVord PJ. Comparative Assessment of Iridium Oxide and Platinum Alloy Wires using an in vitro Glial Scar Assay. Biomaterials 2012 (submitted)

Ereifej ES, Khan S, Newaz G, Zhang J, Auner GW, VandeVord PJ. Characterization of Astrocyte Reactivity and Gene Expression on Biomaterials for Neural Electrodes. Journal of Biomedical Materials Research: Part A. 2011 Oct;99(1):141-50

Trivedi V, Doshi A, Kurup GK, Ereifej ES, Vandevord PJ, Basu AS.A modular approach for the generation, storage, mixing, and detection of droplet libraries for high throughput screening.Lab Chip. 2010 Sep 21;10(18):2433-42.

de Guzman R, Ereifej ES , Broadrick KM, Rogers RA, VandeVord PJ. Alginate-matrigel microencapsulated Schwann cells for inducible secretion of glial cell line derived neurotrophic factor. Journal of Microencapsulation, 17:1-12 (2008)

PRESENTATIONS

Ereifej ES, Khan S, Newaz G, VandeVord PJ. Comparitive Assessment of Iridium Oxide and Platinum Wires Using an in vitri Glial Scar Assay. Society for Biomaterials National Conference, April 2011, Orlando, FL, Poster Presentation

Ereifej ES, Yang J, Cheng MC, VandeVord PJ. Astrocyte Reactivity to Neural Implant with Porous Silicon Backbone Support. Society for Biomaterials National Conference, April 2011, Orlando, FL, Poster Presentation

Ereifej ES, Salakhutdinov I, Mukhopadhyay A, Matthew H, VandeVord PJ. Nanopatterning Effects on Protein Adsorption and Glial Cell Response Biomedical Engineering Society National Conference, October 2009, Pittsburgh, PA, Podium Presentation

Trivedi V, Ereifej ES, Doshi A, Sehgal P, VandeVord PJ, Basu A. Microfluidic Encapsulation of Cells in Alginate Capsules for High Throughput Screening. 31st Annual International IEEE EMBS Conference, September 2009, Minneapolis, MN, Podium Presentation

Ereifej ES, Salakhutdinov I, VandeVord PJ. The Effect of Nanopatterning Poly(methyl methacrylate) on Glial Cell Activation and Proliferation. Society for Biomaterials National Conference, April 2009, San Antonio, TX, Podium Presentation

Ereifej ES, Khan S, Newaz G, VandeVord PJ. Astrocyte Response to Various Biomaterials for bioMEMs. Society for Biomaterials National Conference, April 2009, San Antonio, TX, Poster Presentation

Ereifej ES, de Guzman RC, Rogers R, VandeVord PJ. Comparison of Long Term Viability and Mechanical Stability of Alginate versus Alginate-Matrigel Microencapsulated Schwann Cells. World Biomaterials Congress, May 2008, Amsterdam, Netherlands, Podium Presentation

Ereifej ES, de Guzman RC, Rogers R, VandeVord PJ. Long Term Viability and Mechanical Stability of Alginate-Microencapsulated Schwann Cells. Biomedical Engineering Society National Conference, September 2007, Las Angeles, CA, Poster Presentation

Ereifej ES, de Guzman RC, VandeVord PJ. Long Term Viability of Alginate-Microencapsulated Schwann Cell Line RT4-D6P2T. Society for Biomaterials National Conference, April 2007, Chicago, IL, Poster Presentation